Chaos, Solitons and Fractals 186 (2024) 115323

Contents lists available at ScienceDirect

Chaos, Solitons and Fractals

journal homepage: www.elsevier.com/locate/chaos

Observer based decentralized load frequency control with false data injection attack for specified network quality and delay

Deepak Kumar Panda [a,e], Kaushik Halder [b], Saptarshi Das [a,c,*], Stuart Townley [a,d]

[a] Centre for Environmental Mathematics, Faculty of Environment, Science and Economy, University of Exeter, Penryn Campus, Cornwall TR10 9FE, United Kingdom
[b] School of Computing & Electrical Engineering, Indian Institute of Technology Mandi, Kamand, Mandi, Himachal Pradesh 175005, India
[c] Institute for Data Science and Artificial Intelligence, University of Exeter, North Park Road, Exeter, Devon EX4 4QE, United Kingdom
[d] Environment and Sustainability Institute, University of Exeter, Penryn Campus, Cornwall TR10 9FE, United Kingdom
[e] Centre for Autonomous and Cyber-Physical Systems, Cranfield University, Cranfield, Bedfordshire MK43 0AL, United Kingdom

ARTICLE INFO

Keywords:
Grid frequency
Delay and packet drop
Load frequency control
Demand response
Electric vehicles
Stochastic renewable energy

ABSTRACT

Load frequency control (LFC) aims to stabilize grid frequency fluctuations by countering load disturbances with generation-side controllers. In smart grids, demand response (DR) and electric vehicles (EV) offer alternatives to traditional frequency control, reducing reliance on costly generation-side controllers. These decentralized controls, interconnected through a shared communication medium, form a cyber-physical system, vulnerable to challenges like packet drops and false data injection (FDI) attacks. Additionally, consumer participation in DR introduces significant time delays. This paper derives stability conditions for LFC using a state feedback controller, estimating unobservable states with an observer while accounting for bounded disturbances and noise. This cyber-physical system, involving an observer, controller, and network, is modelled as an observer-based networked control system (NCS) using an asynchronous dynamical system (ADS) approach. The resulting switched system model is used to establish linear matrix inequality (LMI) criteria that ensure stability and determine observer and controller gains under specified packet drop rates, disturbances, and noise. The methodology is tested on various configurations, demonstrating that decentralized EV with LFC and DR improves system response, minimizes frequency fluctuations, and optimizes networked control bandwidth under given conditions.

1. Introduction

Traditional LFC in power systems uses spinning and non-spinning reserves [1] to balance the generation and variable load demand. However, modern power grids incorporate a high penetration of stochastic renewable energy [2]. Hence, responsive loads can be utilized as a part of the DR strategy to balance the generation and demand [3]. Moreover, it also helps to avoid the traditional load following schemes that lower operational costs and greenhouse gas emissions [4]. The load demands are met by balancing mechanisms (BM) with units operating at different time scales [5]. Non-BM units typically involve the loads participating in DR. As per the report by National Grid [6], £105.6 M was spent on the generation side for the balancing mechanism. DR techniques can be utilized to reduce the costs incurred in the BM and are implemented with real-time consumer participation by regulating the electricity market price [7]. The delay in consumer response, incurred due to the tariff adjustment from various DR techniques, can cause grid stability problems [8].

1.1. Previous works on DR, EV, and renewable energy in LFC

The automatic generation control (AGC) system employs conventional controllers in conjunction with various renewable energy sources [9], whose design is formulated using the solution of LMIs. In the context of LFC [10,11], diverse distributed generators (DGs) have been considered, encompassing systems such as wind turbine generators (WTGs), fuel cells (FCs), aqua electrolysers (AEs), and diesel engine generators (DEGs). Furthermore, the inclusion of wind turbine models [12,13] and

* Corresponding author at: Centre for Environmental Mathematics, Faculty of Environment, Science and Economy, University of Exeter, Penryn Campus, Cornwall TR10 9FE, United Kingdom.
E-mail addresses: dp457@exeter.ac.uk (D.K. Panda), kaushik@iitmandi.ac.in (K. Halder), saptarshi.das@ieee.org, s.das3@exeter.ac.uk (S. Das), s.b.townley@exeter.ac.uk (S. Townley).

https://doi.org/10.1016/j.chaos.2024.115323
Received 30 March 2024; Received in revised form 6 July 2024; Accepted 21 July 2024
Available online 1 August 2024

the combined wind and hydro generating systems with battery systems [14,15] have also been explored within the LFC framework. Investigations into stochastic models of renewable energy demand in LFC have been conducted in [16,17] and the corresponding simulation analysis has also been conducted regarding the grid frequency fluctuations.

Coordination mechanisms among multiple household devices engaged in frequency control have been devised, leveraging time-frequency thresholds [18] without incorporating it within the LFC loops. Dynamic DR models, utilizing the linear quadratic regulators (LQR), have been introduced to enhance LFC [19], while control parameter optimization for smart appliances participating in DR strategies has been addressed based on frequency deviation thresholds [20]. Regional DR schemes, on tie-line power flows, have been implemented in [21], using the dynamic adaptive demand response (DADR) for augmenting frequency stability within distribution networks [22]. This concept has been extended to encompass the control of fast-dynamic appliances such as refrigerators [23]. Control loop enhancements, including adaptive delay compensators to mitigate communication delays [24], and extended state observers to estimate disturbances and uncertainties have been designed in the context of DR in LFC.

Electric vehicles (EVs) have been integrated into LFC frameworks [25,26], functioning as controllable loads alongside other household appliances. Similarly, electric water heaters, heat pump water heaters, and EVs have been utilized as controllable loads for grid frequency regulation [24,25,27]. The impact of WTGs on LFC systems has been examined in [28], along with demonstrations of EV-based battery storage systems leveraging vehicle-to-grid (V2G) technology in dynamic power systems and their integration in the AGC systems has been pursued in [29], with future considerations incorporating combined use of heat pump water heaters and electric vehicles for enhanced grid stability [30]. Challenges pertaining to cyber-attacks on AGC systems within future smart grids have been analysed in [31], amidst the broader challenge of operating and controlling power systems along with the integration of fluctuating renewable energy sources [32].

The efficacy of LFC systems amidst high-penetration wind and photovoltaic (PV) power integration has been evaluated [33], with microgrid integration of renewable energy sources alongside EVs, aimed at mitigating frequency fluctuations [34]. Recent efforts have focused on establishing stability conditions for networked LFC systems incorporating EVs, employing stochastic jump system theory [35], linear operator inequalities [36], and event-triggered control strategies employing switching approaches [37].

1.2. Previous works of networked control systems and its applications in LFC

In modern power systems, decentralized control of a smart grid utilizes a shared communication medium due to its ease of implementation, maintenance etc., so that a modern smart grid system with a shared communication medium can be viewed as a cyber-physical system or an NCS. However, the inherent structure of the communication network in the smart grid may cause network imperfections such as communication delay and/or packet dropout among the devices and are also vulnerable to cyber-attacks such as denial of service (DoS) attack which degrades the control loop performances and also may lead to whole system instability. Contemporary researchers have attempted to analyse stability by designing robust controller for such systems under packet drop and/or communication delay. For example, LMI based event trigger control mechanism have been proposed for the LFC under communication delay in [38]. Bilinear matrix inequality (BMI) based Lyapunov stability criteria and state feedback controller design has also been proposed for the LFC under communication delay and packet drops. Other works on mitigating cyber-attack in the NCS used different methods such as evolutionary optimization technique [16], hierarchical games [39], delay estimator and decision making unit [40], zero-input actuator policy within an additional loop [41].

Cyber-attack, where information within NCS is corrupted, is known as an FDI attack. FDI attack in LFC has been detected using a neural network in [42,43], and defence strategy has been developed using generative adversarial networks (GANs) in [44]. The neural network weights are updated using an extended Kalman filtering (EKF) algorithm in [42,43] for resilient estimation of the states corrupted by FDI. A non-integer disturbance observer based refined frequency control technique has been designed in [45] and the performance has been assessed against unknown disturbances and cyber-attacks.

Whereas closed-loop exponential stability of the NCS under packet drop, with an observer-based state feedback controller, has been ensured by deriving an LMI presented in [46]. The stability conditions of NCS, modelled as switched systems, are derived considering the relationship between the packet dropout rate and Lyapunov stability criteria using the average dwell time approach. A similar switched system concept is utilized in [47] to tackle a class of NCS with random packet losses while ensuring robust stability.

However, the switched system, signifying packet drop in forward and feedback path, is modelled using the Bernoulli distribution to design an observer-based controller such that the closed-loop NCS meets the criteria for exponential stochastic stability. Similar an NCS modelling approach is utilized in [48,49] using a switched system approach and linear Bernoulli function. A robust controller is designed considering the NCS packet drops as a discrete-time Markovian jump system between different states [50]. Joint design of parameters for stochastic independent and identically distributed (IID) protocols for signal transmission in NCS and control gains are obtained in [51] to ensure system stability. A simultaneous predictive strategy is utilized in [52,53] to forecast the estimated states lost in the communication channel. However, in this case, the packet drop rate is considered after the data processing unit, and the predictor output is used as a signal to design the controller.

1.3. Research gap, novelty and contributions of this paper

Comparing the existing works mentioned in the previous subsections, we can summarize the research gaps as:

- Prior efforts in designing controllers for LFC have predominantly employed output feedback strategies, neglecting the state-feedback designs. State feedback design permits the integration of independent controllable energy sources with conventional controllers.
- Existing literature in this domain has not simultaneously addressed stochastic renewable energy and packet drops within the same control loop. While our previous work has partially addressed this issue [16], the packet drop considerations have been limited to the feedforward path only. Additionally, contemporary aspects of the smart grid, such as stochastic renewable energy and decentralized energy sources like DR and EVs, remain unexplored in [54] even though packet drop scenarios have been considered.
- A comprehensive analysis of a generalized control strategy tested across different smart grid configurations, such as EVs and DR, is lacking in the previous literature.

Therefore, to address the above challenges, in this paper, the robust state feedback controller and observer are jointly designed for the NCS modelled as a switched system using the ADS approach [55,56] under random packet drops and process and measurement disturbances. The state feedback controller and observer gains are obtained simultaneously while satisfying bounded H_∞ norm. A set of LMI criteria are derived and used to obtain the controller and observer gain, ensuring the exponential system stability and state estimation at an arbitrary packet drop rate and external disturbances. The Lyapunov stability criteria satisfying the H_∞ norm bound has been derived from our previous work in [57], and in this paper observer based state-feedback control strategy

has been designed instead of the PI controller derived in our previous work.

ADS model for the NCS provides an edge over the existing modelling strategies using Bernoulli packet drops in [46,48], and Markovian jump model in [50,58] as it takes into account the stochastic ordering and transmission of packets with a uniform sampling time. Moreover, the stochastic packet transmission at an arbitrary rate helps us gauge the system performance. Stochastic protocol for packet scheduling and dropout rates are considered in [51], but the emphasis is on obtaining the optimal parameters of the stochastic IID protocol for facilitating signal transmission. Moreover, the aperiodic sampling rate for designing the communication protocol is challenging to implement in practice. This paper formulates a set of LMI criteria for the NCS modelled as a switched system considering arbitrary packet drops in a shared communication network from the sensor to observer and controller to actuator while extending the theoretical framework in [59] for an observer and state feedback controller and satisfying the norm bound of the output concerning the disturbance and noise as shown in [47]. The proposed networked observer and state feedback controller design methodology is utilized for an LFC system while incorporating the DR strategies and EV control strategy.

The proposed state feedback control strategy helps us to design a decentralized control strategy for multiple control input within the system, i.e. secondary controllers, EV, and DR aggregators. The decentralized infrastructure involves a shared communication network for the secondary frequency control from the generation company (GENCO) and DR scheme from the independent load and EV aggregator. This scheme is analogous to a server-client topology described in the IEEE Standard 2030.5–2018 [60] for smart energy profile application protocol. The energy controller gains form the back-end server, the secondary load controllers and independent EV and load aggregators are on the application frontend interface. Power system deregulation renders the decoupling of DR and secondary loop control viable.

Similarly, in [37], the EV is coupled with the LFC signal. However, in this paper, the system response is tested against coupled and decoupled EV aggregator in the LFC. A shared communication network between the resources makes it prone to cyber-attacks in the form of a high packet drop rate, considered equivalent to DoS attack. The controller and observer gains are generally obtained for lower packet drop rates in [46] using the switched system model. However, higher packet drop rates, considered equivalent to a DoS attacks [16], are utilized for obtaining controller and observer gains.

The phasor measurement units (PMU) measure the power grid frequency, and the power exchanged between different areas [61]. The security of the data collected by PMU is discussed in [60] as per the IEEE Standard C37.247.2019. The data processing capability of the PMUs can be severely affected due to malware attacks [62], as per the IEEE Standard 1815-2012 distributed network protocol (DNP3) used in smart grid distribution [63]. The gaps between the octets of the 16-octet block make it viable for the attackers to corrupt the incoming data frame, which is interpreted as an FDI attack. The observer is utilized to measure the system states corrupted with the FDI attack [64]. Moreover, the observer for LFC helps us visualize the rate of change of variables under disturbance and noise, which is quite expensive in practice with the distributed sensors. Based on the ratio of infinity norm of output and disturbance, the designed controller will stabilize the system based on arbitrary packet loss at a specific rate, rather than finding the probability bound as given in [54,65].

The research reported in this paper represents the smart grid architectural model (SGAM) [63,65,66] where the LFC, demand response and EV model represents the component layer. The shared communication medium in the feedback path between the PMU and EV power utilization measurement to the server computing the control gain and forward path between the load aggregator to the consumer, EV aggregator to the EV charging centre and control centre to the governor control system represents the communication layer. The observer, representing the server estimating the system states, forms the information layer. The control algorithm represents the functional layer. The usage of various EV and demand response configuration to reduce the spinning reserve costs forms the business layer objective. Hence, we can summarize the key novelty as follows:

- ***Theoretical Innovation:*** This paper introduces a pioneering approach to design a robust state feedback controller and observer tailored for NCS, conceptualized as switched systems. Leveraging an ADS framework [53,55], our methodology addresses the challenges posed by random packet drops and process/measurement disturbances. This research builds upon our previous work [57], where a robust output feedback Proportional-Integral (PI) controller was devised, ensuring output robustness against bounded H_∞ norm concerning input disturbances.
- ***Application Advancement:*** Our study breaks new ground by applying the novel state feedback controller and observer design to mitigate frequency fluctuations across diverse smart grid configurations, while accommodating packet drops in both feedforward and feedback pathways. This research extends the scope of our earlier research [16], which primarily focused on examining packet drops within the feedforward domain. Notably, this paper establishes a guaranteed stability criterion, an aspect absent in our prior work [16]. The LFC model employed here draws from [37], incorporating an electric vehicle (EV) model, although it does not consider the time delay of demand response and packet drop conditions. While packet drop scenarios are addressed in [54], the modern aspects of the smart grid, such as decentralized EV and DR scenarios, remain unexplored.

Based on the novelty outlined above, the unique contributions of this paper are as follows:

- ***Implementation of State Feedback Control***: Unlike previous studies employing output feedback control, this paper utilizes a state feedback control scheme for LFC. By integrating this state-feedback control scheme, the LFC loop becomes adaptable to incorporate modern components of the smart grid, such as independent energy sources like EVs and demand response. The Lyapunov stability criteria are utilized to find the observer and controller gains, with the existence of common quadratic Lyapunov function (CQLF) [56,59,67,68] for the NCS while satisfying H_∞ norm bound and ensuring exponentially stability of the system. Notably, while EVs are addressed in [37], their independence, as demonstrated in this paper, is emphasized, as they are not reliant on the output of conventional control schemes.
- ***Comprehensive Analysis and Benchmarking across Modern Smart Grid Configurations:*** This paper conducts an in-depth analysis using rigorous statistical tests to evaluate the impact of stochastic renewable energy and packet drop rates. This aspect has only been previously explored in our prior work [16]. Furthermore, the analysis extends beyond previous studies by considering an additional FDI attack alongside controllable decentralized energy sources like EVs and demand response. Furthermore, it also tests the robustness of the system to various packet drop rates and demand response time delay scenarios which is analogous to a DoS attack [16] and time delay attack [69]. This is the first paper which considers the cascaded cyber-attack impacts viz. DoS, time delay and FDI, along with the stochastic renewable energy and load demand.
- ***Statistical Analysis with Stochastic Renewable Energy and Load Demand Scenarios:*** The stabilizing controller for different LFC configurations, EV and DR, are tested against stochastic renewable energy source modelled by geometric Brownian motion (gBm) as given in [16]. The frequency, spinning reserve control, EV and DR output is analysed with L_1, L_2 and L_∞ norms of the signals, obtained from Monte Carlo simulations of the stochastic renewable energy and

packet drop rates. The signal norms are analysed using bivariate density plots and nonparametric statistical tests.

This paper is structured into three primary sections before we head to simulation and results:

- Section 2 describes the state-space model of diverse smart grid configurations, incorporating DR and EVs in both centralized and decentralized scenarios.
- Section 3 elaborates on the discretization of the generalized state-space models outlined in Section 2, at a specified sampling time. Then the formulation of NCS as a switched system model is derived for a given controller and observer gain. This consideration encompasses packet dropouts in both the feedforward and feedback pathways.
- In Section 4, the Lyapunov stability criteria are employed, utilizing common quadratic Lyapunov matrices to determine the controller and observer gain respectively, ensuring bounded H_∞ norm against input disturbances. This ensures stability of the switched system derived in Section 3 across varying rates. The LMI condition derived for solution is akin to our prior work in [57].
- Section 5 presents numerical results, incorporating diverse state-space models introduced in Section 2. The results are obtained using the controller and observer gain respectively, derived from solving the LMI. Additionally, the analysis encompasses various packet drop rates and includes stochastic renewable energy and load demand models.

2. Load frequency control with demand response and electric vehicle

The state space model used in this paper is a reduced version of the complex power system dynamics [70] to analyse the nonlinearities induced by the packet drop models. The reduction methodology is similar to the reduction of nonlinear two-layer liquid lattice process [71] and wave processes in oceanography, acoustics and hydrodynamics [72] into simpler ordinary differential equations (ODEs). The generalized one area LFC, similar to the schematic used in [19] is shown in Fig. 1. The two inputs of the EV represent the decentralized and centralized participation in the LFC structure respectively where both of them are not considered at once. The scheme is similar to the decentralized control for the i^{th} area in the power system decoupled from other geographical areas. This schematic can also be considered as a micro-grid operating in a small geographical region. Single control area is considered in this paper as the LMIs derived in the later sections are too restrictive, and it is a challenging task to obtain an acceptable solution with higher-order systems. In this paper, we do not consider the unit commitment and deregulated environment with associated task allocations since this will overcomplicate the analytical stability studies currently under investigation. Although here the stability analysis is considered with i^{th} area as a representative case, for large interconnected smart grids with many areas, the system matrices will be bigger. Although the NCS design method is generic, due to restrictive nature of the LMI algorithm, it may not produce any feasible stabilizing solution. Therefore, in order study the possible cyber-physical security problems, we proceed with a single area-based analysis.

2.1. Load frequency control state space model

The model of the power system is inherently nonlinear. However, linearized models of LFC are acceptable for analysis because the load fluctuations are usually quite small. The simplified LFC model consisting of the governor, non-reheated turbine, along with the electrical machine models with load fluctuations as state disturbance, is represented as a linear state-space model as follows:

$$\Delta\dot{f}_i(t) = -\frac{D_i}{M_i}\Delta f_i(t) + \frac{1}{M_i}\Delta P_{m_i}(t) - \frac{1}{M_i}\Delta P_L(s), \tag{1}$$

$$\Delta\dot{P}_{m_i}(t) = -\frac{1}{T_{t_i}}\Delta P_{m_i}(t) + \frac{1}{T_{t_i}}\Delta P_{G_i}(t), \tag{2}$$

$$\Delta\dot{P}_{g_i}(t) = -\frac{1}{R_i T_{g_i}}\Delta f_i(t) - \frac{1}{T_{g_i}}\Delta P_{g_i}(t) + \frac{1}{T_{g_i}}\Delta u_{c_i}(t), \tag{3}$$

$$\frac{d}{dt}\left[\beta_i \int \Delta f_i(t)dt\right] = \beta_i \Delta f_i(t). \tag{4}$$

Here, T_{t_i} and T_{g_i} represent the time constant of the governor and turbine, respectively. R_i represents the droop constant of the primary control loop. D_i is the damping coefficient of the system, and H_i is the equivalent system inertia. T_d represents the fixed equivalent delay in the demand response side. Here, Δu_C represents the control input to the

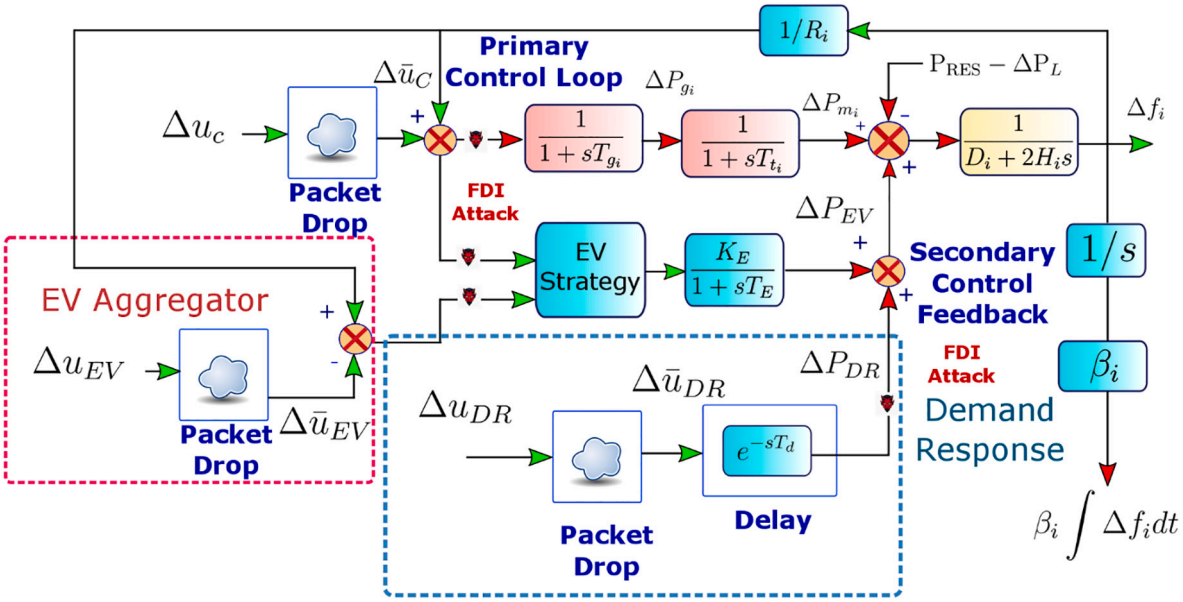

Fig. 1. Schematic of load frequency control with different strategies of EV and demand response. Packet dropout and FDI attacks are shown at relevant places.

governor. As shown in Fig. 1, the governor, turbine, and power system time constants govern the grid frequency dynamics. The droop component (R_i) is a part of the primary control loop, which acts upon the frequency deviation Δf_i. The primary feedback loop will activate the necessary over-frequency and under-frequency relays in the thermal power station. The term $\beta_i \int \Delta f_i(t)dt$ represents the power needed to stabilize the frequency fluctuations Δf_i, which is utilized in the secondary control loop. It can also be considered a cumulative disturbance due to the frequency fluctuations in other areas, as given in [61]. The value of the parameters used in the state-space model (1)–(4) is adopted from [37]. The model (1)–(4) can be written in the form:

$$\begin{aligned} \dot{\mathbf{x}}(t) &= \mathbf{A}\mathbf{x}(t) + \mathbf{B}_1 u(t) + \mathbf{B}_2 w(t), \\ \mathbf{y}(t) &= \mathbf{C}\mathbf{x}(t) + \mathbf{D}n(t). \end{aligned} \tag{5}$$

Here, $\mathbf{A}$ is the system matrix, $\mathbf{B}_1$ is the control input matrix, $\mathbf{B}_2$ is the disturbance matrix, $\mathbf{C}$ is the observation matrix and $\mathbf{D}$ is the noise matrix. Moreover, $\mathbf{x}(t)$ is the state vector, $\mathbf{u}(t)$ is the input vector, $w(t) \in L_2[0,\infty)$ is the disturbance vector, $\mathbf{y}(t)$ is the system output and $n(t) \in L_2[0,\infty)$ is the output noise vector. Since we are designing an observer-based controller here, it is essential to measure certain states to make the system observable. Corresponding to (1)–(4), we can write the system matrices as follows:

$$\mathbf{A} = \begin{bmatrix} -\frac{D_i}{M_i} & \frac{1}{M_i} & 0 & 0 \\ 0 & -\frac{1}{T_{t_i}} & \frac{1}{T_{t_i}} & 0 \\ -\frac{1}{RT_{g_i}} & 0 & -\frac{1}{T_{g_i}} & 0 \\ 0 & 0 & 0 & 1 \end{bmatrix}, \mathbf{B}_1 = \begin{bmatrix} 0 \\ 0 \\ \frac{1}{T_{g_i}} \\ 0 \end{bmatrix}, \mathbf{B}_2 = \begin{bmatrix} -\frac{1}{M_i} \\ 0 \\ 0 \\ 0 \end{bmatrix}, \tag{6}$$

where, input states: $\mathbf{x} = \begin{bmatrix} \Delta f_i(t) & \Delta P_{m_i}(t) & \Delta P_{g_i}(t) & \beta \int \Delta f_i(t)dt \end{bmatrix}^T$, system output $\mathbf{y} = \begin{bmatrix} \Delta f(t) & \beta \int \Delta f(t)dt \end{bmatrix}^T$, control input: $\mathbf{u} = \Delta u_{c_i}(t)$ and disturbance input $\mathbf{w} = \begin{bmatrix} \Delta P_L & d_{\text{FDI}} \end{bmatrix}^T$. Here ΔP_L and d_{FDI} represent the load and FDI attack disturbance vector.

The output vector is chosen such that the observability condition is satisfied i.e.

$$\text{rowrank}\left(\begin{bmatrix} \mathbf{C} \\ \mathbf{CA} \\ \mathbf{CA}^2 \\ \vdots \\ \mathbf{CA}^{n-1} \end{bmatrix}\right) = n. \tag{7}$$

2.2. Load frequency control with demand response

In this subsection, we consider time delays in the demand response. Although many contemporary literatures have studied LFC with time delays in the primary and secondary loops, here the delay in demand response is significantly larger than rest of the NCS. This is because the delay in demand response involves multiple stages of information processing and consumer's decision based on tariff which are not typically communication delays on NCS. The power balance equation with the inclusion of demand response is written, as shown in Fig. 1:

$$\Delta P_{m_i}(s) + \Delta u_{DR}(s)G(s) - \Delta P_L(s) = 2H_i s\Delta f_i(s) + D_i \Delta f_i(s), \tag{8}$$

where, $G(s)$ represents the Pade approximation of the time delay induced by the demand response. IEEE Std 2030.6- 2016 [73], suggests that the delay time is the cumulative sum of notification time sent to the consumer from the aggregator and the consumer response time. For the sake of simplicity, here 2nd order Pade approximation of the delay is considered. Moreover, in [19], the performance change is negligible with the reduction in the order of the Pade. The second-order Pade approximation e^{-sT_d} is given as [74]:

$$G(s) = \frac{T_d^2 s^2 - 6T_d s + 12}{T_d^2 s^2 + 6T_d s + 12}. \tag{9}$$

Now let us consider: $X_{\text{temp}}(s) = \Delta \overline{u}_{DR_i}(s)G(s)$.

Hence, we can write:

$$\begin{aligned} X_{\text{temp}}(s) &= G_1(s) \cdot \Delta \overline{u}_{DR}(s) \\ &= \left(\left(s^2 - \frac{6s}{T_d} + \frac{12}{T_d^2} \right) \Big/ \left(s^2 + \frac{6s}{T_d} + \frac{12}{T_d^2} \right) \right) \cdot \Delta \overline{u}_{DR}(s). \end{aligned} \tag{10}$$

The above expression can be written as:

$$X_{\text{temp}}(s) = \Delta \overline{u}_{DR}(s) + X_1(s), \tag{11}$$

where,

$$X_1(s) = -\left(\left(\frac{12s}{T_d} \right) \Big/ \left(s^2 + \frac{6s}{T_d} + \frac{12}{T_d^2} \right) \right) \Delta \overline{u}_{DR}(s). \tag{12}$$

Now, let us consider $X_2(s) = \frac{1}{s} \cdot X_1(s)$. Hence, we can write $x_2(t)$ as:

$$\dot{x}_2(t) = x_1(t). \tag{13}$$

Substituting the value of $x_2(t)$ in (11) and writing the equation in the time domain, we get:

$$\dot{x}_1(t) = -\frac{6}{T_d} x_1(t) - \frac{12}{T_d^2} x_2(t) - \frac{12}{T_d} L^{-1}[\Delta \overline{u}_{DR}(s)]. \tag{14}$$

Here, $L^{-1}[.]$ represent the inverse Laplace transform.

Thus, two new state variables $x_1(t)$ and $x_2(t)$ are incorporated in the state-space model due to the second-order Pade approximation of the time delay. The time delay T_d considered in this paper is 1 s. The new states in (13)–(14) is incorporated along with (1)–(4) to form the following state-space model for LFC with demand response:

$$\begin{aligned} \mathbf{A} &= \begin{bmatrix} -\frac{D_i}{M_i} & \frac{1}{M_i} & 0 & 0 & \frac{1}{M_i} & 0 \\ 0 & -\frac{1}{T_{t_i}} & \frac{1}{T_{t_i}} & 0 & 0 & 0 \\ -\frac{1}{R_i T_{g_i}} & 0 & -\frac{1}{T_{g_i}} & 0 & 0 & 0 \\ 0 & 0 & 0 & 1 & 0 & 0 \\ 0 & 0 & 0 & 0 & -\frac{6}{T_d} & -\frac{12}{T_d^2} \\ 0 & 0 & 0 & 0 & 1 & 0 \end{bmatrix}, \mathbf{B}_1 = \begin{bmatrix} 0 & \frac{1}{M_i} \\ 0 & 0 \\ \frac{1}{T_{g_i}} & 0 \\ 0 & 0 \\ 0 & -\frac{12}{T_{d_i}} \\ 0 & 0 \end{bmatrix}, \mathbf{B}_2 \\ &= \begin{bmatrix} -\frac{1}{M_i} \\ 0 \\ 0 \\ 0 \\ 0 \\ 0 \end{bmatrix}, \end{aligned} \tag{15}$$

where, input states $\mathbf{x} = \begin{bmatrix} \Delta f_i(t) & \Delta P_{m_i}(t) & \Delta P_{g_i}(t) & \beta_i \int \Delta f_i(t)dt & x_1(t) & x_2(t) \end{bmatrix}^T$, output variables $\mathbf{y} = \begin{bmatrix} \Delta f_i(t) & \beta \int \Delta f_i(t)dt \end{bmatrix}^T$, control input $\mathbf{u} = \begin{bmatrix} \Delta u_{c_i}(t) & \Delta u_{DR}(t) \end{bmatrix}^T$ and disturbance input $\mathbf{w} = \begin{bmatrix} \Delta P_L & d_{\text{FDI}} \end{bmatrix}^T$.

2.3. Load frequency control with centralized and decentralized EV connection

From Fig. 1, we can write the EV power output ΔP_{EV} as in [37]:

$$\Delta \dot{P}_E(t) = -\frac{1}{R_i T_E}\Delta f_i(t) - \frac{1}{T_E}\Delta P_E(t) + \frac{K_E}{T_E}\Delta u_{St}(t). \tag{16}$$

Here, K_E and T_E are the gain and time constant of the EV module respectively. The $\Delta u_{St}(t)$ depends on whether it is coupled to spinning reserves or regulated independently from a decentralized strategy, which can be characterized as:

$$\Delta u_{st}(t) = \begin{cases} \Delta u_C(t), & \text{EV Strategy} = \text{Centralized}, \\ \Delta u_{EV}(t), & \text{EV Strategy} = \text{Decentralized}. \end{cases} \tag{17}$$

The parameters of the EV model defined in (16) are adapted from [37]. Hence we combine the power generator's LFC model in (1)–(4) with the EV model in (16), to write the state space model of the form (5), with centralized strategy as:

$$\mathbf{A} = \begin{bmatrix} -\frac{D_i}{M_i} & \frac{1}{M_i} & 0 & 0 & 0 \\ 0 & -\frac{1}{T_{t_i}} & \frac{1}{T_{t_i}} & 0 & 0 \\ -\frac{1}{R_i T_{g_i}} & 0 & -\frac{1}{T_{g_i}} & 0 & 0 \\ 0 & 0 & 0 & 1 & 0 \\ -\frac{1}{R_i T_E} & 0 & 0 & 0 & -\frac{1}{T_E} \end{bmatrix}, \mathbf{B}_1 = \begin{bmatrix} 0 \\ 0 \\ \frac{1}{T_{g_i}} \\ 0 \\ \frac{K_E}{T_E} \end{bmatrix}, \mathbf{B}_2 = \begin{bmatrix} -\frac{1}{M_i} \\ 0 \\ 0 \\ 0 \\ 0 \end{bmatrix}. \tag{18}$$

Here, states: $\mathbf{x} = \begin{bmatrix} \Delta f_i(t) & \Delta P_{m_i}(t) & \Delta P_{g_i}(t) & \beta_i \int \Delta f_i(t)dt & \Delta P_{E_i}(t) \end{bmatrix}^T$, output variable:$\mathbf{y} = \begin{bmatrix} \Delta f_i(t) & \beta_i \int \Delta f_i(t)dt & \Delta P_E(t) \end{bmatrix}^T$, control input: $\mathbf{u} = \Delta u_c(t)$ and disturbance input: $\mathbf{w} = \begin{bmatrix} \Delta P_L & d_{\text{FDI}} \end{bmatrix}^T$.

We observe that we need to incorporate the change in EV output $\Delta P_E(t)$ in the output vector to satisfy the observability condition (7). Therefore, for decentralized EV configuration, the $\mathbf{A}$ and $\mathbf{B}_2$ remains the same as (18) and $\mathbf{B}_1$ is modified as follows:

$$\mathbf{B}_1 = \begin{bmatrix} 0 & 0 \\ 0 & 0 \\ \frac{1}{T_{g_i}} & 0 \\ 0 & 0 \\ 0 & \frac{K_E}{T_E} \end{bmatrix}. \tag{19}$$

It is seen that, for decentralized configuration, we have two control inputs in this configuration $\mathbf{u} = \begin{bmatrix} \Delta u_c(t) & \Delta u_{\text{EV}}(t) \end{bmatrix}^T$.

2.4. LFC with demand response and centralized/decentralized EV configuration

In this case, we combine all the state space equations of traditional LFC from (1)–(4) and the new state-space variables obtained from demand response (13) and the EV model (16) with the configuration strategy defined in (17). We can write the state space equation of LFC, DR and with centralized EV configuration as:

$$\mathbf{A} = \begin{bmatrix} -\frac{D_i}{M_i} & \frac{1}{M_i} & 0 & 0 & \frac{1}{M_i} & 0 & 0 \\ 0 & -\frac{1}{T_{t_i}} & \frac{1}{T_{t_i}} & 0 & 0 & 0 & 0 \\ -\frac{1}{R_i T_{g_i}} & 0 & -\frac{1}{T_{g_i}} & 0 & 0 & 0 & 0 \\ 0 & 0 & 0 & 1 & 0 & 0 & 0 \\ 0 & 0 & 0 & 0 & -\frac{6}{T_d} & -\frac{12}{T_d^2} & 0 \\ 0 & 0 & 0 & 0 & 1 & 0 & 0 \\ -\frac{1}{R_i T_E} & 0 & 0 & 0 & 0 & 0 & -\frac{1}{T_E} \end{bmatrix}, \mathbf{B}_1$$

$$= \begin{bmatrix} 0 & \frac{1}{M} \\ 0 & 0 \\ \frac{1}{T_{g_i}} & 0 \\ 0 & 0 \\ 0 & -\frac{12}{T_d} \\ 0 & 0 \\ \frac{K_E}{T_E} & 0 \end{bmatrix}, \mathbf{B}_2 = \begin{bmatrix} -\frac{1}{M_i} \\ 0 \\ 0 \\ 0 \\ 0 \\ 0 \\ 0 \end{bmatrix}, \tag{20}$$

where, input states: $\mathbf{x} = \begin{bmatrix} \Delta f_i(t) & \Delta P_{m_i}(t) & \Delta P_{g_i}(t) & \beta_i \int \Delta f_i(t)dt x_1(t) x_2(t) \Delta P_E(t) \end{bmatrix}^T$, output variables: $\mathbf{y} = \begin{bmatrix} \Delta f_i(t) & \beta_i \int \Delta f_i(t)dt \Delta P_E(t) \end{bmatrix}^T$, control input: $\mathbf{u} = \begin{bmatrix} \Delta u_c(t) & \Delta u_{DR}(t) \end{bmatrix}^T$ and disturbance input: $\mathbf{w} = \begin{bmatrix} \Delta P_L & d_{\text{FDI}} \end{bmatrix}^T$.

Similar to the previous subsection, for decentralized EV configuration, $\mathbf{A}$ and $\mathbf{B}_2$ remains the same as (20), but $\mathbf{B}_1$ changes as follows, satisfying observability condition (7):

$$\mathbf{B}_1 = \begin{bmatrix} 0 & \frac{1}{M} & 0 \\ 0 & 0 & 0 \\ \frac{1}{T_g} & 0 & 0 \\ 0 & 0 & 0 \\ 0 & -\frac{12}{T_d} & 0 \\ 0 & 0 & 0 \\ 0 & 0 & \frac{K_E}{T_E} \end{bmatrix}, \tag{21}$$

where, $\mathbf{u} = \begin{bmatrix} \Delta u_c(t) & \Delta u_{DR}(t) & \Delta u_{EV}(t) \end{bmatrix}^T$.

However, in order to design the observer based state feedback controller under random packet drop, the continuous-time state-space system for different LFC, DR and EV configurations defined in (6), (15), (18)–(19) and (20)–(21) need to be converted into discrete-time domain with a specified sampling time T_s. Hence, as per [75], the continuous time state-space can be represented in discrete-time domain with specified T_s as:

$$\begin{aligned} \mathbf{x}(k+1) &= \mathbf{F}\mathbf{x}(k) + \mathbf{G}_1\bar{u}(k) + \mathbf{G}_2 w(k), \\ \mathbf{y}(k) &= \mathbf{C}\mathbf{x}(k) + \mathbf{D}n(k), \end{aligned} \tag{22}$$

where,

$$\mathbf{F} = e^{\mathbf{A}T_s}, \mathbf{G}_1 = \int_0^{T_s} e^{\mathbf{A}T_s}\mathbf{B}_1 dt, \mathbf{G}_2 = \int_0^{T_s} e^{\mathbf{A}T_s}\mathbf{B}_2 dt. \tag{23}$$

The stabilizing controller and observer for the system defined by (22) under random packet drop and external disturbances are derived in the next section. In (22), $\bar{u}(k)$ represents the control output from the communication network. The concept of probabilistic observability is not used to analyse the system as given in [54]. Instead, the switched system is modelled, and joint observer and controller gains are obtained to ensure its stability based on the arbitrary number of packet drops, which is explained in the following sections.

3. Switched system modelling under packet dropout with observer and controller gain

The controller and observer used for the system (22) are shown in Fig. 2. Generally, the observer at the control centre receives the measured signal from the communication channel to estimate the given states $\hat{\mathbf{x}}(k)$ for the next time instant. The state feedback controller gain $\mathbf{K}$ has to be obtained from the estimated states to generate control signals. As shown in Fig. 2, the controller is derived from the observer, whose form is given as:

$$\begin{aligned} \hat{\mathbf{x}}(k+1) &= \mathbf{F}\hat{\mathbf{x}}(k) + \mathbf{G}_1\mathbf{u}(k) + \mathbf{L}(\bar{y}(k) - \hat{y}(k)), \\ \hat{\mathbf{y}}(k) &= \mathbf{C}\hat{\mathbf{x}}(k). \end{aligned} \tag{24}$$

Here, $\bar{y}(k)$ represents the output received by the observer after the feedback network effect to estimate the state variables $\hat{\mathbf{x}}(k)$ using observer gain $\mathbf{L}$ and $\hat{y}(k)$ represents the observed output. The control input $\mathbf{u}(k)$ is defined as:

$$\mathbf{u}(k) = -\mathbf{K}\hat{\mathbf{x}}(k). \tag{25}$$

The state estimation error of the dynamical system, i.e. $\mathbf{e}(k) = \mathbf{x}(k) - \hat{\mathbf{x}}(k)$, where $\mathbf{x}(k)$ is obtained from the discretized system model (22) and $\hat{\mathbf{x}}(k)$ is obtained from the observer equation in (24), which play an essential role in deciding the performance of the NCS. The estimation error of the dynamical system governed by the observer gain $\mathbf{L}$ should be much faster than the closed-loop system response obtained from the state feedback control gain $\mathbf{K}$ [75]. Ideally, it should be four to five times faster for optimum system response. Physically, an observer is a computer program; hence it is possible to increase the response speed so that the estimated state converges to the true state. However, the error dynamical system response is constrained by the noise and the sensitivity issues present in the system.

As described in [76], there are two ways to model packet dropout in the literature. In the first method, the dropouts follow a particular probability distribution and a stochastic model like the Markovian jump linear system is utilized to describe the NCS. The second approach is deterministic, where packet dropouts can be specified in time average sense or maximum value. An ADS with a rate constraint on the deterministic events i.e. effective packet transmission [77] represents this approach, based on the CQLF approach. Thus, the packet dropouts in both the feedback and forward path are considered as events; hence the NCS can be considered as a discrete time switched system. Here, the switched system means the hybrid dynamical system, having a finite number of subsystems, which are modelled using different packet transmission scenarios in both the feedback and forward path of the NCS. A logical rule is used to facilitate switching between the subsystems. The switched system stability studies with arbitrary switching signals have been performed here as per [78,79]. As shown in [80], the switched system has to be modelled so that the controller and observer use the previously transmitted information to stabilize the system and estimate the system states, respectively. A time-driven observer is utilized to design a state feedback controller (25), as ADS under random packet dropouts as given in [68] with certain assumptions as follows:

- The data packets are time-stamped, containing the information of the sampling instant when it is sampled. As given in IEEE Standard 1815–2012 [63], the DNP3 protocol supports data time-stamping, aiding the utilities to collect historical data.
- The sensor clock is considered as the reference. For load frequency control, the PMU clock can be considered.
- Both the controller and actuator are time driven.

The packet transmission from the controller to the actuator (in the forward path) and sensor to the observer (in the feedback path) is shown in Fig. 1 and Fig. 2, respectively. We have considered the FDI attack in the governor input of the primary control loop, input of the EV strategy and by manipulating the output of the demand response, to simulate a realistic scenario of NCS under cyber-attack. The aim of this paper is to

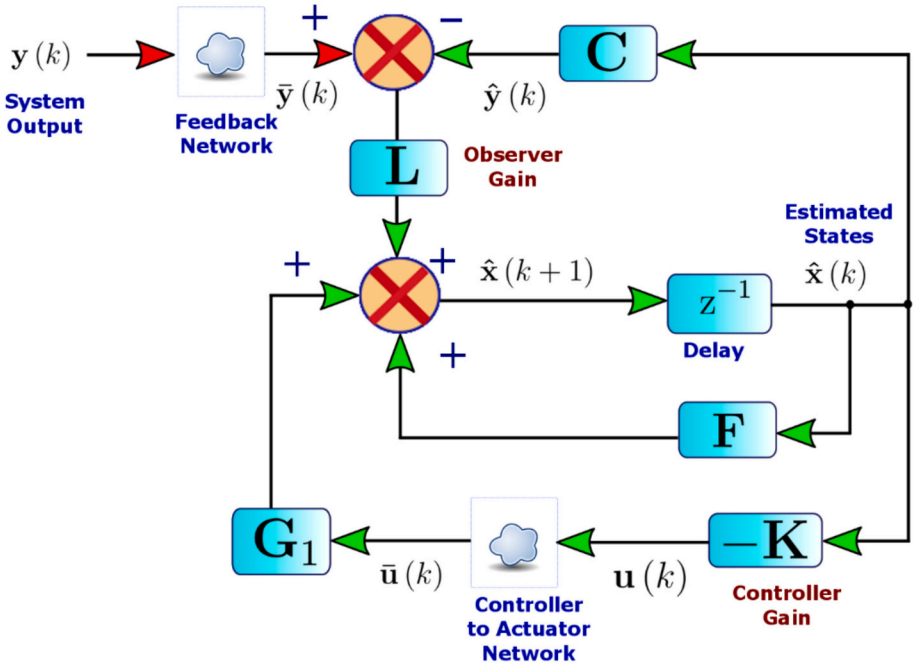

Fig. 2. Schematic of the observer-based controller for the decentralized load frequency control system. The packet drops at feedback and feedforward are also shown in the schematic, which helps obtain the derivations of the switched system model for stability analysis.

design a robust control strategy so that it can ensure the stability even with an FDI attack and high percentage of packet dropout, which are validated by credible Monte Carlo simulations. It is assumed that two switches, i.e. s_1 and s_2 respectively, can represent the network in the feedback and forward path of the control loop. Depending on the switch position, system output $y(k)$ and control input $u(k)$ at time instant k can be modelled using Boolean variables, $s_1(\bar{s}_1), s_2(\bar{s}_2)$, which is represented as:

$$\left.\begin{array}{lll} s_1: & \bar{y}(k)=y(k) & \text{for effective transmission} \\ \bar{s}_1: & \bar{y}(k)=\bar{y}(k-1) & \text{for ineffective transmission} \\ s_2: & \bar{u}(k)=u(k)=-\mathbf{K}\widehat{\mathbf{x}}(k) & \text{for effective transmission} \\ \bar{s}_2: & \bar{u}(k)=\bar{u}(k-1)=-\mathbf{K}\widehat{\mathbf{x}}(k-1) & \text{for ineffective transmission} \end{array}\right\}, \tag{26}$$

where, $s_1(\bar{s}_1)$ represents the close (open) position of the switch s_1 in the feedback path and $s_2(\bar{s}_2)$ represents the close (open) position of the switch s_2 in the forward path. As per Boolean switch configuration (26), four possible subsystems can be formulated as an ADS with the Boolean combinations (s_1,s_2), $(\bar{s}_1,s_2)$, $(s_1,\bar{s}_2)$, $(\bar{s}_1,\bar{s}_2)$. The resulting NCS from these combinations is represented as an ADS. It has a rate constraint (r) using the subsystems represented by $\mathbf{\Phi}_{\sigma(k)}, \sigma(k)=1,2,3,4$ as:

$$\begin{aligned} &\mathbf{z}(k+1)=\mathbf{\Phi}_{\sigma(k)}\mathbf{z}(k)+\mathbf{\Gamma}_{\sigma(k)}\boldsymbol{\eta}(k), \quad \sigma(k)=1,2,3,4 \\ &\widetilde{y}_z(k)=\widetilde{\mathbf{C}}\mathbf{z}(k), \end{aligned} \tag{27}$$

where, $\mathbf{z}(k), \boldsymbol{\eta}(k)$ represents the augmented system states, input states, and $\widetilde{y}, \widetilde{\mathbf{C}}$ represents the output, output matrix of the subsystems. The stability of the state estimation error for the switched system (27) deploying a Luenberger observer, is obtained by finding a CQLF using LMIs [81,82]. In the following subsection, subsystems of the switched systems are derived for different switching conditions.

3.1. Case 1: no packet drop condition

As per the switching condition $\{s_1, s_2\}$, the system output and control input is represented using (26) as:

$$\begin{aligned} &\bar{y}(k)=y(k)=\mathbf{C}\mathbf{x}(k)+\mathbf{D}n(k), \\ &\bar{u}(k)=u(k)=-\mathbf{K}\widehat{\mathbf{x}}(k). \end{aligned} \tag{28}$$

The state estimation error $\mathbf{e}(k)$ is represented as:

$$\mathbf{e}(k)=\mathbf{x}(k)-\widehat{\mathbf{x}}(k). \tag{29}$$

From the discrete-time systems in (22), and substituting the estimation error $\mathbf{e}(k)$ in (29) we can write:

$$\mathbf{x}(k+1)=(\mathbf{F}-\mathbf{G}_1K)\mathbf{x}(k)+\mathbf{G}_1\mathbf{K}\mathbf{e}(k)+\mathbf{G}_2w(k). \tag{30}$$

Similarly, we can write the discrete-time system at time instant $(k-1)$ as:

$$\mathbf{x}(k)=\mathbf{F}\mathbf{x}(k-1)+\mathbf{G}_1\bar{u}(k-1)+\mathbf{G}_2w(k-1). \tag{31}$$

The corresponding state estimation error is derived as:

$$\begin{aligned} &\mathbf{e}(k+1)=\mathbf{x}(k+1)-\widehat{\mathbf{x}}(k+1) \\ &\Rightarrow\mathbf{e}(k+1)=[\mathbf{F}\mathbf{x}(k)+\mathbf{G}_1\bar{u}(k)+\mathbf{G}_2w(k)]-[\mathbf{F}\widehat{\mathbf{x}}(k)+\mathbf{G}_1u(k)+\mathbf{L}(\bar{y}(k)-\widehat{y}(k))] \\ &\Rightarrow\mathbf{e}(k+1)=[\mathbf{F}\mathbf{x}(k)+\mathbf{G}_1u(k)+\mathbf{G}_2w(k)]-[\mathbf{F}\widehat{\mathbf{x}}(k)+\mathbf{G}_1u(k)+\mathbf{L}(y(k)-\mathbf{C}\widehat{\mathbf{x}}(k))] \\ &\Rightarrow\mathbf{e}(k+1)=[\mathbf{F}\mathbf{x}(k)+\mathbf{G}_2w(k)]-[\mathbf{F}\widehat{\mathbf{x}}(k)+\mathbf{L}(\mathbf{C}\mathbf{x}(k)+\mathbf{D}n(k)-\mathbf{C}\widehat{\mathbf{x}}(k))] \\ &\Rightarrow\mathbf{e}(k+1)=[\not{\mathbf{F}}\mathbf{x}(k)+\mathbf{G}_2w(k)]-[\mathbf{F}(\not{\mathbf{x}}(k)-\mathbf{e}(k))+\mathbf{L}(\mathbf{C}\mathbf{e}(k)+\mathbf{D}n(k))] \\ &\Rightarrow\mathbf{e}(k+1)=[\mathbf{F}-\mathbf{L}\mathbf{C}]\mathbf{e}(k)+\mathbf{G}_2w(k)-\mathbf{L}\mathbf{D}n(k). \end{aligned} \tag{32}$$

Similarly (28), we can write $\bar{u}(k)$ as:

$$\bar{u}(k)=-\mathbf{K}\mathbf{x}(k)+\mathbf{K}\mathbf{e}(k). \tag{33}$$

Now, let us define the augmented states as:

$\mathbf{z}=[\,\mathbf{x}(k) \quad \mathbf{x}(k-1) \quad \mathbf{e}(k) \quad \bar{u}(k-1)\,]^T$ and $\boldsymbol{\eta}(k)=[\,w(k) \quad w(k-1) \quad n(k) n(k-1)\,]^T$..

The NCS (27) can be formulated using (30)–(33) as:

$$\begin{aligned} \mathbf{z}(k+1)&=\mathbf{\Phi}_1\mathbf{z}(k)+\mathbf{\Gamma}_1\boldsymbol{\eta}(k) \\ &=\begin{bmatrix} \mathbf{F}-\mathbf{G}_1\mathbf{K} & 0 & \mathbf{G}_1\mathbf{K} & 0 \\ 0 & \mathbf{F} & 0 & \mathbf{G}_1 \\ 0 & 0 & \mathbf{F}-\mathbf{L}\mathbf{C} & 0 \\ -\mathbf{K} & 0 & \mathbf{K} & 0 \end{bmatrix}\mathbf{z}(k)+\begin{bmatrix} \mathbf{G}_2 & 0 & 0 & 0 \\ 0 & \mathbf{G}_2 & 0 & 0 \\ \mathbf{G}_2 & 0 & -\mathbf{L}\mathbf{D} & 0 \\ 0 & 0 & 0 & 0 \end{bmatrix}\boldsymbol{\eta}(k). \end{aligned} \tag{34}$$

3.2. Case 2: packet drop in the feedback path

Under this condition, i.e.$\{\bar{s}_1, s_2\}$ the system output becomes:

$$\bar{y}(k)=\bar{y}(k-1)=\mathbf{C}\mathbf{x}(k-1)+\mathbf{D}n(k-1). \tag{35}$$

The terms $\mathbf{x}(k+1), \mathbf{x}(k), \bar{u}(k)$ will remain the same as given in (30), (31) and (33) respectively. The estimation error $\mathbf{e}(k+1)$ can be written as:

$$\begin{aligned} &\Rightarrow\mathbf{e}(k+1)=[\mathbf{F}\mathbf{x}(k)+\mathbf{G}_1u(k)+\mathbf{G}_2w(k)\,]-[\mathbf{F}\widehat{\mathbf{x}}(k)+\mathbf{G}_1u(k)+\mathbf{L}(\mathbf{C}\mathbf{x}(k-1)+\mathbf{D}n(k-1)-\mathbf{C}\widehat{\mathbf{x}}(k)\,)\,] \\ &\Rightarrow\mathbf{e}(k+1)=\mathbf{F}\mathbf{e}(k)+\mathbf{L}\mathbf{C}\widehat{\mathbf{x}}(k)-\mathbf{L}\mathbf{C}\mathbf{x}(k-1)-\mathbf{L}\mathbf{D}n(k-1)+\mathbf{G}_2w(k) \\ &\Rightarrow\mathbf{e}(k+1)=\mathbf{F}\mathbf{e}(k)+\mathbf{L}\mathbf{C}[\mathbf{x}(k)-\mathbf{e}(k)\,]-\mathbf{L}\mathbf{C}\mathbf{x}(k-1)-\mathbf{L}\mathbf{D}n(k-1)+\mathbf{G}_2w(k) \\ &\Rightarrow\mathbf{e}(k+1)=[\mathbf{L}\mathbf{C}]\mathbf{x}(k)+[\mathbf{F}-\mathbf{L}\mathbf{C}]\mathbf{e}(k)-\mathbf{L}\mathbf{C}\mathbf{x}(k-1)-\mathbf{L}\mathbf{D}n(k-1)+\mathbf{G}_2w(k). \end{aligned} \tag{36}$$

Using (30), (31), (33), (36), the matrix $\mathbf{\Phi}_2$ and $\mathbf{\Gamma}_2$ in (27) can be written from the augmented states as:

$$\mathbf{\Phi}_2=\begin{bmatrix} \mathbf{F}-\mathbf{G}_1\mathbf{K} & 0 & \mathbf{G}_1\mathbf{K} & 0 \\ 0 & \mathbf{F} & 0 & \mathbf{G}_1 \\ \mathbf{L}\mathbf{C} & -\mathbf{L}\mathbf{C} & \mathbf{F}-\mathbf{L}\mathbf{C} & 0 \\ -\mathbf{K} & 0 & \mathbf{K} & 0 \end{bmatrix}, \mathbf{\Gamma}_2=\begin{bmatrix} \mathbf{G}_2 & 0 & 0 & 0 \\ 0 & \mathbf{G}_2 & 0 & 0 \\ \mathbf{G}_2 & 0 & 0 & -\mathbf{L}\mathbf{D} \\ 0 & 0 & 0 & 0 \end{bmatrix}. \tag{37}$$

3.3. Case 3: packet drop in the feedforward path

For $\{s_1, \bar{s}_2\}$, i.e. packet drop occurring in the forward path only, we get:

$$\bar{u}(k)=\bar{u}(k-1). \tag{38}$$

Thus we can write $\mathbf{x}(k+1)$ from (22) as:

$$\mathbf{x}(k+1)=\mathbf{F}\mathbf{x}(k)+\mathbf{G}_1\bar{u}(k-1)+\mathbf{G}_2w(k). \tag{39}$$

The term $\mathbf{x}(k)$ will remain the same as given in (31). The estimation error $\mathbf{e}(k+1)$ can be written as:

$$
\begin{aligned}
&\mathbf{e}(k+1) = \mathbf{x}(k+1) - \widehat{\mathbf{x}}(k+1)\\
&\Rightarrow \mathbf{e}(k+1) = [\mathbf{F}\mathbf{x}(k) + \mathbf{G_1}\bar{u}(k-1) + \mathbf{G_2}w(k)\,] - [\mathbf{F}[\mathbf{x}(k) - \mathbf{e}(k)\,] + \mathbf{G}_1\{\,-\mathbf{K}[\mathbf{x}(k) - \mathbf{e}(k)\,]\,\} + \mathbf{L}(\mathbf{C}\mathbf{x}(k) + \mathbf{D}n(k) - \mathbf{C}\widehat{\mathbf{x}}(k)\,)\,]\\
&\Rightarrow \mathbf{e}(k+1) = [\mathbf{F}\mathbf{x}(k) + \mathbf{G_1}\bar{u}(k-1) + \mathbf{G_2}w(k)\,] - [\mathbf{F}[\mathbf{x}(k) - \mathbf{e}(k)\,] + \mathbf{G}_1\{\,-\mathbf{K}[\mathbf{x}(k) - \mathbf{e}(k)\,]\,\} + \mathbf{L}(\mathbf{C}\mathbf{e}(k) + \mathbf{D}n(k)\,)\,]\\
&\Rightarrow \mathbf{e}(k+1) = [\mathbf{F}\mathbf{x}(k) + \mathbf{G_1}\bar{u}(k-1) + \mathbf{G_2}w(k)\,] - [[\mathbf{F} - \mathbf{G}_1K]\mathbf{x}(k) + [\,-\mathbf{F} + \mathbf{G}_1\mathbf{K} + \mathbf{LC}]\mathbf{e}(k) + [\mathbf{LD}]n(k)\,]\\
&\Rightarrow \mathbf{e}(k+1) = [\cancel{\mathbf{F}} - \cancel{\mathbf{F}} + \mathbf{G_1}\mathbf{K}]\mathbf{x}(k) + [\mathbf{F} - \mathbf{G}_1K - \mathbf{LC}]\mathbf{e}(k) + \mathbf{G_2}w(k) - \mathbf{LD}n(k) + \mathbf{G_1}\bar{u}(k-1)\\
&\Rightarrow \mathbf{e}(k+1) = \mathbf{G}_1\mathbf{K}\mathbf{x}(k) + [\mathbf{F} - \mathbf{G_1}\mathbf{K} - \mathbf{LC}]\mathbf{e}(k) + \mathbf{G_1}\bar{u}(k-1) + \mathbf{G_2}w(k) - \mathbf{LD}n(k).
\end{aligned}
\tag{40}
$$

Using (31), (40) the matrix $\mathbf{\Phi}_3$ and $\mathbf{\Gamma}_3$ in (27) can be written from the augmented states as:

$$
\mathbf{\Phi}_3 = \begin{bmatrix} \mathbf{F} & 0 & 0 & \mathbf{G}_1 \\ 0 & \mathbf{F} & 0 & \mathbf{G}_1 \\ \mathbf{G}_1\mathbf{K} & 0 & \mathbf{F} - \mathbf{G}_1\mathbf{K} - \mathbf{LC} & \mathbf{G}_1 \\ 0 & 0 & 0 & \mathbf{I} \end{bmatrix}, \mathbf{\Gamma}_3 = \begin{bmatrix} \mathbf{G}_2 & 0 & 0 & 0 \\ 0 & \mathbf{G}_2 & 0 & 0 \\ \mathbf{G}_2 & 0 & -\mathbf{LD} & 0 \\ 0 & 0 & 0 & 0 \end{bmatrix}.
\tag{41}
$$

3.4. Case 4: packet drop in the feedback and feedforward path

If the packet drop occurs in both the sides (feedback and forward path) of the control loop, i.e. $\{\bar{s}_1, \bar{s}_2\}$, the terms $\mathbf{x}(k+1), \mathbf{x}(k), \bar{u}(k)$ will remain the same as in the previous case. The estimation error $\mathbf{e}(k+1)$ can be written as:

$$
\begin{aligned}
&\Rightarrow \mathbf{e}(k+1) = [\mathbf{F}\mathbf{x}(k) + \mathbf{G_1}\bar{u}(k-1) + \mathbf{G_2}w(k)\,] - [\mathbf{F}\widehat{\mathbf{x}}(k) + \mathbf{G}_1u(k) + \mathbf{L}(\bar{y}(k-1) - \mathbf{C}\widehat{\mathbf{x}}(k)\,)\,]\\
&\Rightarrow \mathbf{e}(k+1) = [\mathbf{F}\mathbf{x}(k) + \mathbf{G_1}\bar{u}(k-1) + \mathbf{G_2}w(k)\,] - [\mathbf{F}\{\mathbf{x}(k) - \mathbf{e}(k)\,\} + \mathbf{G}_1\{\,-\mathbf{K}[\mathbf{x}(k) - \mathbf{e}(k)\,]\,\} + \mathbf{L}(\bar{y}(k-1) - \mathbf{C}\{\mathbf{x}(k) - \mathbf{e}(k)\,\}\,)\,]\\
&\Rightarrow \mathbf{e}(k+1) = [\mathbf{F}\mathbf{x}(k) + \mathbf{G_1}\bar{u}(k-1) + \mathbf{G_2}w(k)\,] - [\{\mathbf{F} - \mathbf{LC} - \mathbf{G}_1\mathbf{K}\}\mathbf{x}(k) + \{\,-\mathbf{F} + \mathbf{G}_1\mathbf{K} + \mathbf{LC}\}\mathbf{e}(k) + \mathbf{L}\bar{y}(k-1)\,]\\
&\Rightarrow \mathbf{e}(k+1) = [\cancel{\mathbf{F}} - \cancel{\mathbf{F}} + \mathbf{LC} + \mathbf{G_1}\mathbf{K}]\mathbf{x}(k) + [\mathbf{F} - \mathbf{G_1}\mathbf{K} - \mathbf{LC}]\mathbf{e}(k) + \mathbf{G_1}\bar{u}(k-1) - \mathbf{L}\bar{y}(k-1) + \mathbf{G_2}w(k)\\
&\Rightarrow \mathbf{e}(k+1) = [\mathbf{LC} + \mathbf{G_1}\mathbf{K}]\mathbf{x}(k) + [\mathbf{F} - \mathbf{G_1}\mathbf{K} - \mathbf{LC}]\mathbf{e}(k) + \mathbf{G_1}\bar{u}(k-1) - \mathbf{L}\bar{y}(k-1) + \mathbf{G_2}w(k)\\
&\Rightarrow \mathbf{e}(k+1) = [\mathbf{LC} + \mathbf{G_1}\mathbf{K}]\mathbf{x}(k) + [\mathbf{F} - \mathbf{G_1}\mathbf{K} - \mathbf{LC}]\mathbf{e}(k) + \mathbf{G_1}\bar{u}(k-1) - \mathbf{L}[\mathbf{C}\mathbf{x}(k-1) + \mathbf{D}n(k-1)\,] + \mathbf{G_2}w(k)\\
&\Rightarrow \mathbf{e}(k+1) = [\mathbf{LC} + \mathbf{G_1}\mathbf{K}]\mathbf{x}(k) + [\mathbf{F} - \mathbf{G_1}\mathbf{K} - \mathbf{LC}]\mathbf{e}(k) + \mathbf{G_1}\bar{u}(k-1) - \mathbf{LC}\mathbf{x}(k-1) - \mathbf{LD}n(k-1) + \mathbf{G_2}w(k).
\end{aligned}
\tag{42}
$$

Using, (31), (38), (39), and (42), the matrix $\mathbf{\Phi}_4$ and $\mathbf{\Gamma}_4$ in (27) can be written from the augmented states as follows:

$$
\begin{aligned}
\mathbf{\Phi}_4 &= \begin{bmatrix} \mathbf{F} & 0 & 0 & \mathbf{G}_1 \\ 0 & \mathbf{F} & 0 & \mathbf{G}_1 \\ \mathbf{LC} + \mathbf{G}_1\mathbf{K} & -\mathbf{LC} & \mathbf{F} - \mathbf{G}_1\mathbf{K} - \mathbf{LC} & \mathbf{G}_1 \\ 0 & 0 & 0 & \mathbf{I} \end{bmatrix}, \mathbf{\Gamma}_4 \\
&= \begin{bmatrix} \mathbf{G}_2 & 0 & 0 & 0 \\ 0 & \mathbf{G}_2 & 0 & 0 \\ \mathbf{G}_2 & 0 & 0 & -\mathbf{LD} \\ 0 & 0 & 0 & 0 \end{bmatrix}.
\end{aligned}
\tag{43}
$$

Therefore, the output of the subsystems can be written as:

$$
\widetilde{y}(k) = \widetilde{\mathbf{C}}\mathbf{z}(k) = [\,\mathbf{C} \quad \mathbf{0} \quad \mathbf{0} \quad \mathbf{0}\,]\mathbf{z}(k).
\tag{44}
$$

4. Stability analysis of NCS using ADS and joint controller/observer design

The procedure aims to find the controller gain for the NCS defined in (27) ensuring guaranteed exponential stability for the system, based on the bounded H_∞ norm. We assume that the fraction of the effective data packet transmission be r_1 and r_2 across the switches s_1 and s_2 respectively. Here, the switches s_1 and s_2 practically represents the situation where the data is transmitted from the PMU measurement to the control centre and load centre for the generation and demand response control system. Let us assume $r_1 = r_2 = r$ (considering same network settings in the forward and feedback path), the effective transmission probabilities R_1, R_2, R_3, R_4 from the sensor to the actuator, for each of the following four cases, can be computed as:

$$
\begin{aligned}
&s_1, s_2 : R_1 = r^2, \qquad \bar{s}_1, s_2 : R_2 = (1-r)r,\\
&s_1, \bar{s}_2 : R_3 = r(1-r), \quad \bar{s}_1, \bar{s}_2 : R_4 = (1-r)(1-r).
\end{aligned}
\tag{45}
$$

Then as per [55], the NCS defined in (27) is exponentially stable under packet drop if the following inequality is satisfied:

$$
\alpha_1^{R_1}\alpha_2^{R_2}\alpha_3^{R_3}\alpha_4^{R_4} > \alpha > 1 \quad : \quad \alpha_1, \alpha_2, \alpha_3, \alpha_4 \in \mathbb{R}_+.
\tag{46}
$$

Hence, we can derive the following theorem:

Theorem 1. *The NCS (27) is exponentially stable with decay rate $\alpha > 0$ under random packet drop rate driven by arbitrary switching signal and external disturbances if there exists a CQLF,* i.e. $\mathbf{P} = \mathbf{P}^T > \mathbf{0}$ *and state feedback controller and observer gains* $\{\mathbf{K}, \mathbf{L}\}$ *with the satisfaction of H_∞ norm bound $\gamma > 0$ by satisfying the following LMIs:*

$$
\begin{bmatrix} \widetilde{\mathbf{C}}^T\widetilde{\mathbf{C}} - \alpha_\sigma^{-2}\mathbf{P} & \mathbf{0} & \mathbf{\Phi}_\sigma^T \\ \mathbf{0} & -\gamma^2\mathbf{I} & \mathbf{\Gamma}_\sigma^T \\ \mathbf{\Phi}_\sigma & \mathbf{\Gamma}_\sigma & -\mathbf{Q} \end{bmatrix} < \mathbf{0}, \quad \forall\sigma = 1,2,3,4,
\tag{47}
$$

where $\mathbf{P}^{-1} = \mathbf{Q}$, *implying:*

$$
\mathbf{P}\mathbf{Q} = \mathbf{I}.
\tag{48}
$$

Proof. :

As shown in [55], the NCS (27) will be exponentially stable at transmission rate r, if (46) is satisfied and the discrete-time Lyapunov function satisfies the following inequality:

$$
\Delta V(k) = V(\mathbf{z}(k+1)\,) - V(\mathbf{z}(k)\,) < \left(\alpha_\sigma^{-2} - 1\right)V(\mathbf{z}(k)\,),
\tag{49}
$$

while considering the Lyapunov function $V(\mathbf{z}(k)\,) = \mathbf{z}^T(k)\mathbf{P}\mathbf{z}(k)$. In order to satisfy the H_∞ norm bound γ for the NCS (27), the following inequality has to be satisfied [83]:

$$
V(\mathbf{z}(k+1)\,) - V(\mathbf{z}(k)\,) + \widetilde{y}^T(k)\widetilde{y}(k) - \gamma^2\mathbf{\eta}^T(k)\mathbf{\eta}(k) < \mathbf{0}.
\tag{50}
$$

Here, $V(\mathbf{z}(k+1)\,)$ and $V(\mathbf{z}(k)\,)$ should satisfy the inequality condition for the exponential stability of the switched system. Substituting $V(\mathbf{z}(k)\,) = \mathbf{z}^T(k)\mathbf{P}\mathbf{z}(k)$ in (27), to satisfy the relation (49), we can write the following inequality:

$$\begin{bmatrix}\mathbf{z}^T(k) & \boldsymbol{\eta}^T(k)\end{bmatrix}\begin{bmatrix}\boldsymbol{\Phi}_\sigma^T\mathbf{P}\boldsymbol{\Phi}_\sigma-\alpha_\sigma^{-2}\mathbf{P} & \boldsymbol{\Phi}_\sigma^T\mathbf{P}\boldsymbol{\Gamma}_\sigma\\ \boldsymbol{\Gamma}_\sigma^T\mathbf{P}\boldsymbol{\Phi}_\sigma & \boldsymbol{\Gamma}_\sigma^T\mathbf{P}\boldsymbol{\Gamma}_\sigma\end{bmatrix}\begin{bmatrix}\mathbf{z}(k)\\ \boldsymbol{\eta}(k)\end{bmatrix}<\mathbf{0}. \tag{51}$$

For satisfying the H_∞ norm bound of the output to the disturbance input as per (50), the following inequality holds:

$$\widetilde{y}^T(k)\widetilde{y}(k)-\gamma^2\boldsymbol{\eta}^T(k)\boldsymbol{\eta}(k)\le\mathbf{0}. \tag{52}$$

Using the relation (44), in the above inequality yields:

$$\begin{bmatrix}\mathbf{z}^T(k) & \boldsymbol{\eta}^T(k)\end{bmatrix}\begin{bmatrix}\widetilde{\mathbf{C}}^T\widetilde{\mathbf{C}} & \mathbf{0}\\ \mathbf{0} & -\gamma^2\mathbf{I}\end{bmatrix}\begin{bmatrix}\mathbf{z}(k)\\ \boldsymbol{\eta}(k)\end{bmatrix}\le\mathbf{0}. \tag{53}$$

Considering the strict inequalities in (51) and (53), we can write:

$$\begin{bmatrix}\mathbf{z}^T(k) & \boldsymbol{\eta}^T(k)\end{bmatrix}\begin{bmatrix}\boldsymbol{\Phi}_\sigma^T\mathbf{P}\boldsymbol{\Phi}_\sigma-\alpha_\sigma^{-2}\mathbf{P}+\widetilde{\mathbf{C}}^T\widetilde{\mathbf{C}} & \boldsymbol{\Phi}_\sigma^T\mathbf{P}\boldsymbol{\Gamma}_\sigma\\ \boldsymbol{\Gamma}_\sigma^T\mathbf{P}\boldsymbol{\Phi}_\sigma & \boldsymbol{\Gamma}_\sigma^T\mathbf{P}\boldsymbol{\Gamma}_\sigma-\gamma^2\mathbf{I}\end{bmatrix}\begin{bmatrix}\mathbf{z}(k)\\ \boldsymbol{\eta}(k)\end{bmatrix}<\mathbf{0}, \tag{54}$$

which implies:

$$\begin{bmatrix}\boldsymbol{\Phi}_\sigma^T\mathbf{P}\boldsymbol{\Phi}_\sigma-\alpha_\sigma^{-2}\mathbf{P}+\widetilde{\mathbf{C}}^T\widetilde{\mathbf{C}} & \boldsymbol{\Phi}_\sigma^T\mathbf{P}\boldsymbol{\Gamma}_\sigma\\ \boldsymbol{\Gamma}_\sigma^T\mathbf{P}\boldsymbol{\Phi}_\sigma & \boldsymbol{\Gamma}_\sigma^T\mathbf{P}\boldsymbol{\Gamma}_\sigma-\gamma^2\mathbf{I}\end{bmatrix}<\mathbf{0}. \tag{55}$$

Thus, we can write (55) as:

$$\begin{bmatrix}-\alpha_\sigma^{-2}\mathbf{P}+\widetilde{\mathbf{C}}^T\widetilde{\mathbf{C}} & \mathbf{0}\\ \mathbf{0} & -\gamma^2\mathbf{I}\end{bmatrix}+\begin{bmatrix}\boldsymbol{\Phi}_\sigma^T\\ \boldsymbol{\Gamma}_\sigma^T\end{bmatrix}\mathbf{P}\begin{bmatrix}\boldsymbol{\Phi}_\sigma & \boldsymbol{\Gamma}_\sigma\end{bmatrix}<\mathbf{0}. \tag{56}$$

Taking Schur complement of (56), we can write:

$$\begin{bmatrix}\widetilde{\mathbf{C}}^T\widetilde{\mathbf{C}}-\alpha_\sigma^{-2}\mathbf{P} & \mathbf{0} & \boldsymbol{\Phi}_\sigma^T\\ \mathbf{0} & -\gamma^2\mathbf{I} & \boldsymbol{\Gamma}_\sigma^T\\ \boldsymbol{\Phi}_\sigma & \boldsymbol{\Gamma}_\sigma & -\mathbf{Q}\end{bmatrix}<\mathbf{0}, \tag{57}$$

where, $\mathbf{P}^{-1}=\mathbf{Q}$, thus proving (47) and (48). □ The error convergence due to the observed and current state depends on the boundedness of noise and disturbance vector stated for the linear switched system [81]. Hence, load disturbance and nature of FDI attack is considered to be pulsed. Pulsed load disturbance can be considered from the naval shipboard power system [84] or a fast DC voltage electric vehicle charger [85].

Load demand is a pulse signal defined as:

$$\Delta P_L=\begin{cases}0.01 & 10<t<100,\\ 0 & \text{otherwise.}\end{cases} \tag{58}$$

The disturbance is considered as an FDI attack in a similar pattern as given in [43] as:

$$d_{\text{FDI}}(t)=\begin{cases}0.04 & t>100\\ 0.09 & 120<t<150\\ 0 & t>150.\end{cases} \tag{59}$$

The FDI attack modifies the state variables like governor input $P_{g_i}(t)$ or the input signal to the EV, $P_E(t)$ as given in [43]. As far as the DR is concerned, the FDI attack modifies the state variable $x_1(t)$ which is indirectly affected by the attack on the data transfer between the load aggregator and the consumers.

The feasibility of the problem in Theorem 1 is nonconvex due to the matrix equality constraints as shown in (47) and (48). As shown in [86], this type of problem is NP-hard. The cone complementary linearization (CCL) algorithm efficiency is relatively higher as compared to other methods [87] while solving the LMIs with nonconvex constraints. This algorithm has also been used to find the state feedback controller for the NCS considering the network delay and packet dropout in [88]. The CCL algorithm states that the LMI $\begin{bmatrix}\mathbf{P} & \mathbf{I}\\ \mathbf{I} & \mathbf{Q}\end{bmatrix}\ge\mathbf{0}$ is feasible in the matrix variables $\mathbf{P}\in\mathbb{R}^n>\mathbf{0}$ and $\mathbf{Q}\in\mathbb{R}^n>\mathbf{0}$, then $\text{Tr}(\mathbf{PQ})\ge n$ and at the optimum $\text{Tr}(\mathbf{PQ})=n$ iff $\mathbf{PQ}=\mathbf{I}$. Hence, in order to find the controller and the observer gain for the switched system (27) using the CCL algorithm, the equality constraints (48) are cast in the following LMI form:

$$\begin{bmatrix}\mathbf{P} & \mathbf{I}\\ \mathbf{I} & \mathbf{Q}\end{bmatrix}\ge\mathbf{0}. \tag{60}$$

Hence, in order to find the observer and controller gain, the following trace minimization problem has to be solved:

$$min\,\text{Tr}(\mathbf{PQ}) \tag{61}$$

subjected to (46), (47) and (60).

The algorithm is summarized as follows:

Algorithm. : Cone Complementary Linearization (CCL).

Initialize: Select the number of iterations N and switching rate r and exponential convergence rate $\{\alpha_i\}_{i=1}^4$. Set $j=0$

if $\left(\sum_{i=1}^4 r_i log(\alpha_i)>0\right)$

Find $\{\mathbf{P_0},\mathbf{Q_0}\}$ solving (47) and (60)

for $j=0, N$ **do**

$\underset{\mathbf{P,Q}}{min}\text{Tr}\left(\mathbf{P}_j\mathbf{Q}+\mathbf{Q}_j\mathbf{P}\right)$ s.t. (47) and (60)

$\mathbf{P}_{j+1}\leftarrow\mathbf{P}$, $\mathbf{Q}_{j+1}\leftarrow\mathbf{Q}$

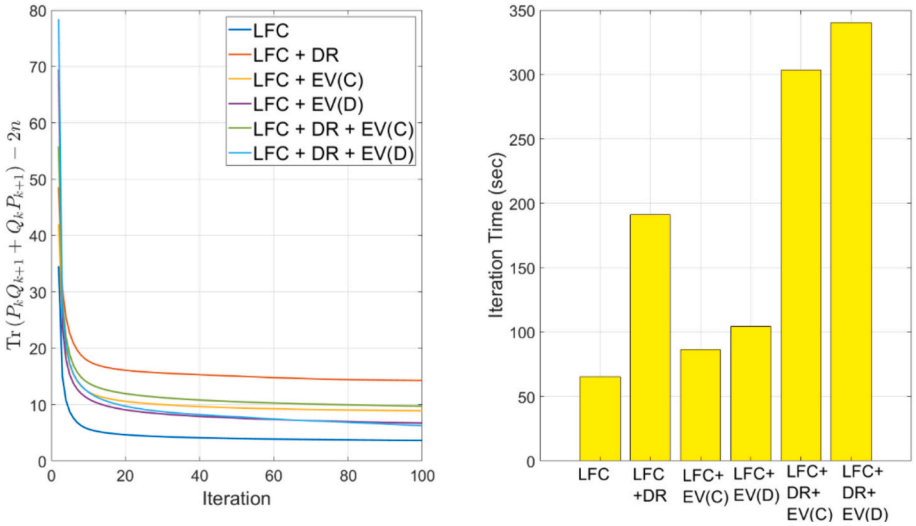

Fig. 3. Convergence of the CCL algorithm when it is run for 100 iterations and time taken for all the system configurations.

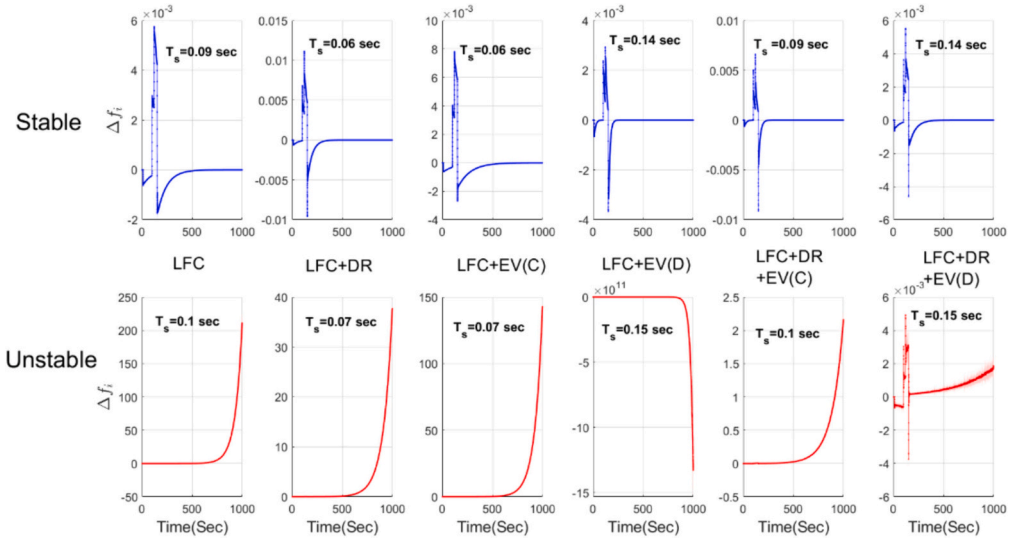

Fig. 4. Stable and unstable system response for different sampling time for different LFC system configurations.

end
end

5. Results and discussions

5.1. Convergence and computational time analysis

The joint observer and controller for the NCS are found numerically by solving the above CCL algorithm in MATLAB using the YALMIP toolbox [89]. The semidefinite optimization SeDuMi solver [90] is utilized in the YALMIP toolbox to implement the CCL algorithm, which solves (61), satisfying (46), (47) and (60). The solver can be initialized with the settings $\texttt{solver} = \texttt{'sedumi'}\ \texttt{sedumi.eps} = 10^{-12}$. The value of the data transmission rate (r) and exponential convergence rate, (α_i) as defined in, (46) is initialized as 0.1 and $\{1.50, 1.25, 1.25, 1.1\}$ respectively, which means the system is tuned at a 90 % packet drop rate. The activation of the packet drop condition is executed randomly. We employ a uniform random number generator to produce a random value within the range of 0 to 1, which is subsequently compared with our predetermined threshold of 0.9. If the generated value exceeds 0.9, data transmission occurs from both the feedforward and feedback paths. Otherwise, the control input $u(t)$ and output $y(t)$ retain their values from the previous time step, as outlined in eq. (26). The algorithmic convergence is tested on the LFC model with different DR, and EV configuration is shown in Fig. 3.

The algorithm converges to obtain $(\mathbf{P}, \mathbf{Q}, \mathbf{L}, \mathbf{K}, \gamma)$ in 100 iterations. We observe that the algorithm convergence rate is quite fast, as it requires

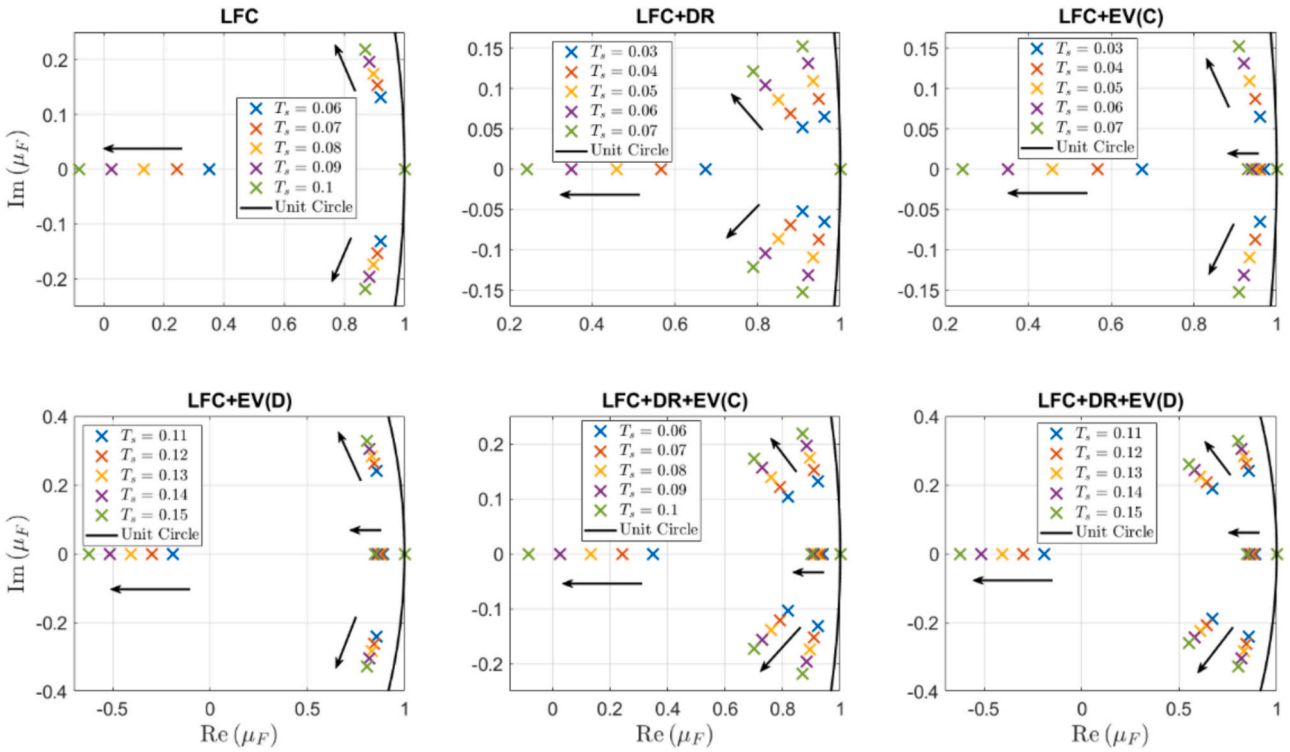

Fig. 5. Eigenvalue shifting of the discrete-time system sampled at different sampling intervals for different LFC system configurations.

around 20 iterations to settle down. The higher-order dynamics provided due to the DR time delay increases the total convergence time, as shown in Fig. 3. The total iteration time is highest for LFC, DR, and EV combined, as the system order is relatively high. Hence, we can say that the total iteration time depends linearly upon the order of the system. It is noted that the present work considers the CCL algorithm, a well-known technique for solving LMIs (57) with strict and nonconvex constraints, as a sequential optimization problem as reported in [59,67,87,91]. As shown in Fig. 3, the CCL algorithm ensures the convergence of the error $\mathrm{Tr}(\mathbf{P}_k\mathbf{Q}_{k+1} + \mathbf{Q}_k\mathbf{P}_{k+1}) - 2n$ for all the system configurations, i.e. at a minimum value when $t \to \infty$ while satisfying the LMIs (57). However, we observe an unequal converged CCL error in Fig. 3, which can be attributed to the difference in system configuration.

5.2. System stability based on the sampling time

The system response of the different system configurations with the proposed state feedback controller and observer for different sampling time T_s is shown in Fig. 4. We observe a spike in the frequency response at a time interval $10 < t < 200$, which is due to the bounded load disturbance and the FDI attack as mentioned in (58) and (59). The maximum frequency fluctuations are encountered with LFC with DR configuration, being marginally >0.01 p.u. (per-unit). The maximum frequency fluctuations $\{\Delta f_i\}_{\max}$ are comparable to the one obtained in [37]. Moreover, it is also in line with the IEEE smart grid industrial standards of interoperability [92].

The sampling time T_s is varied at the rate of 0.01 s to find the discretized system as per the relation given in (23), from which the LMI is solved to obtain the controller and observer gains. A low value of T_s utilizes that higher communication bandwidth, while a higher value can make the plant unstable with the obtained observer and controller gains. Hence, a threshold margin of the sampling time is obtained, beyond which, if increased, can make the LFC system unstable, as shown in Fig. 4. We found the threshold on T_s from the simulations but a more rigorous analysis on the choice of sampling time can be explored in the future using analytical methods. As per our analysis, the sampling time T_s for instability is least when LFC and EV/DR is utilized and highest for LFC with decentralized EV configuration with and without the inclusion of DR. The system response in Fig. 4 suggests that the LFC with DR and decentralized EV configuration utilizes minimum communication bandwidth for stability scenario while ensuring system stability.

The integration of EVs into LFC follows the configuration outlined in [33]. Despite appearing as an additional transfer function in Fig. 1, it is utilized in two distinct configurations as presented in eq. (17). However, the impact can be summarized as follows:

- In the decentralized EV configuration, the sampling time required for controller design is observed to be the largest, as shown in Fig. 4. Higher sampling time subsequently reduces the communication bandwidth, necessary for implementing the control scheme.
- Notably, the decentralized EV configuration exhibits the lowest maximum frequency fluctuation during FDI attacks. This suggests that when EVs are integrated into the LFC loop as decentralized energy sources, they enhance system stabilization in the presence of FDI attacks and packet drop rates.

The above inference is supported in Fig. 5, with the given eigenvalue pattern of $\mathbf{F}$ at different sampling times for different LFC, DR and EV configurations. LFC has an eigenvalue at the origin, a real eigenvalue and a pair of complex eigenvalue pairs. The eigenvalue at the origin is responsible for making the steady-state value of Δf_i to zero. DR state variable adds another pair of complex eigenvalue pair, while a coupled EV configuration adds another eigenvalue on the real axis while pulling the resultant complex eigenvalue pair closer to the origin. With the decentralized EV configuration, the eigenvalue located on the real axis is not affected. However, the complex pairs of eigenvalues move away

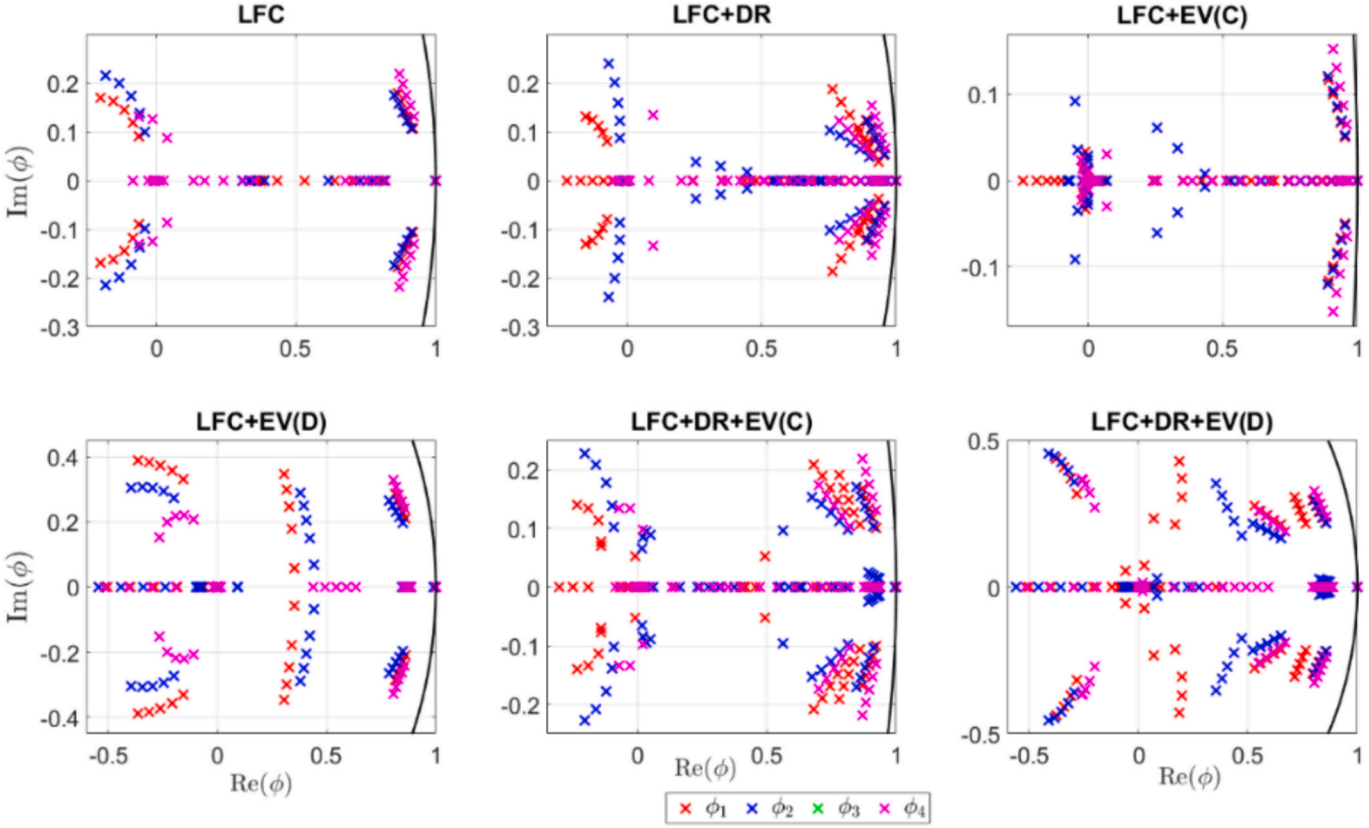

Fig. 6. Eigenvalue configuration of the modelled switched systems at different sampling times for different system configurations.

from the origin, resulting in stability at a higher sampling rate and faster system performance in terms of settling time. A similar phenomenon is observed in LFC and DR with different EV combinations, centralized and decentralized, where the complex and real poles are farther away from the origin. Controller designed on the LFC system where eigenvalues are far away from the origin gives faster response with a smaller peak overshoot.

The degradation in stability for all systems under varying sampling time is observed in Fig. 5. It is seen that the eigenvalues of all the systems are shifting towards higher frequencies and lower damping region, i.e. shifted away from the stable region when T_s is increasing. Moreover, when DR is considered in the LFC and the combination of LFC and EV, the number of complex conjugate poles increases (i.e. two pairs of complex conjugate poles); thus, the number of non-dominant poles are increasing. Therefore, it will be challenging to design a controller based on dominant pole placement for these systems [93,94]. However, a deeper insight into system characteristics is obtained by incorporating the controller and observer gains to consider the eigenvalues of $\{\Phi_i\}_{i=1}^{4}$ for all the system configurations, as shown in Fig. 6. We observe that the eigenvalues or poles of each sub-system lie within the unit circle at different sampling times. However, the poles are shifting towards higher frequencies and lower damping ratio region in the unit circle with an increase in sampling time T_s.

When packet drop occurs in both feedback and forward path, i.e. Φ_4, we observe that the poles are more divergent in nature with higher T_s than other sub-systems for all system configurations. In the case of LFC with DR and both DR and EV configuration, the eigenvalues of sub-systems under no packet drop are dominant with an increase in T_s. However, for the LFC with EV with centralized configuration Φ_4 provides poles with dominant nature with an increase in T_s. The switched systems can be unstable or stable under certain switching signals between all the sub-systems, even though the sub-systems are stable, unstable or a combination of both respectively [79,95,96]. This phenomenon can be attributed to the fact that the system stability depends on the dynamics of each sub-system and the properties of the switching signal (e.g. controlled switching, arbitrary switching). The switched system stability under controlled or restricted switching using dwell-time and average dwell-time [97], piecewise and multiple Lyapunov function [79] approaches have also been discussed. For example, Hespanha [98] has proposed that under the time-controlled class of switching signals (i.e., trajectory independent), uniform asymptotic stability of switched linear systems is equivalent to the exponential stability, and in [97], it has been shown that under slow switching, the switched-system is exponentially stable. For ensuring the stability of the switched systems with both stable and unstable sub-systems, an average dwell time approach has been proposed in [99], where the activation time of unstable sub-systems is chosen smaller than the stable sub-systems. However, the approaches proposed in [97,99] are not valid for switched systems under arbitrary switching since these methods suggest dwelling in stable sub-systems for a considerable period. The existence of CQLF using the LMI approach has been presented for the switched systems under arbitrary switching in [56,58,59,67,68,96]. In the present work, NCS under packet drop has been modelled as switched systems using the ADS approach, where the aim is to obtain observer and state feedback controller gains with CQLF and bounded H_∞ norm such that the LMIs (47) are satisfied, ensuring exponential stability for the NCS, subjected to packet drop modelled as switched systems under arbitrary switching. Therefore, it is important to select appropriate T_s for the discrete time dynamical systems such that the NCS is exponentially stable, since the sub-systems are going towards instability region with the increasing T_s; thus leading to an unstable behavior of the NCS (27) under arbitrary switching. Hence, we can infer that the selection of T_s should be smaller for the stable sub-systems to achieve overall stability of the NCS, modelled as switched systems under arbitrary switching. The

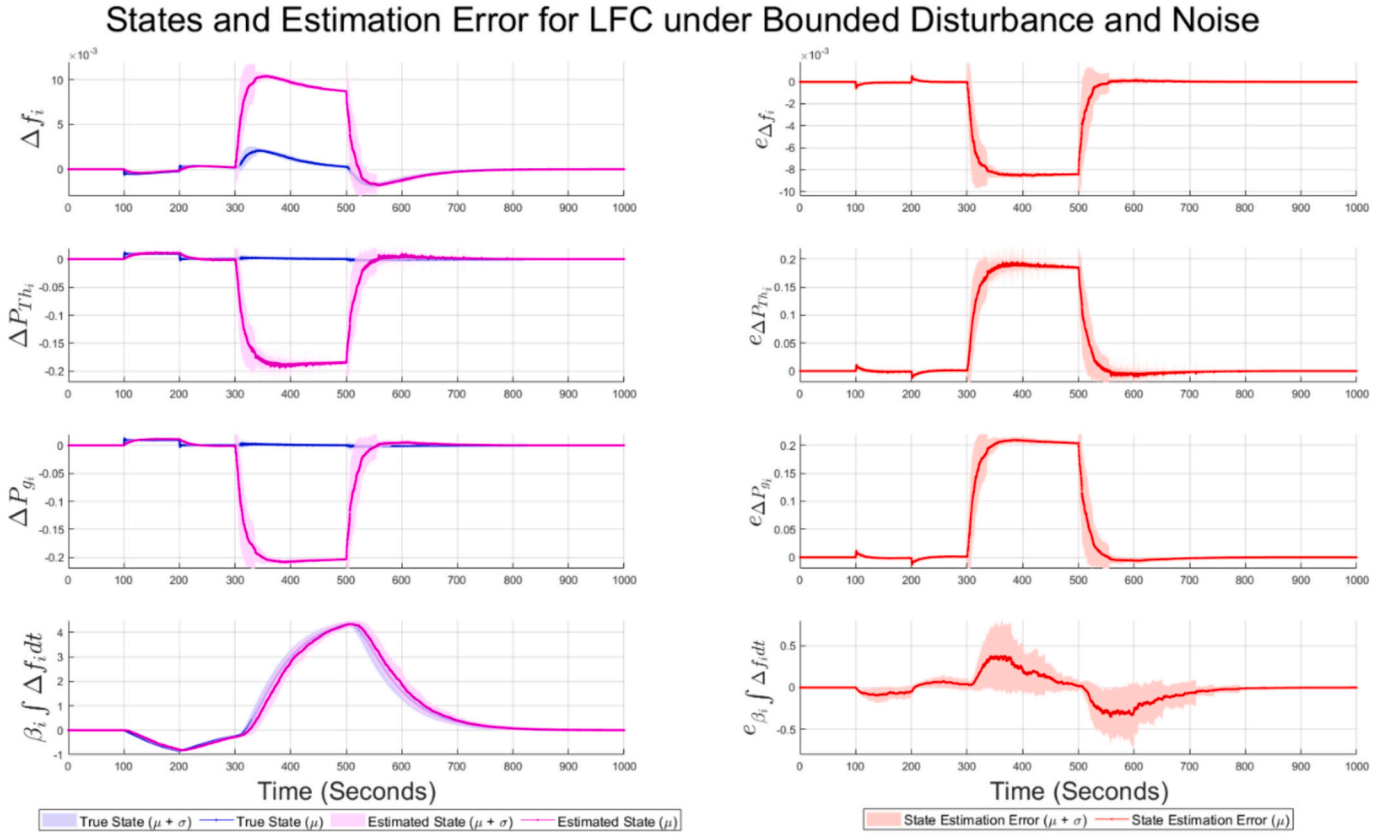

Fig. 7. True/observed states and estimation error for the LFC under bounded disturbance and noise obtained after 100 Monte Carlo simulations at 99% random packet drop rate.

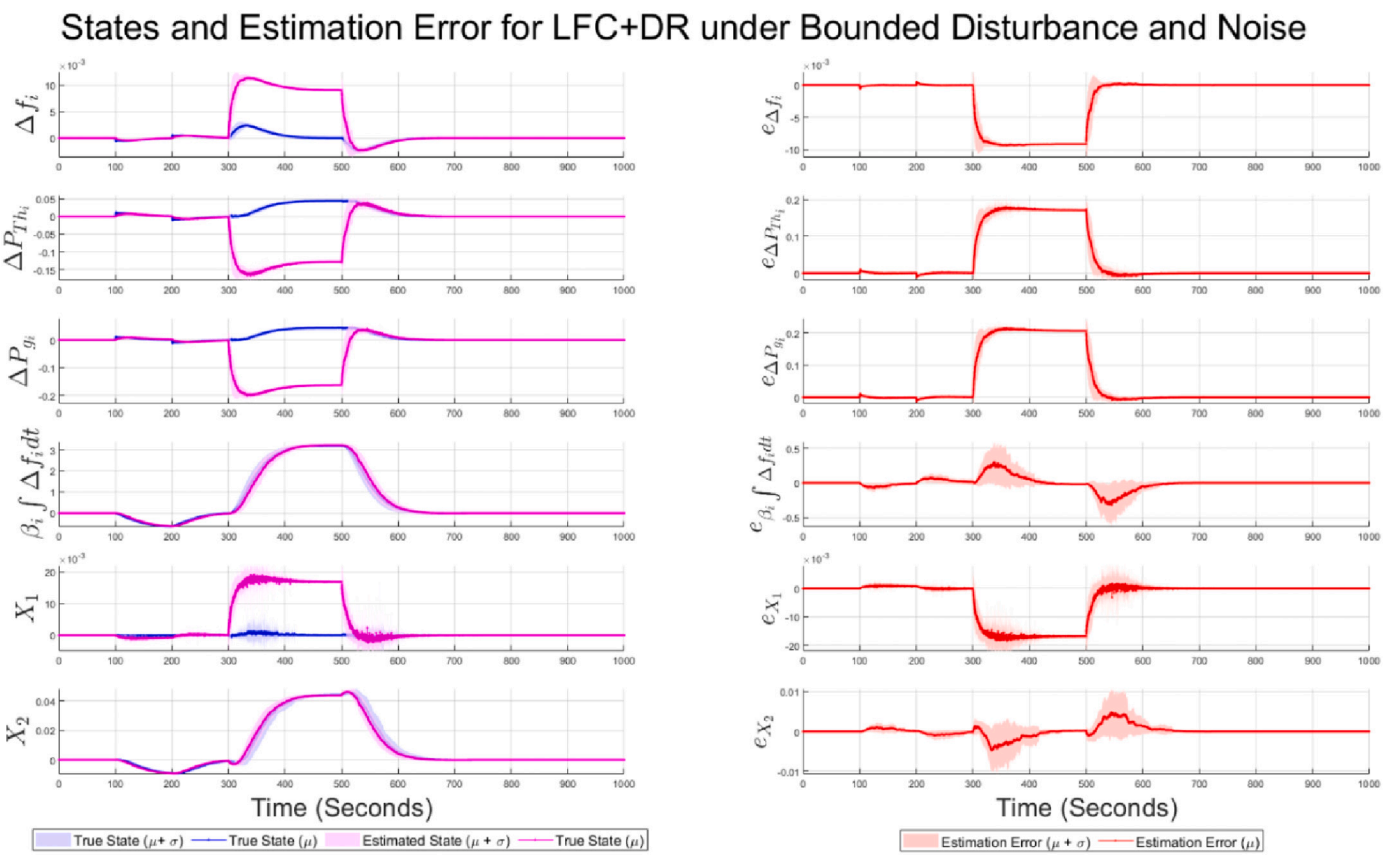

Fig. 8. True/observed states and estimation error for LFC with DR under bounded noise and disturbance obtained after 100 Monte Carlo system simulations at 99% random packet drop rate.

selection of T_s for the NCS stability analysis under arbitrary packet drop will be analytically explored in the future. Although in many contemporary studies on NCS based on random and fixed delays, researchers have considered the Lyapunov-Krasovskii functional (LKF) for stability analysis which is fundamentally different from the approach reported in this paper. Here, the focus is to consider Pade approximation of the fixed delay within a switched system framework, needed to model the packet drops in the NCS.

With high packet drop rates in feedback and forward path, we can expect the switched system Φ_4 to be activated most of the time. Hence the poles of Φ_4 will dominate the dynamics of the overall system. As we saw in Fig. 5, we also see a similar pattern for eigenvalues of $\{\Phi_i\}_{i=1}^{4}$ in Fig. 6, where they move away from the origin with an increase in sampling time. In a decentralized EV system with LFC, the eigenvalue movement is away from the real and imaginary axis. However, for LFC systems with DR, the eigenvalues drift away along the imaginary axis only. We observe in the case of decentralized EV systems with LFC, the complex conjugate eigenvalue pairs are further apart, from the origin, as compared to the eigenvalues in other system configurations. As a result, we see a better-quality response from the networked system.

5.3. State estimation and analysis under bounded noise and disturbance

The system response with the designed state feedback controller and observer gain obtained after solving the LMI (57) using the CCL algorithm is shown in Fig. 7, Fig. 8, Fig. 9, Fig. 10, Fig. 11 and Fig. 12. The system response is obtained under bounded noise and disturbance, which is defined as follows:

$$\Delta P_L = \begin{cases} 0.01 & 100 < t < 200 \\ 0 & \text{otherwise}, \end{cases} \tag{62}$$

and

$$n(t) = \begin{cases} 0.01 & 300 < t < 400 \\ 0 & \text{otherwise}. \end{cases} \tag{63}$$

The FDI attack as a disturbance is not considered in this case since it was studied in the previous section. Pulsed load disturbance is considered for the simulation analysis. The noise represents the error in measuring variables in the power control centre and EV aggregator centre for those configurations where EV was deployed. The nature of the disturbance in (62)–(63) is such that it is L_2-norm bounded so that the controller and observer design is valid for linear switched system [81]. The system simulation is performed at a 99 % packet drop rate, even though the controller and observer gains were obtained at a 90 % packet drop rate. The simulation strategy was deployed to analyse the state estimation error and system sensitivity to higher packet drop rates and controller validation. The sampling time T_s considered here is the one described in the previous section.

We observe a common trend for all the system configuration that the estimation error due to disturbance input is higher than the input load disturbance. Moreover, we also observe that the settling time and uncertainty of the estimated system state, when the bounded noise was applied, is relatively higher than the settling time when the disturbance was applied. We observe for the states $\{\Delta f_i, \Delta P_{Th_i}, \Delta P_{g_i}\}$, the settling time for the estimation error is close to 200 s and for $\beta_i \int \Delta f_i dt$ it is around 400 s even though the noise duration was for 100 s as defined in (63). However, we observe that the settling time for the state $\beta_i \int \Delta f_i dt$ is the highest for the LFC system in Fig. 7 as compared to other states. The settling time is lower when the input disturbance ΔP_L is applied. Hence, we observe a steep jump in $\beta_i \int \Delta f_i dt$ value when the noise is applied. The finite uncertainty in the estimation error plot $e_{\beta_i \int \Delta f_i dt}$ during the time

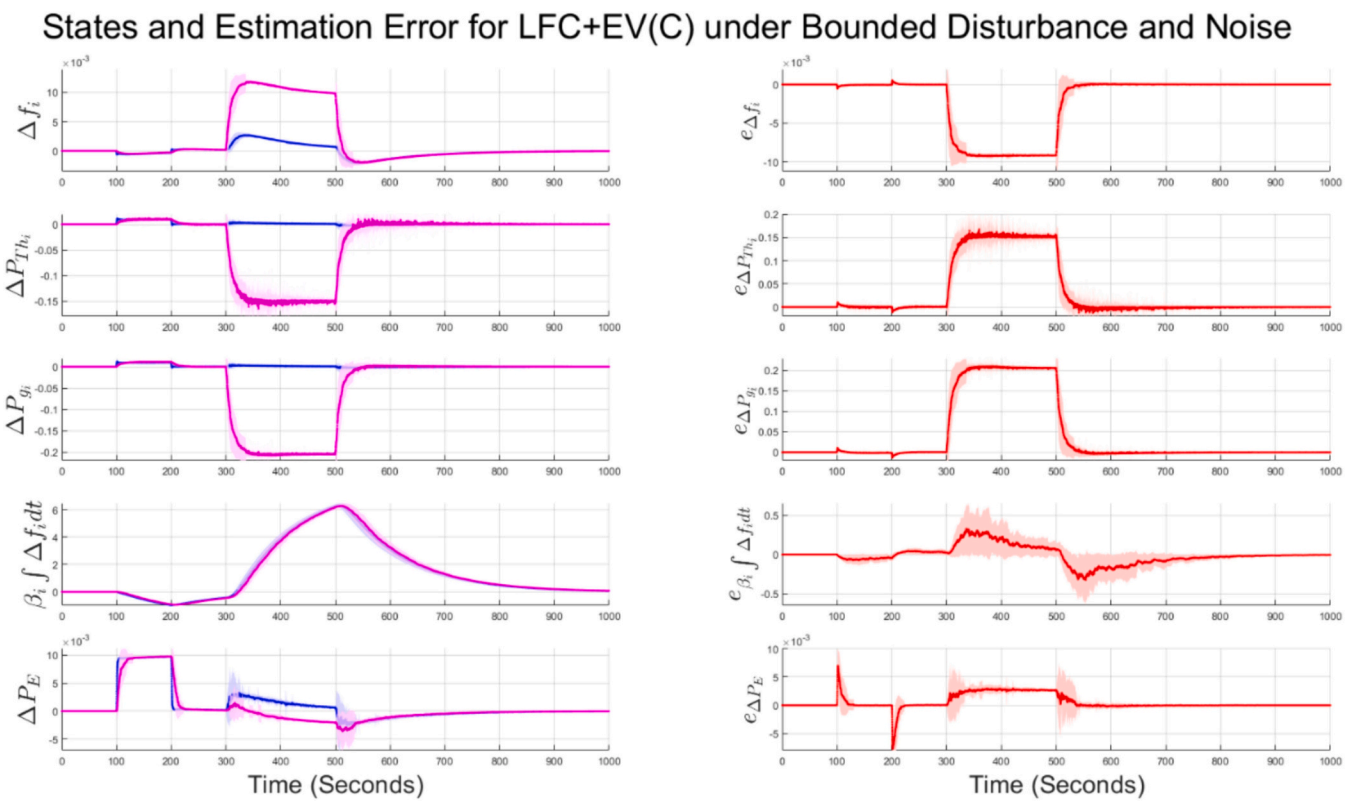

Fig. 9. True/observed states for LFC with centralized EV configuration under bounded noise and disturbance obtained after 100 Monte Carlo simulations at 99% random packet drop rate.

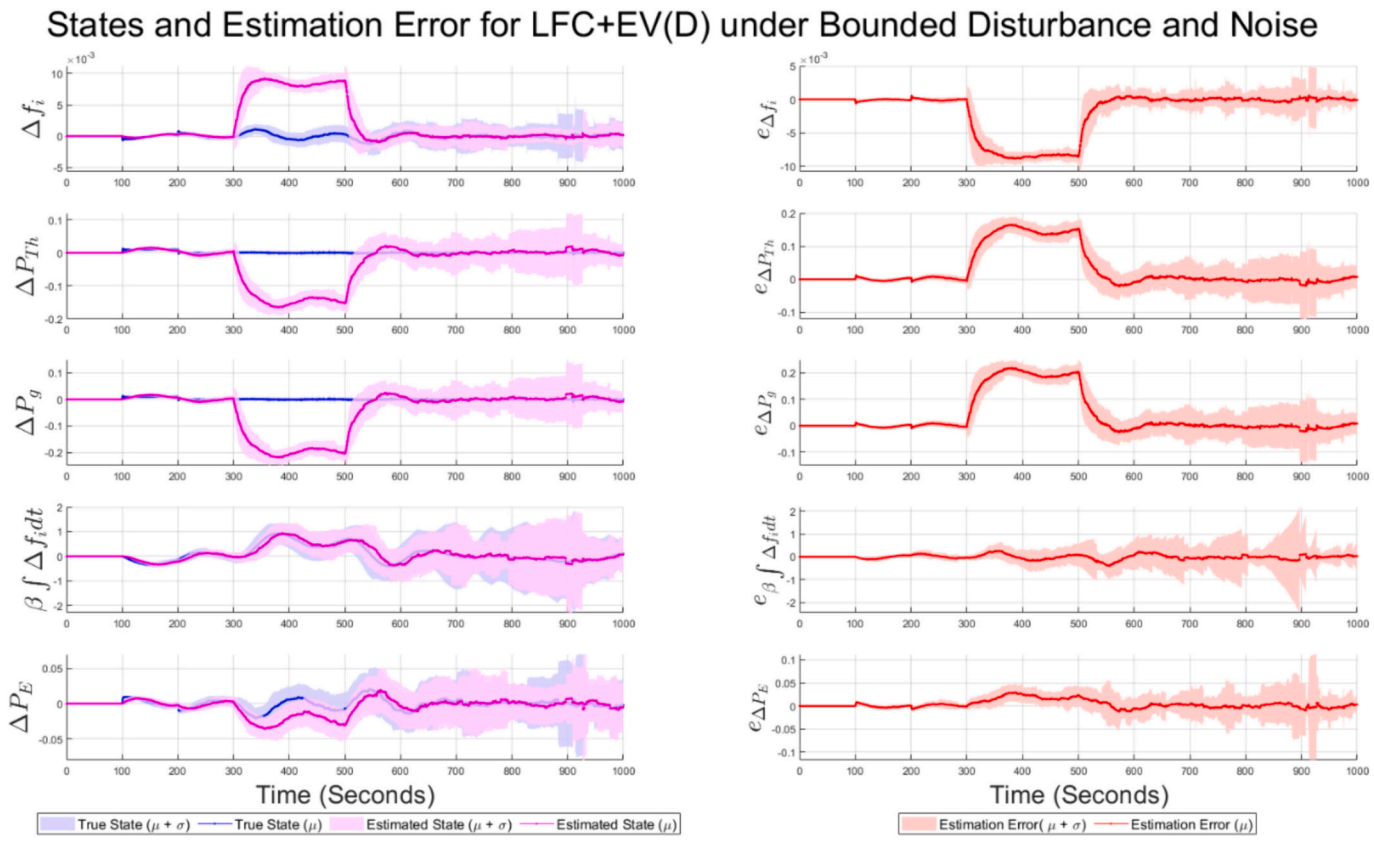

Fig. 10. True/observed states for LFC with decentralized EV configuration under bounded noise and disturbance obtained after 100 Monte Carlo simulations at 99% random packet drop rate.

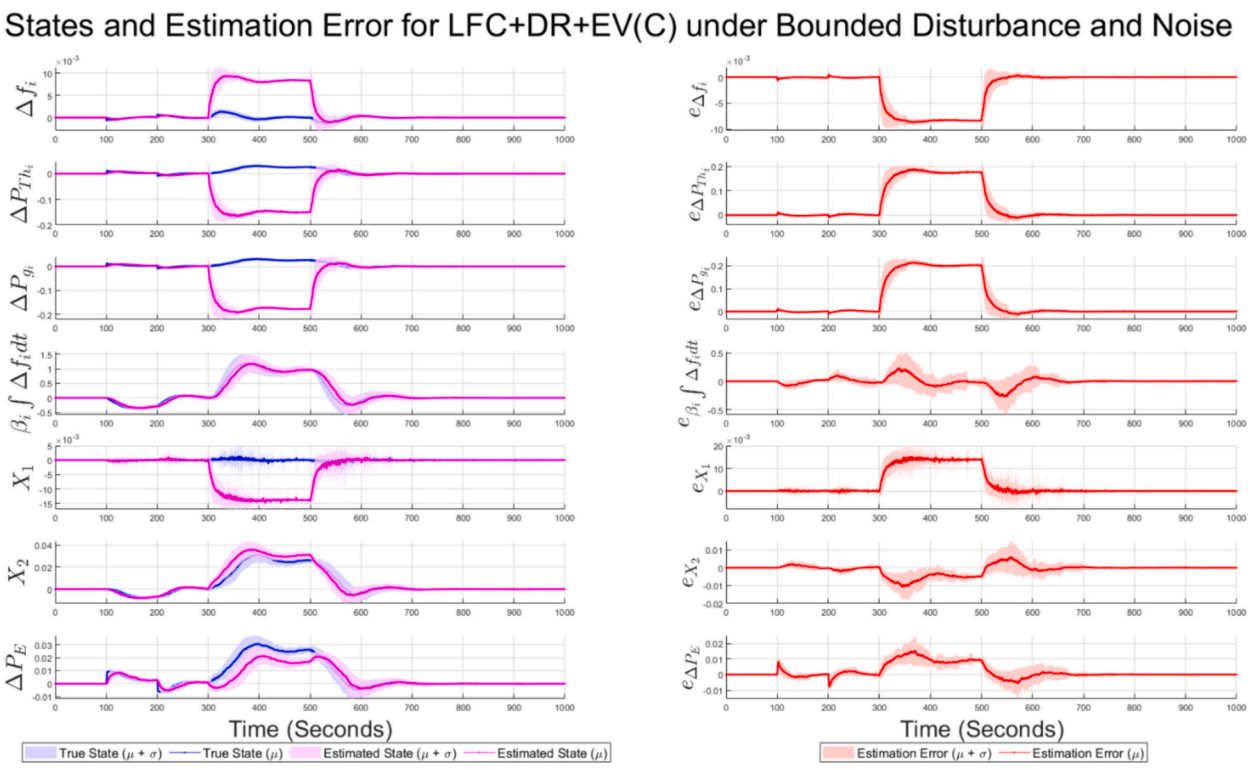

Fig. 11. True and observed states for LFC with demand response and centralized EV configuration obtained after 100 Monte Carlo simulations at 99% packet drop rate.

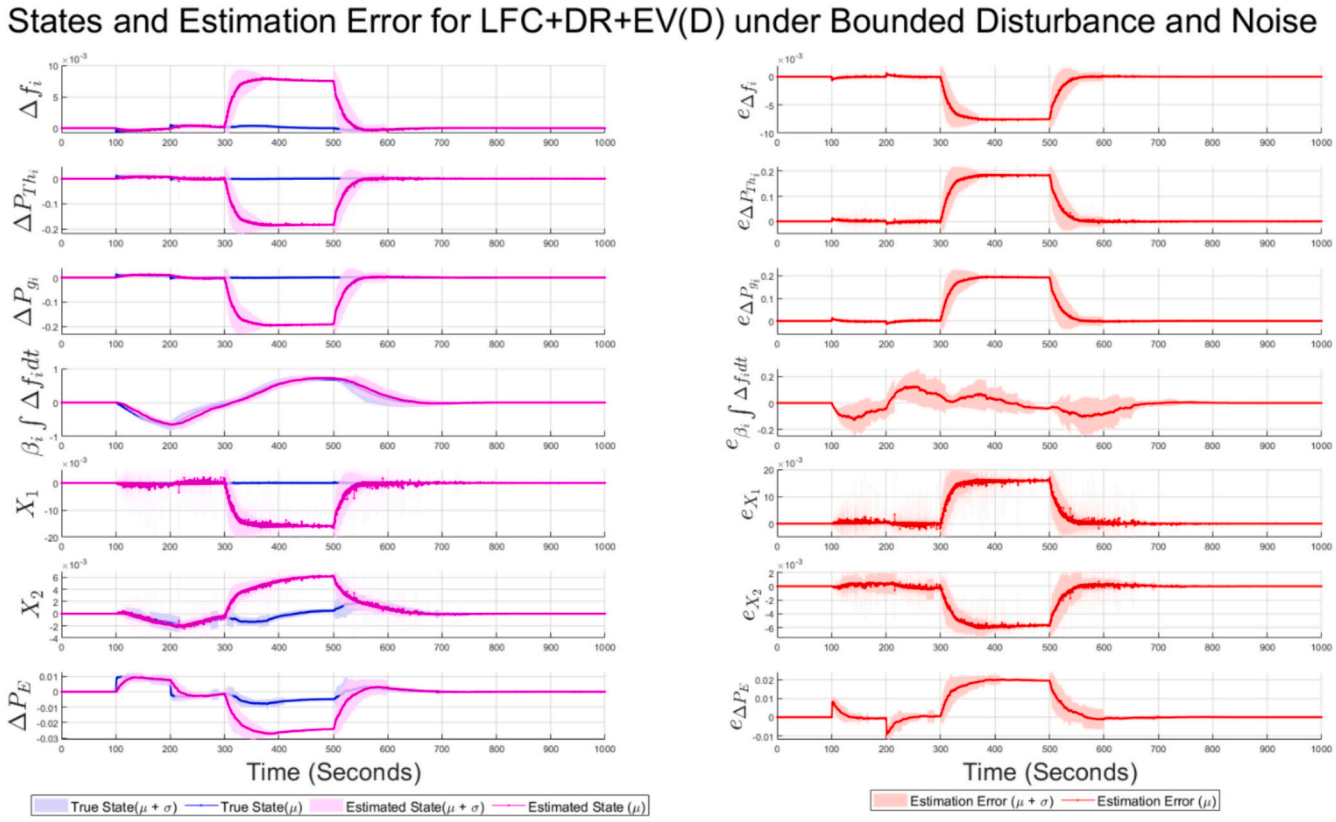

Fig. 12. True and observed states for LFC with demand response and decentralized EV configuration obtained after 100 Monte Carlo simulations at 99% packet drop rate.

$200 < t < 300$, even when no disturbance or noise is present in the system, confirms that the state was not steady during that period. Physically, the secondary control feedback for frequency deviation and its observer estimated value is quite sensitive to system noise. We observe higher uncertainty in the state estimation error for the remaining states when it is settling down or reaching the peak under persistent noise in the given time duration.

We observe in Fig. 8 that the response of the states $\{\Delta f_i, \Delta P_{Th_i}, \Delta P_{g_i}\}$ and estimation error is similar to what we observed for the LFC system with a similar settling time. However, the settling time for the state estimation error $\beta_i \int \Delta f_i dt$ is much lower than the previous case. Moreover, the settling time for that state for input disturbance is also lower, which can be attributed to the demand response contribution, where the requirement of secondary control input becomes lesser than the same without it. However, we observe uncertainty in the error response of the state $\beta_i \int \Delta f_i dt$ at the time $500 < t < 600$, even though no disturbance or noise is present during that interval. This phenomenon is attributed due to the delay between the aggregator and consumer response which also reflects on the estimation error of the state $\{X_1, X_2\}$ and $\beta_i \int \Delta f_i dt$ during the interval $500 < t < 600$.

We observe in Fig. 9 that the estimation error of the states $\{\Delta f_i, \Delta P_{Th_i}, \Delta P_{g_i}\}$ is quite similar as compared to the previous cases for the LFC with centralized EV configuration. However, we observe the uncertainty in the estimated value of the state ΔP_{Th_i} during the time interval $300 < t < 500$. The settling time for $\beta_i \int \Delta f_i dt$ is higher for the LFC system, which we observed in Fig. 7 due to the uncertainty of its estimation error. Unlike the other states, the effect of load disturbance is higher for the state ΔP_E than the measurement noise, which is evident by comparing its peak. However, the settling time of the state ΔP_E is much faster as compared to other system states.

As compared to the previous responses, the state estimation error is not settling down to zero, as shown in Fig. 10 for the LFC system with a decentralized EV configuration. However, the mean of the estimation error is almost settling to zero for all the states. Higher uncertainty is caused for this system due to the fact that the poles are far apart from the origin, as shown in the eigenvalue plot for the discretized system in Fig. 5. An increase in any parameter moves the eigenvalues of the closed-loop system closer to the unit circle, making the system sensitive to parametric variations. We observe that the oscillations due to measurement noise are much higher, as compared to system disturbances. However, the peak of the state $\beta_i \int \Delta f_i dt$ is much lower as compared to the previous cases.

For the LFC, demand response, and EV configuration, the estimation error is similar for centralized and decentralized configuration. However, for $\beta_i \int \Delta f_i dt$, the peak value is lower for the decentralized configuration. In the centralized EV configuration, $\beta_i \int \Delta f_i dt$ settles faster when there is an input disturbance, but the settling time is similar for the same state under a bounded noise scenario. We observe a higher uncertainty for the estimation error of $\beta_i \int \Delta f_i dt$ in the decentralized scenario, which may be due to the higher system sensitivity to parametric variations. We observe the sensitivity in the wiggles found for the mean state of $\{X_1, X_2\}$ for the decentralized EV scenario. The wiggles are also persistent when the noise and disturbance are not present in the system. However, we do not see any uncertainty or wiggles for $\{X_1, X_2\}$ during the input disturbance period for the centralized EV configuration. However, the trend is opposite for the state ΔP_E, where we find higher uncertainty for the system with centralized EV configuration when the bounded noise is present in the system. Moreover, we also observe an improvement in the settling time for the state ΔP_E for the decentralized EV configuration. However, the system response and estimation error are similar for ΔP_E during the interval when input disturbance is applied to the system.

5.4. State estimation and analysis under FDI attack and load disturbance

In Fig. 13, we observe that all the states are estimated perfectly by the observer, tracking in the given time interval. However, during the period when the FDI attack and load disturbance occurs, the real and the observed states vary. We observe that the state $\beta \int \Delta f_i dt$ is estimated perfectly despite the FDI attack and load disturbance, which may be due to the relative magnitude of the attack and the estimated states being higher than the remaining states. When the FDI attack and load

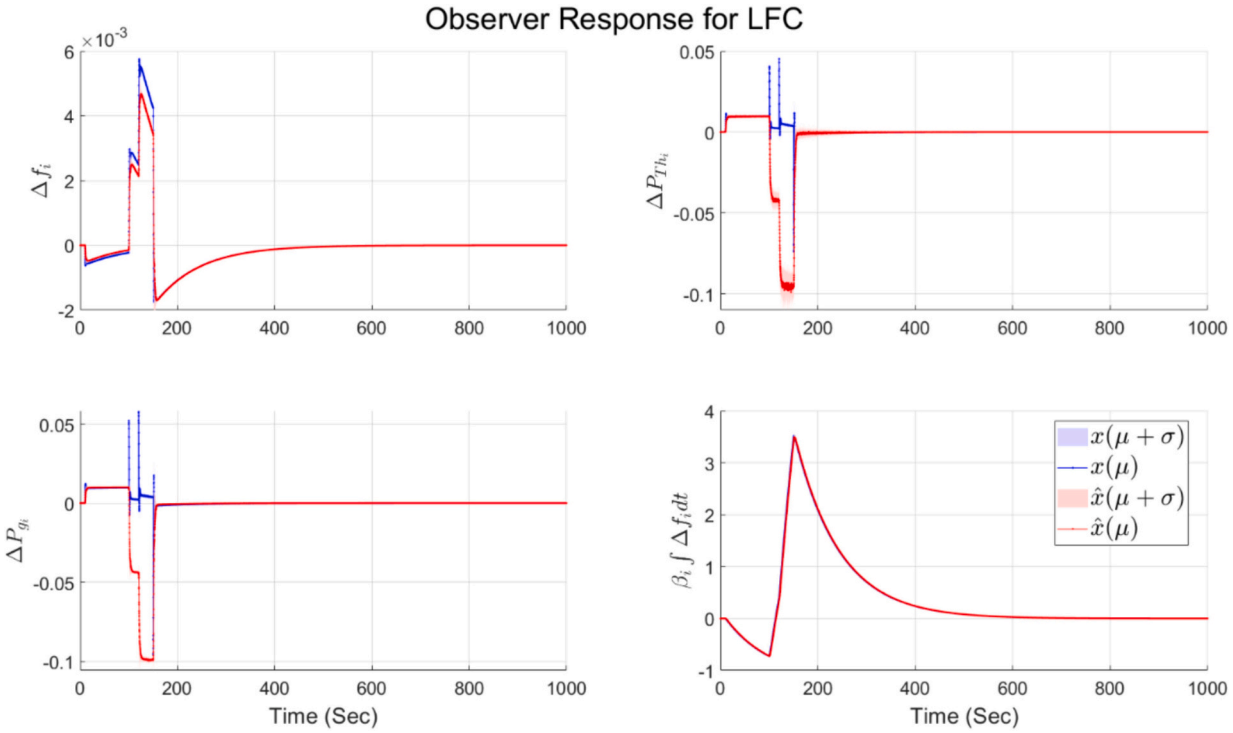

Fig. 13. Observer response for LFC system with mean and uncertainty calculated over 100 Monte Carlo simulations.

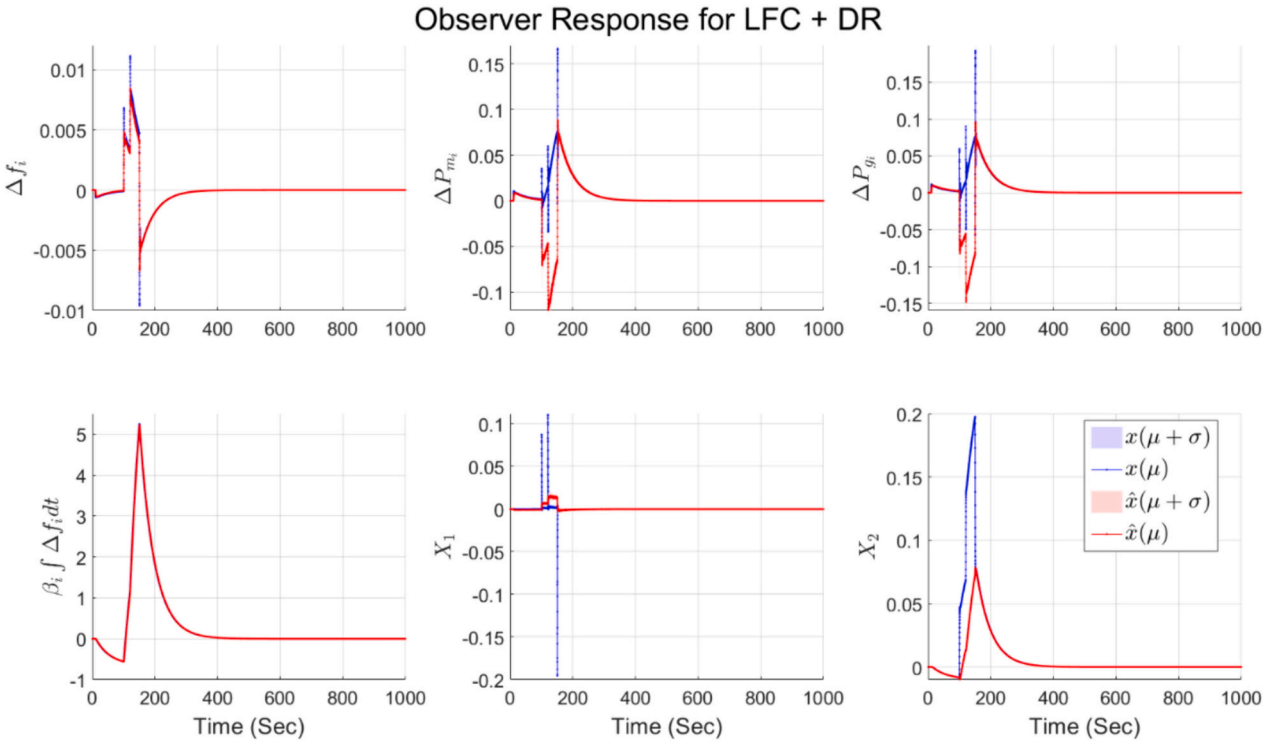

Fig. 14. Observer response for LFC and DR system configuration with mean and uncertainty calculated over 100 Monte Carlo simulations.

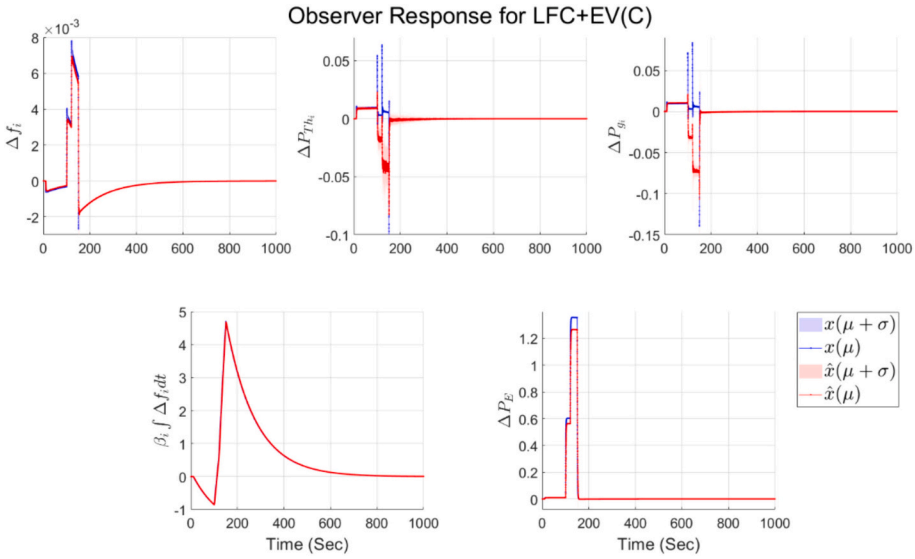

Fig. 15. Observer response for LFC and centralized EV system configuration with mean and uncertainty calculated over 100 Monte Carlo simulations.

disturbance occurs, $\{\Delta P_{g_i}, \Delta P_{m_i}\}$ increases for a while before it settles down to zero. It suggests that FDI attack on the input tends to increase the generation than what is required from the plants.

The impact of the FDI attack on $\{\Delta P_{g_i}, \Delta P_{m_i}\}$ is much more pronounced for LFC and DR, as seen in Fig. 14, as the peak value is higher than observed in the previous case. However, the estimated states $\{\Delta \widehat{P}_{g_i}, \Delta \widehat{P}_{m_i}\}$ during FDI attack is negative maximum of the original state variables observed. For the DR state variables $\{X_1, X_2\}$, we also observe a similar pattern, where estimation error is large when the FDI attack occurs with the underestimation of both the parameters.

When we incorporate a centralized EV configuration with LFC, positive power output from the aggregator is expected as shown in Fig. 15, which means either the EVs have to be in discharge mode during that period or energy has to be provided from the storage devices owned by the aggregators. However, the peaks of $\{\Delta P_{g_i}, \Delta P_{m_i}\}$ during load disturbance and FDI attack are much lower than in the previous case suggesting that the centralized EV provides better regulation of power plants during the grid disturbance as compared to DR. The EV state ΔP_E is almost correctly estimated even during the FDI attack.

However, when EV is introduced in a decentralized configuration in the LFC loop, ΔP_{Th_i} is better estimated by the observer, as shown in Fig. 16. Moreover, the peak of $\{\Delta P_{g_i}, \Delta P_{m_i}\}$ during load disturbance and FDI attack is much lower as compared to all the previous cases. We also observe a reduced ΔP_E requirement in the decentralized strategy as

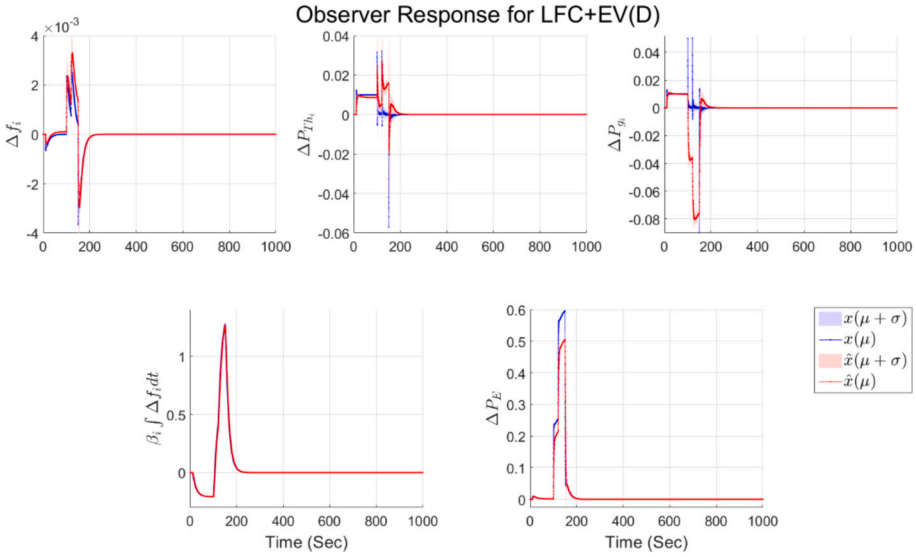

Fig. 16. Observer response for LFC and decentralized EV system configuration with mean and uncertainty calculated over 100 Monte Carlo simulations.

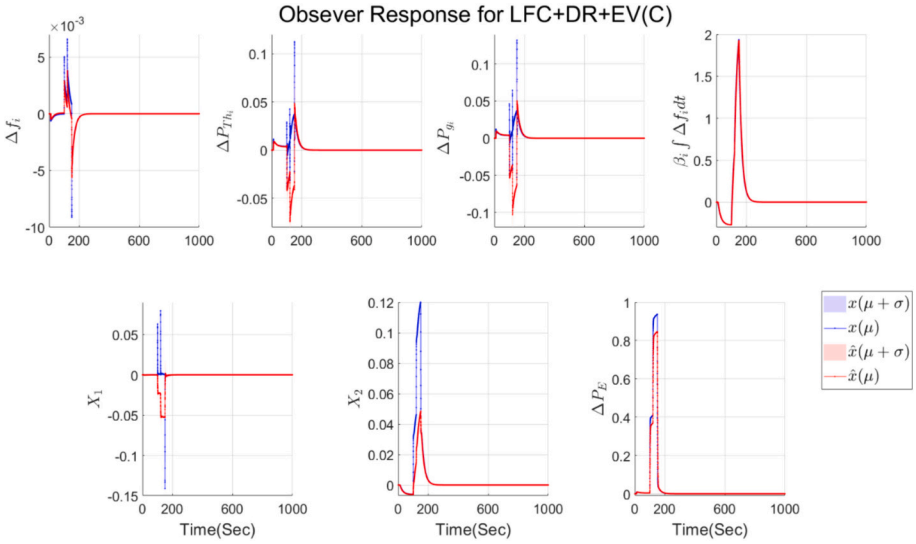

Fig. 17. Observer response for LFC, DR and centralized EV system configuration with mean and uncertainty calculated over 100 Monte Carlo simulations.

compared to the centralized strategy of the EV, which is mainly due to the introduction of the eigenvalues away from the origin. There is also a reduction of $\beta \int \Delta f_i dt$ required to stabilize the frequency of the grid.

When all the LFC, DR and EV configuration is combined, we observe a higher peak for the state $\{\Delta P_{g_i}, \Delta P_{m_i}\}$. However, the secondary frequency feedback $\beta \int \Delta f_i dt$ required is much lower during the disturbance. Similarly, we observe lower ΔP_E requirement from the aggregator when the EV works in a decentralized configuration compared to the centralized one (Figs. 17 and 18). The estimation of the EV power is much better than the other state variables, during the FDI attack and load disturbance.

5.5. System response with different packet drop rate

As we increase the packet drop rate from 90 to 95%, we observe a marginal difference in the frequency fluctuation response shown in Fig. 19. However, as we increase it to 99%, most system configurations remain stable except when EV is utilized in a decentralized fashion in conjunction with the classical LFC. We observe sustained oscillations in that case, which seems to increase with time along with higher uncertainty. The higher oscillations suggest that the system is fragile with high sensitivity to the system parameters like packet drop rates. We also observe a higher uncertainty in the frequency fluctuation due to random packet drop rates for LFC, DR and EV configurations. When the packet-drop rates increase to 99.9%, the LFC with decentralized EV configuration becomes unstable with or without the inclusion of demand response. However, when the EV configuration is centralized, we observe sustained oscillations of lower magnitude than LFC and LFC with DR configurations. The oscillations with LFC and LFC with DR have higher uncertainty and seem to grow bigger with time (Fig. 19).

5.6. System response with various demand response time delays

As seen in Fig. 20, the system configuration of demand response with LFC and LFC with centralized EV configuration is stable with an increase in demand response time delay. However, the system is unstable when decentralized EV configuration is used with the increase in time delay. In Fig. 5 and Fig. 6, we observe that the eigenvalues move away from the stability region in the decentralized EV operation. The eigenvalues tend

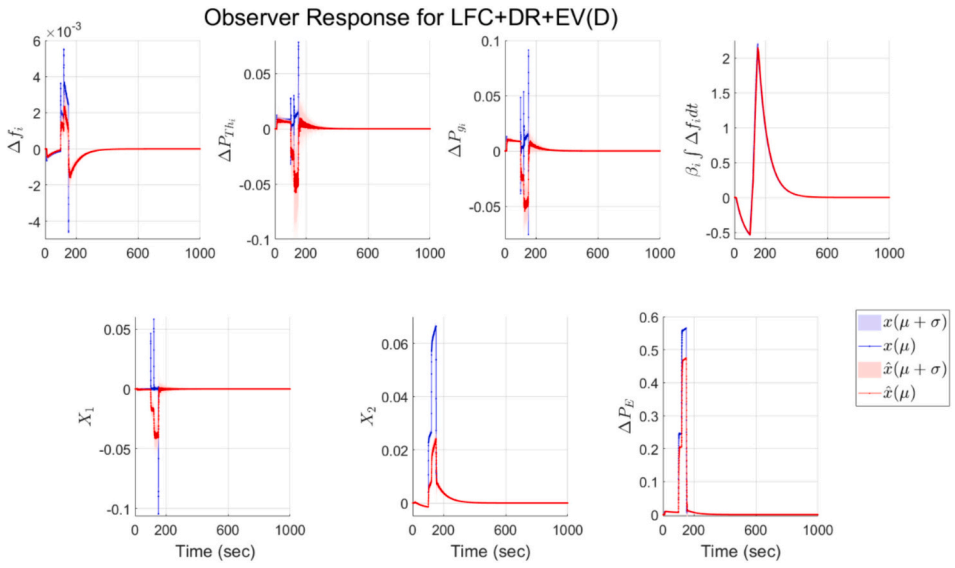

Fig. 18. Observer response for LFC, DR and decentralized EV system configuration with mean and uncertainty calculated over 100 Monte Carlo simulations.

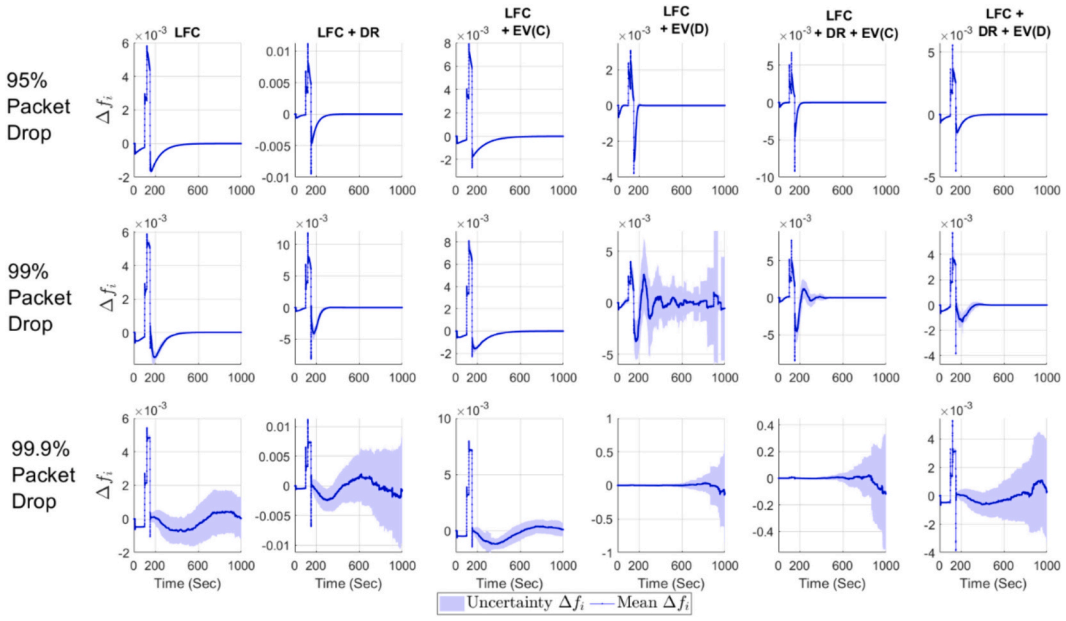

Fig. 19. Frequency fluctuations for different system configurations with variation in the packet drop rates calculated for all LFC system configuration over 100 Monte Carlo simulations.

to make the system fragile and sensitive to system parameters like the DR time delay. We also observe from Fig. 21 that as the time delay T_d of the demand response increases, the eigenvalues move towards the unit circle. Hence, due to switching behavior, these eigenvalues move out from the stability region to render the system unstable.

5.7. System response and multivariate analysis including renewable energy sources

As shown in Fig. 22, stochastic solar power output is passed through a DC-DC converter and an interconnected inverter having time constant of $T_{I/C}$ and T_I respectively. Similarly, stochastic wind power from the turbine is passed through a wind generator system having gain K_{WTG} and time constant T_{WTG}. The stochastic model of solar and wind power is similar to the gBm model and the system parameters are adopted from [16]. Geometric Brownian motion is used for the solar irradiance $(\breve{\Phi}(t))$ and the Ornstein-Uhlenbeck (OU) Brownian motion model is utilized for the wind speed (v) and load demand. The solar power (P_{PV}) and wind power (P_W) is related to solar irradiance and wind speed as follows:

$$P_{PV} = \eta S\breve{\Phi}(t)\{1 - 0.005(\mathrm{T_a} + 25)\}, \tag{64}$$

where, the parameters $\eta = 10\%$ is the conversion efficiency of the PV cells, $S = 4084\ \mathrm{m}^2$ is the measured area of the PV array, Φ is measured in $\mathrm{kW/m}^2$ which is the solar radiation of the PV cells and $\mathrm{T_a} = 25^{\circ}C$ is considered as the ambient temperature:

$$P_W(t) = \begin{cases} 130 - 63v(t) + 9.1v^2(t) - 0.3v^3(t) & ;4 < v(t) < 15\ \mathrm{m/s} \\ 140 + 11v(t) - 0.36v^2(t) & ;15 \le v(t) < 26\ \mathrm{m/s} \\ 0 & ;v(t) > 26\ \mathrm{m/s}. \end{cases} \tag{65}$$

The wind speed is considered between 0 and 30 m/s for the single

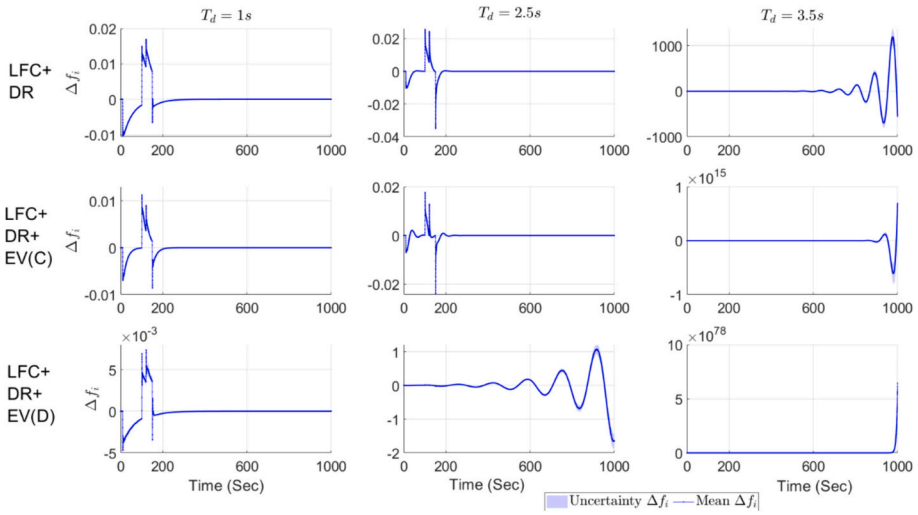

Fig. 20. Frequency fluctuations for different demand response system configurations with variation in the packet drop rates calculated for the over 100 Monte Carlo simulations.

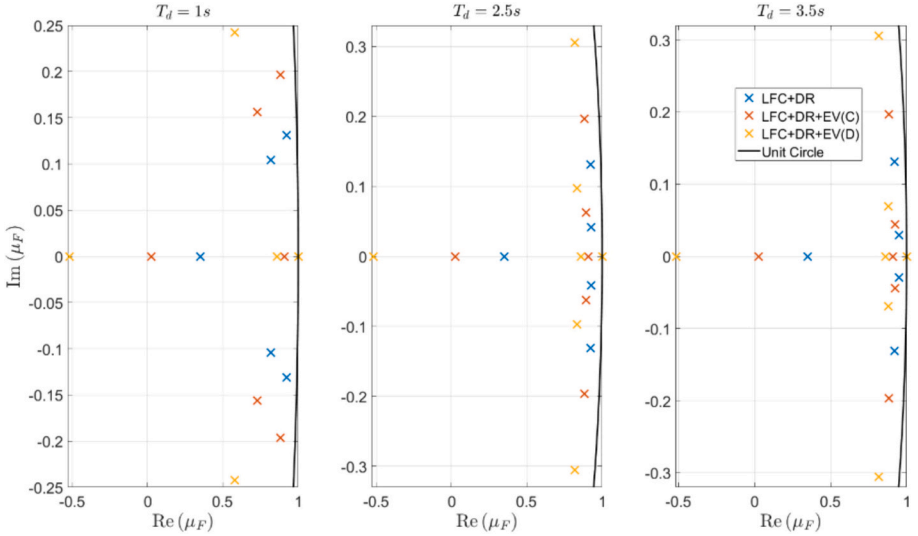

Fig. 21. Configuration of the poles of different discrete systems with an increase in time delays due to demand response.

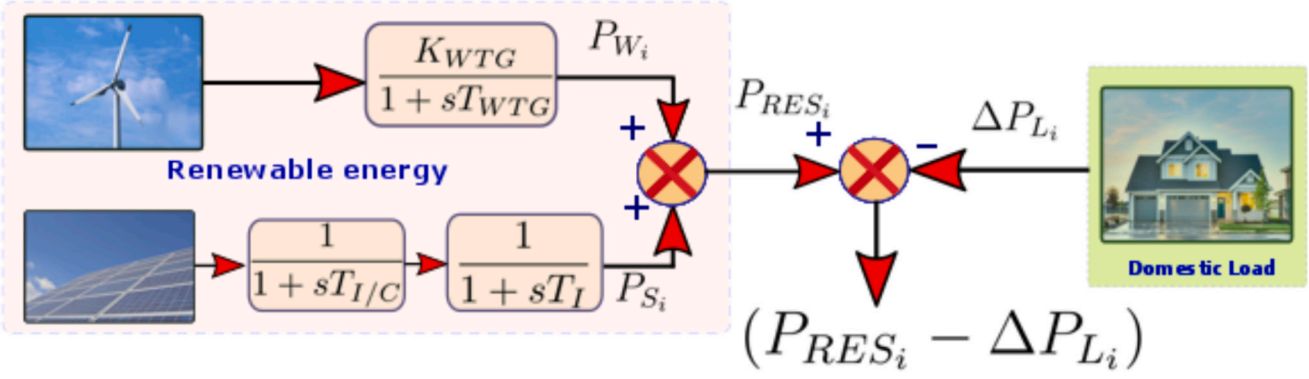

Fig. 22. Schematic of the stochastic renewable energy (solar and wind) and load demand used in the LFC configuration.

area. The rate and the drift for solar irradiation and parameters to simulate Ornstein-Uhlenbeck process for the load demand and wind velocity are obtained from [16] to generate the random input profiles for solar irradiation. The gBm has been simulated in MATLAB using the function `gbm()` in the Financial Toolbox. The mean and uncertainty of the Monte Carlo simulations of the stochastic solar power, wind power and load demand are shown in Fig. 23.

Let us introduce a variable $k_{P_{\mathrm{Ren}}}$ that is equal to the renewable energy

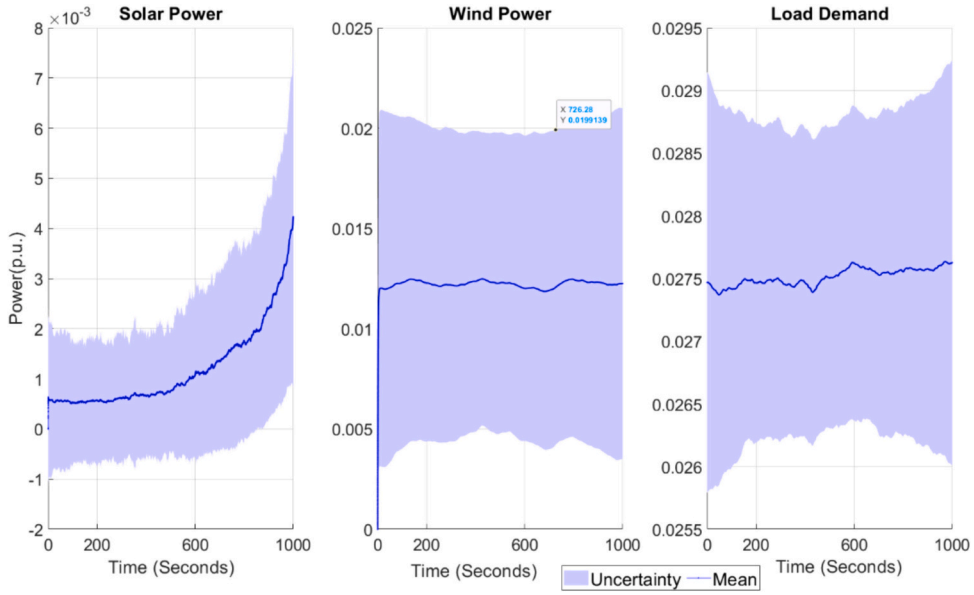

Fig. 23. Uncertainty and mean of the stochastic solar power, wind power and load demand after 500 Monte Carlo simulations.

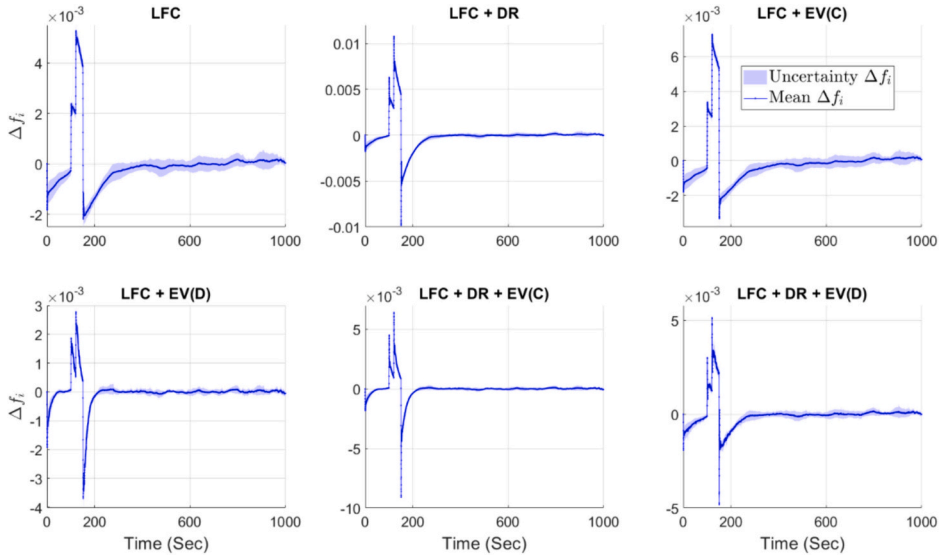

Fig. 24. Frequency fluctuations for LFC and different fluctuations for the stochastic load demand and renewable energy with 500 Monte Carlo simulations.

utilization factor shown in Fig. 25. Thus, considering its positive and negative oscillations, we consider the absolute value of the variable. Hence, we can write:

$$\frac{P_{\text{Ren}}}{P_{\text{Ren}}+\Delta P_{Th_i}} = |k_{P_{\text{Ren}}}| \Rightarrow \Delta P_{Th_i} = \left(\frac{1-|k_{P_{\text{Ren}}}|}{|k_{P_{\text{Ren}}}|}\right) P_{\text{Ren}} \Rightarrow \Delta P_{Th_i}$$
$$= \left(\frac{1}{|k_{P_{\text{Ren}}}|} - 1\right) P_{\text{Ren}}. \tag{66}$$

It suggests when $k_{P_{\text{Ren}}} < 0$ and $k_{P_{\text{Ren}}} > 1$ then $\Delta P_{Th_i} < 0$. However, when $0 < k_{P_{\text{Ren}}} < 1$, the $\Delta P_{Th_i} > 0$. Moreover, we also observe that a smaller value $|k_{P_{\text{Ren}}}|$ will increase the thermal power output ΔP_{Th_i}. We observe in Fig. 25 that the fluctuation of $|k_{P_{\text{Ren}}}|$ is highest when LFC is with the centralized EV configuration. It suggests, when renewable energy is used for LFC, the LFC with demand response and LFC with centralized EV configuration, they tend to reduce the thermal power output. The increase in thermal power output is observed only after $t > 600$, for LFC and LFC with demand response. However, for the LFC with decentralized EV configuration and LFC with demand response and centralized EV configuration $k_{P_{\text{Ren}}}$ lies between 0 and 1 mainly after $t > 200$. Moreover, initial fluctuation of $|k_{P_{\text{Ren}}}|$ is also lower as compared to the last three cases. It suggests that the LFC with decentralized EV configuration and LFC with demand response and centralized EV configuration utilizes thermal power plant output more than other configurations. However, for LFC with demand response and a decentralized EV configuration, the $|k_{P_{\text{Ren}}}| > 1$ maximum fluctuation is lower, as compared to the LFC with decentralized EV configuration and LFC with demand response and centralized EV configuration. The random fluctuations in Fig. 25 can be explained with the help of the power balance equation. Since the frequency fluctuation is close to zero, as shown in Fig. 24, we can suggest that the power generation and demand is almost balanced as:

$$\Delta P_{Th_i} + P_{\text{Ren}} + \Delta P_{DR} + \Delta P_{EV} \approx \Delta P_L$$
$$\Rightarrow \Delta P_{Th_i} \approx \Delta P_L - P_{\text{Ren}} - \Delta P_{DR} - \Delta P_{EV}. \tag{67}$$

Substituting the value of ΔP_{Th_i} from (66) in (67), we obtain:

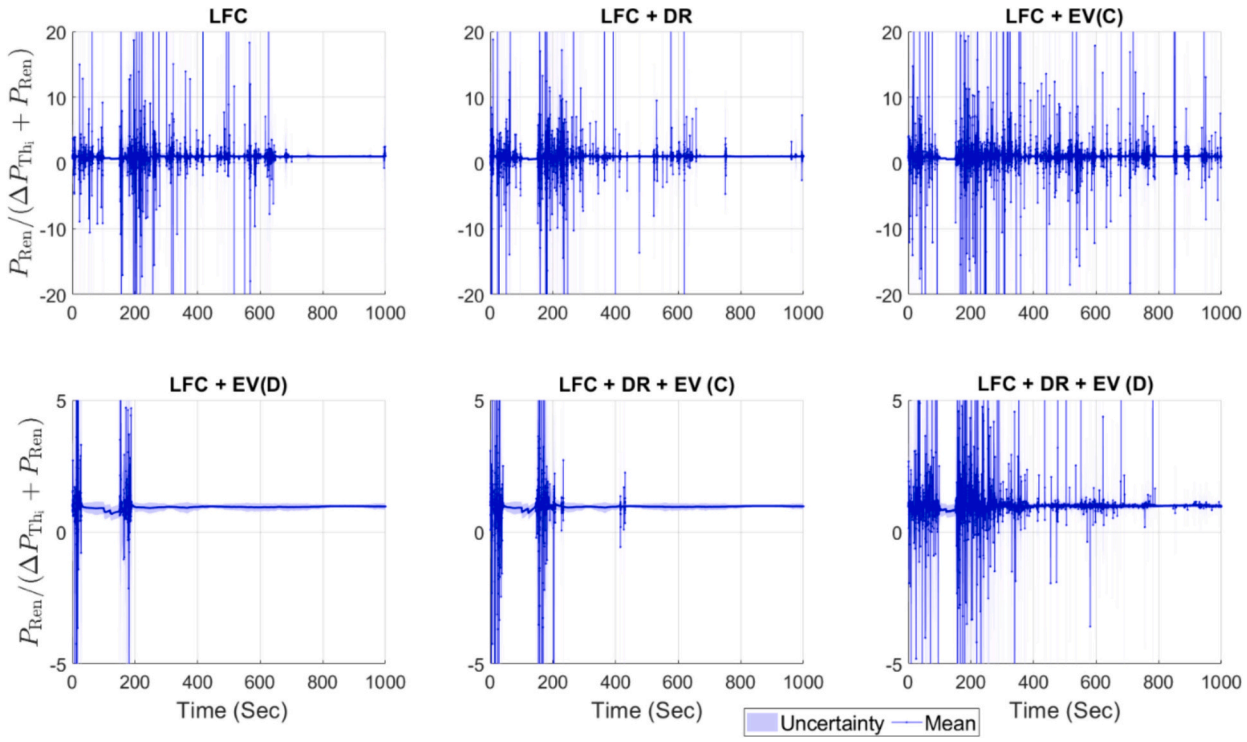

Fig. 25. Renewable energy utilization for different system configurations obtained after 500 Monte Carlo simulations of renewable energy source. The uncertainty is considered at one standard deviation.

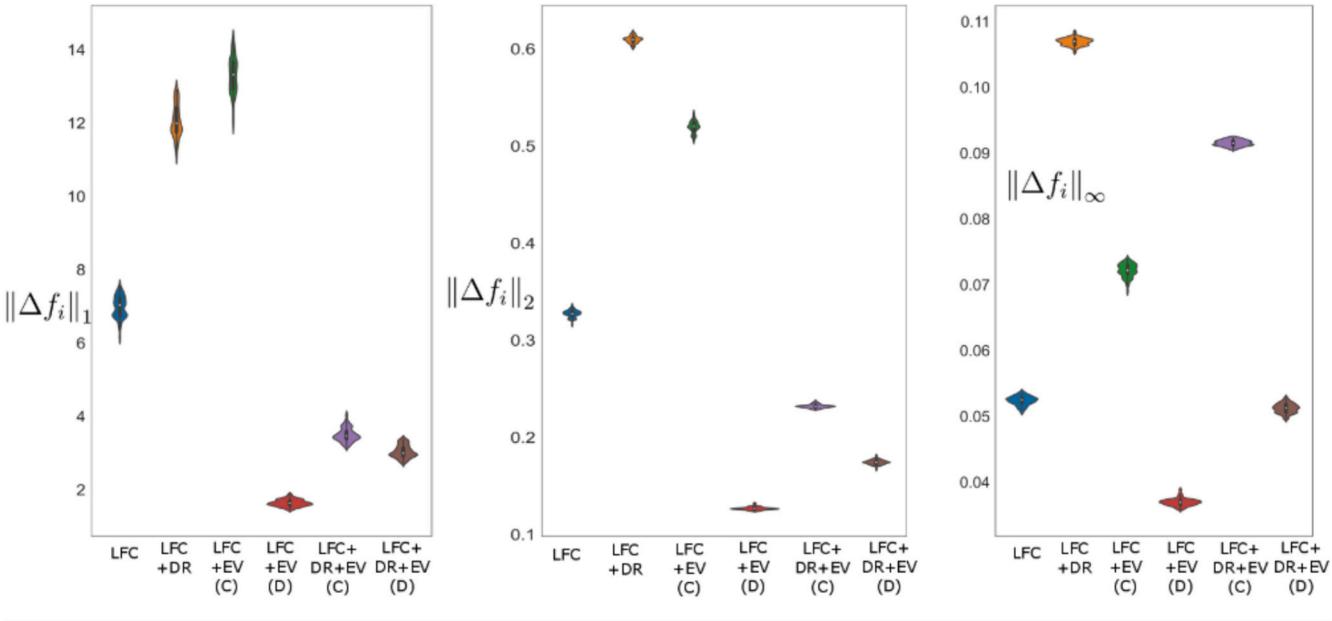

Fig. 26. Boxplot for the L_1 norm, L_2 norm and L_∞ norm of frequency fluctuations for different system configurations.

$$\left(\frac{1}{|k_{P_{\text{Ren}}}|} - 1\right) P_{\text{Ren}} \approx \Delta P_L - P_{\text{Ren}} - \Delta P_{DR} - \Delta P_{EV},$$
$$\Rightarrow \Delta P_L \approx \frac{1}{|k_{P_{\text{Ren}}}|} P_{\text{Ren}} + \Delta P_{DR} + \Delta P_{EV}. \tag{68}$$

We observe that when $0 < k_{P_{\text{Ren}}} < 1$, P_{Ren} is highly utilized to meet the load fluctuations. Thus, we can infer from (67) and (68) that if we increase the higher renewable energy fluctuation, utilization leads to higher thermal power output. A higher value of $|k_{P_{\text{Ren}}}|$ for the LFC system suggests that the load is mainly met by thermal power since there is no demand response and EV power, and it also explains the higher uncertainty in the frequency fluctuation in Fig. 24. When LFC is utilized with decentralized EV configuration and with demand response and centralized EV configuration, we observe $0 < k_{P_{\text{Ren}}} < 1$ which suggests that renewable energy is highly utilized for those configurations to meet the load fluctuations. However, when EV is utilized in a decentralized configuration, demand response and EV output are primarily utilized to meet the load fluctuation due to the higher value of $|k_{P_{\text{Ren}}}|$ in this system

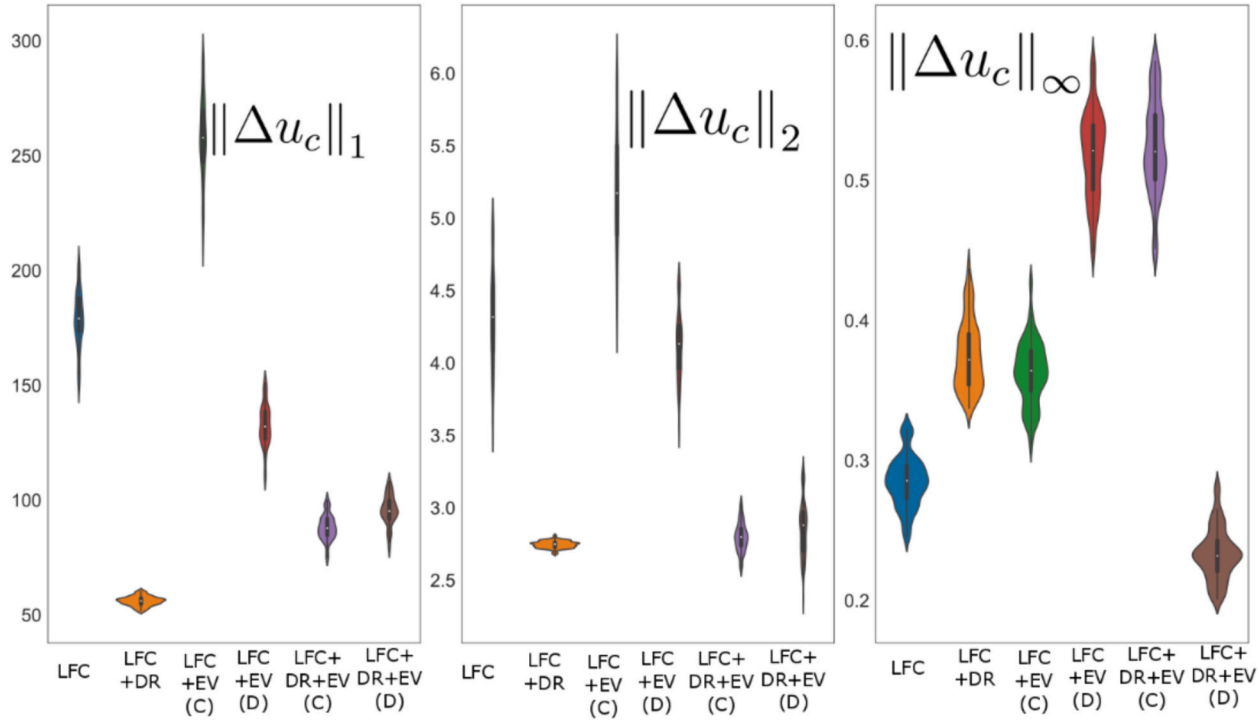

Fig. 27. Boxplot for the L_1-norm, L_2-norm and L_∞-norm of governor control input fluctuations for different system configurations.

Table 1
Multivariate normality test results on the frequency fluctuations and governor control signal norms.

Signals	$\widehat{\beta}_{1,m}$	$\widehat{\beta}_{2,m}$	Critical distance	*p*-value
$\|\Delta f_i\|_1, \|\Delta f_i\|_2, \|\Delta f_i\|_\infty$	6.795	12.585	7.814	0
$\|\Delta u_{c_i}\|_1, \|\Delta u_{c_i}\|_2, \|\Delta u_{c_i}\|_\infty$	1.787	11.524	7.814	0

Table 2
Results of nonparametric multivariate test for the frequency fluctuation and governor control signals norms considering different system configuration as the samples.

Signals	Test statistic (F)	Degrees of freedom (df_1)	Degrees of freedom (df_2)	*p*-value
$\|\Delta f_i\|_1, \|\Delta f_i\|_2, \|\Delta f_i\|_\infty$	7621.986	15	8260	0
$\|\Delta u_{c_i}\|_1, \|\Delta u_{c_i}\|_2, \|\Delta u_{c_i}\|_\infty$	3927.158	15	8260	0

configuration. In our simulation studies in many cases, the frequency fluctuation is quite small showing the efficacy of the LMI based robust control design since without the analytical stability framework such large disturbance could easily destabilize the LFC.

When renewable energy is introduced in the disturbance input, we see a frequency fluctuation within a specific limit while satisfying the requirement [92]. However, we observe that the uncertainty limit is low due to the magnitude of FDI attack being much higher than the renewable energy generation fluctuations. We also observe that due to demand response, the uncertainty in the frequency fluctuations Δf_i is relatively low. The maximum fluctuations in frequency are lowest when the decentralized configuration of EV is utilized with LFC.

The L_1 norm, L_2 norm and L_∞ norm of frequency fluctuations Δf_i are shown in Fig. 19, explaining that the total fluctuations are highest for LFC with DR and centralized EV configuration, while it is lowest for LFC with a decentralized EV combination. The LFC, DR, and EV with the centralized configuration, have lower frequency fluctuations than the two combinations. The maximum fluctuations of LFC, DR, and EV with centralized configuration are much higher than that in the decentralized configuration. However, the total absolute fluctuation $\|\Delta f_i\|_1$ for the two configurations is similar.

For a quantitative check of the Δf_i, we have to conduct a statistical hypothesis test. Firstly, we need to check whether the signal norms are multivariate normal. The multivariate statistical test on the signal norms is performed similarly in [100], where multivariate normality is tested. The test is conducted with the help of the function mult.*norm*() in the QuantPsyc package in R [101]. The skewness and kurtosis coefficients $\widehat{\beta}_{1,m}$ and $\widehat{\beta}_{2,m}$ are used to compute the test statistic and the *p*-value for checking the normality. The details about the coefficients are provided in [100]. As we observe in the univariate plot in Fig. 26 and Fig. 27, the data does not follow a normal distribution. The qualitative inference is confirmed by the *p*-value in Table 1, which is 0. The critical distance is the same for both the signals as it only depends on the sample size, which is considered to be equal. However, the skewness coefficient for the governor control signal norms is smaller than the frequency fluctuation norms Δf_i. Since the *p*-value is zero, a nonparametric multivariate test is to be conducted on the given data.

Then we perform a nonparametric multivariate test using the nonpartest() function using the *npmv* package in R [102] on the given data considering the three norms as the factor levels while testing 1000 Monte Carlo samples and different LFC system configurations. Wilk's lambda statistic is considered here, which has an effective test statistic that follows an F-distribution having degrees of freedom df_1 and df_2. The expressions for the effective test statistic and degrees of freedom is mentioned in [100]. We observe in Table 2, that the *p*-value is zero, which confirms that neither the frequency nor the control norms are similar for the different system configurations. The degrees of freedom are the same for both the signal norms as they only depend on the sample size. However, the test statistic for the governor control signal norms is lower than the frequency deviations, which states that the governor control signal norms are similar for the different system configuration as compared to the frequency fluctuation norms.

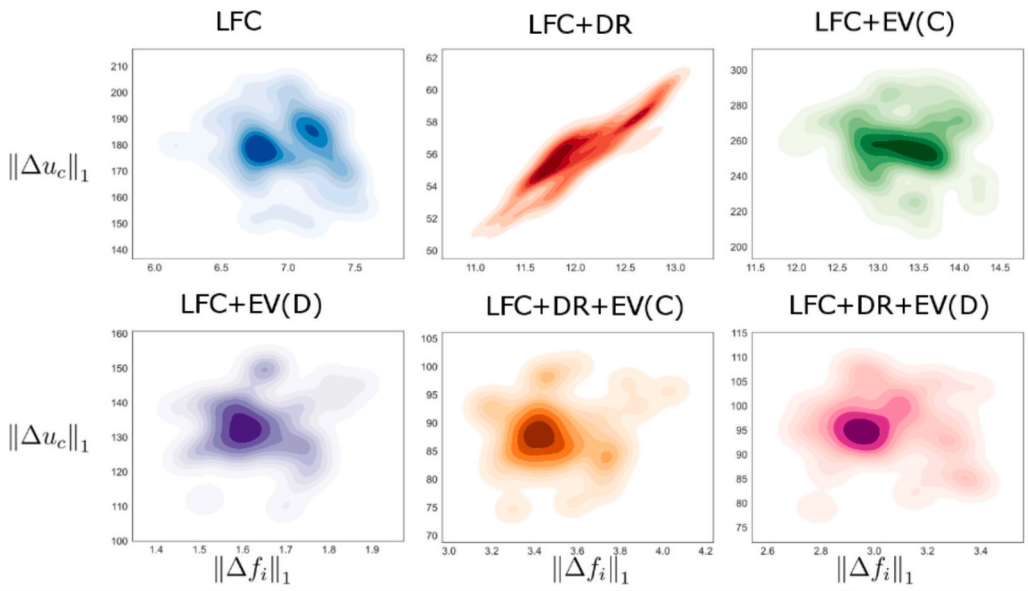

Fig. 28. Bivariate analysis of the L_1-norm of the frequency fluctuations and governor control input with 500 Monte Carlo simulations.

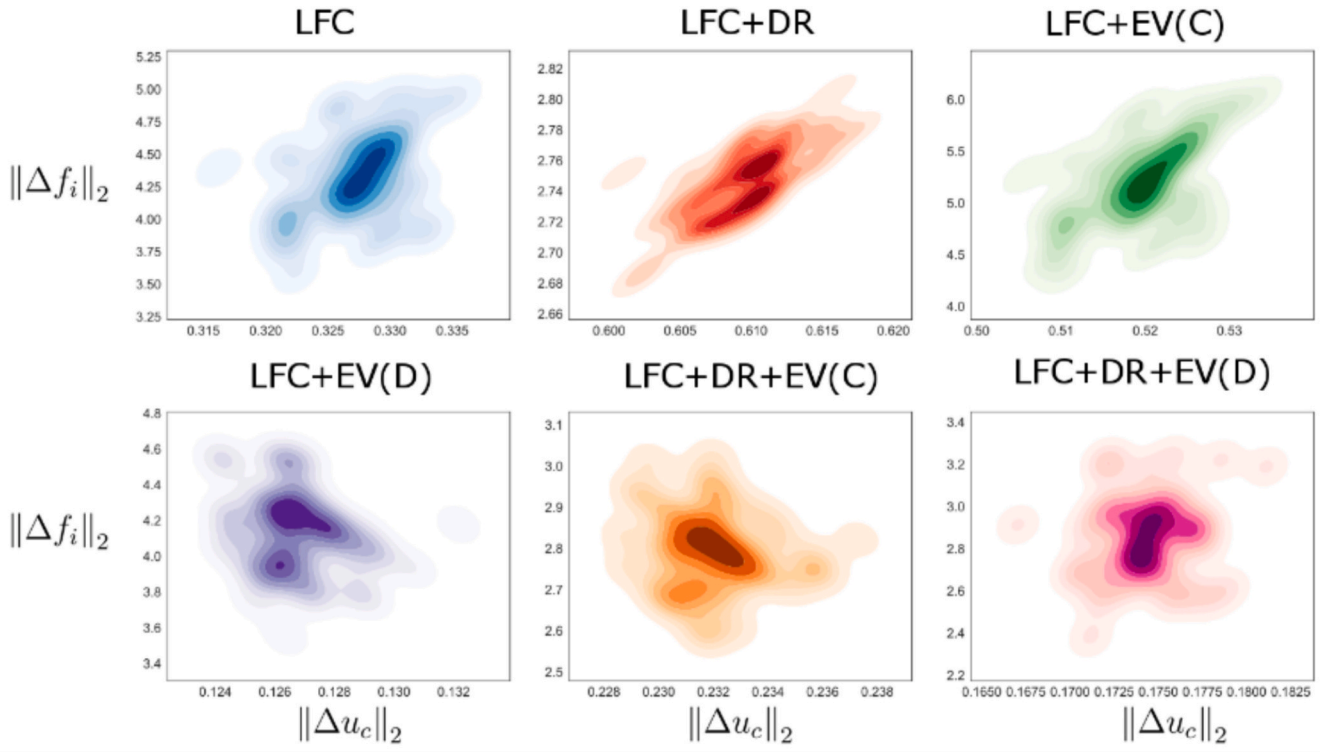

Fig. 29. Bivariate analysis of the L_2-norm of the frequency fluctuations and governor control input with 500 Monte Carlo simulations.

Similarly, the comparison is also performed on the governor control input, based on the three norms as shown in Fig. 27. Here, $\|\Delta u_c\|_2$ represents the cost of the spinning reserves as given in [54]. We observe that with the combination of LFC, DR, and EV, the cost due to spinning reserves is reduced. Even with DR, only the cost is relatively low as well. However, the spinning reserve cost is highest when EV with centralized configuration is used along with LFC with high uncertainty per ensemble of disturbance vector. When we observe the overall fluctuations, we see a positive correlation pattern for the relationship between the and $\|\Delta f_i\|_1$ for the LFC and DR configuration in Fig. 28. A bimodal bivariate distribution is observed only in the case of LFC configuration. However, for the other configurations, no significant correlation pattern can be deduced.

In Fig. 29 we observe that the spinning reserve cost is positively correlated to the frequency fluctuations in LFC, DR and EV combinations. A slight positive correlation is obtained for simple LFC cases. However, a slight negative correlation is obtained for the $\|\Delta f_i\|_2$ and $\|\Delta u_c\|_2$, with no correlation obtained when LFC, DR and EV are used in a decentralized fashion. Thus, we can say that by incorporating the DR and EV in a centralized configuration, the rate of frequency fluctuations increases with a relative increase in the governor control input. As far as the maximum fluctuation is concerned, we observe a positive correlation

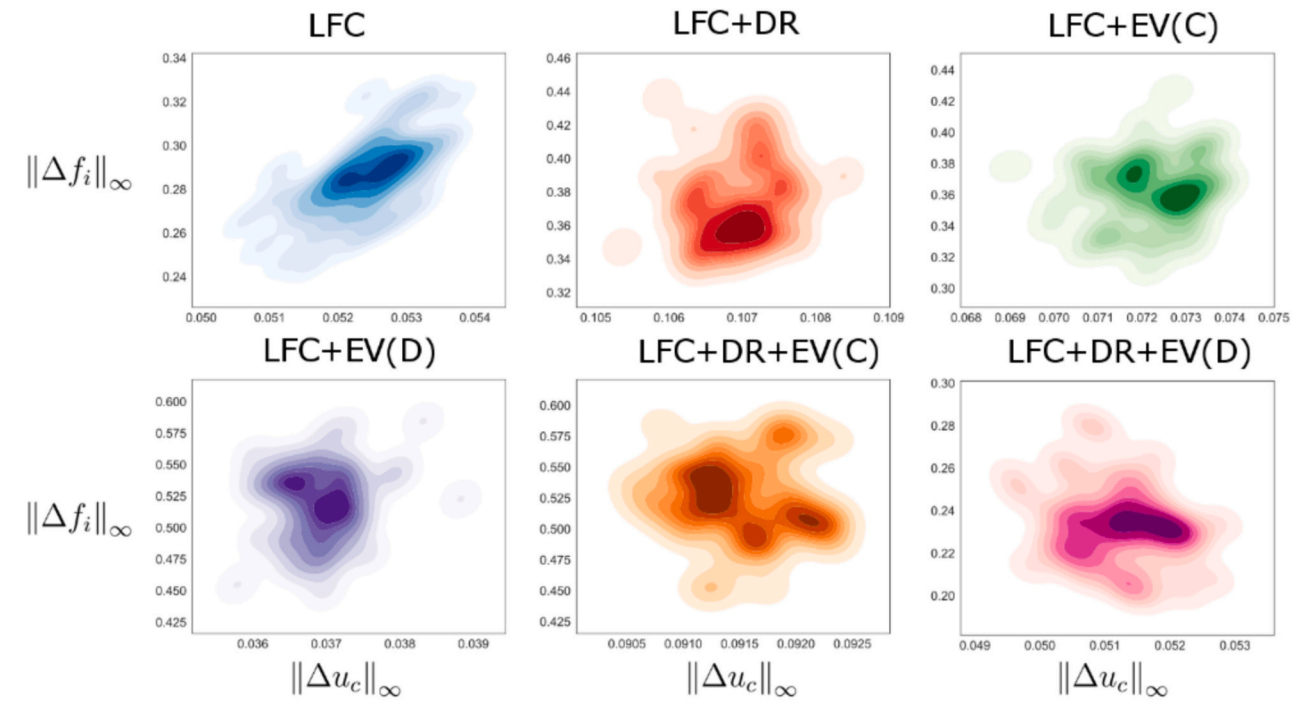

Fig. 30. Bivariate analysis of the L_∞-norm of the frequency fluctuations and governor control input with 500 Monte Carlo simulations.

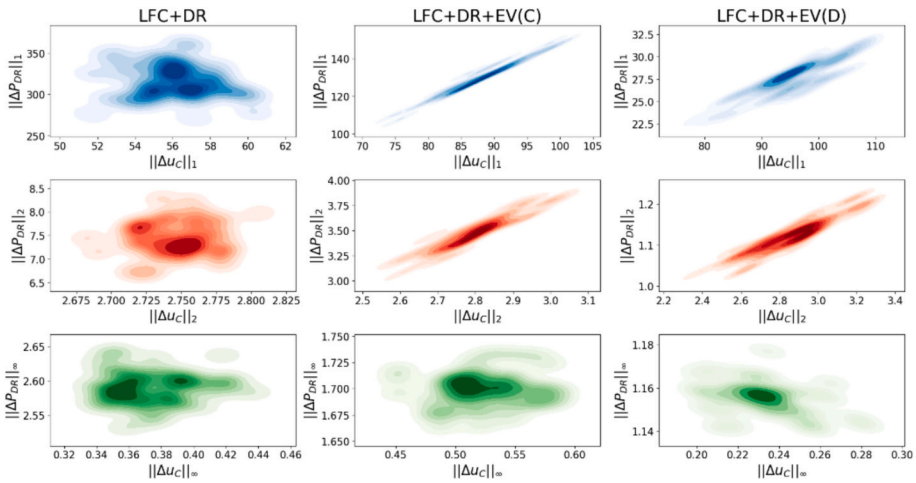

Fig. 31. Bivariate analysis of the norms of the demand response and governor control input with 500 Monte Carlo simulations.

between frequency and control input in Fig. 30. The bimodal pattern is observed for the LFC and centralized and decentralized EV configuration. A trimodal pattern is observed for LFC, DR and centralized EV configuration.

We do not see any significant correlation between the governor control input and the DR output signal norms for LFC and DR configuration in Fig. 31. However, trimodal distribution in the case of L_1 and L_∞ norms of the variables is observed. We observe a positive correlation when EV is added to the LFC and DR configuration, which states that increased control input is equally matched by increased DR output. The power output from the EV effectively nullifies the above power output as observed for the L_1 and L_2 norm fluctuations in Fig. 31. However, we do not see any such pattern of the demand response output ΔP_{DR} with the frequency fluctuation Δf_i in Fig. 32. A slight positive correlation is observed in the case of ΔP_{DR} and Δf_i for LFC and DR combination. The distribution is also mostly unimodal except in the L_∞-norm of LFC, DR and centralized EV combination. We observe a positive correlation in the L_1-norm and L_2-norm of the ΔP_{EV} and the governor control input Δu_c when using the LFC, DR and EV configuration in Fig. 33. Some positive correlation is also observed in the L_∞-norm relation for LFC, DR and decentralized EV configuration. A bimodal distribution is observed for the L_2-norm and L_∞-norm of the variables concerned. Moreover, an obtuse tilt of the 2D kernel density estimate (KDE) plot indicates a slight negative correlation between the L_2-norm of ΔP_{EV} and Δu_c.

A positive correlation is observed for the L_∞-norm between electric vehicle output ΔP_{EV} and frequency fluctuations Δf_i in the LFC case with decentralized EV configuration as observed in Fig. 34. Similarly, a positive correlation with multimodal distribution is observed in LFC with DR and centralized EV configuration. However, a slight negative correlation and multiple modes are observed in the case of LFC, DR and decentralized EV configuration. In the bivariate plots of L_1 and L_2 norms, we do not observe a strong correlation pattern. However, we observe a significant bimodal data pattern in the case of L_2-norm between ΔP_{EV} and Δf_i.

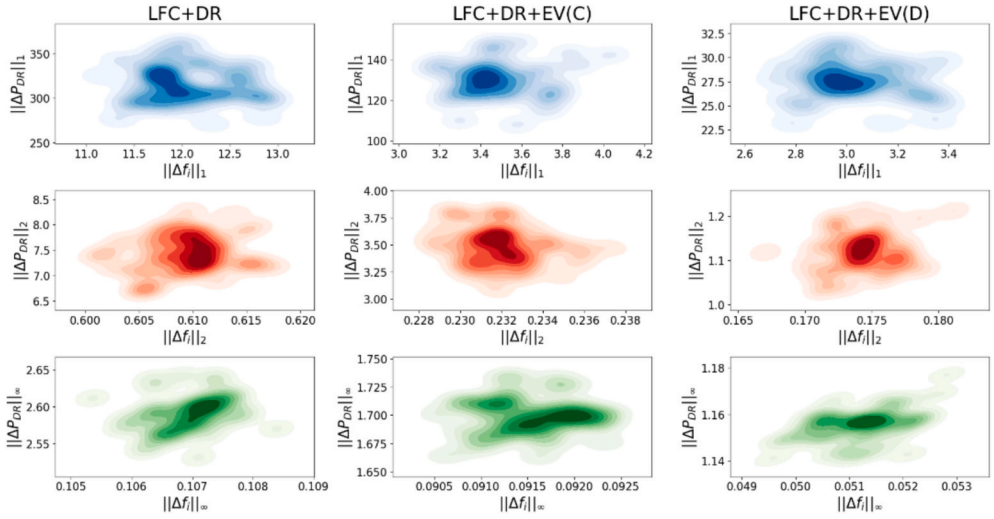

Fig. 32. Bivariate analysis of the norms of the frequency fluctuations and demand response output with 500 Monte Carlo simulations.

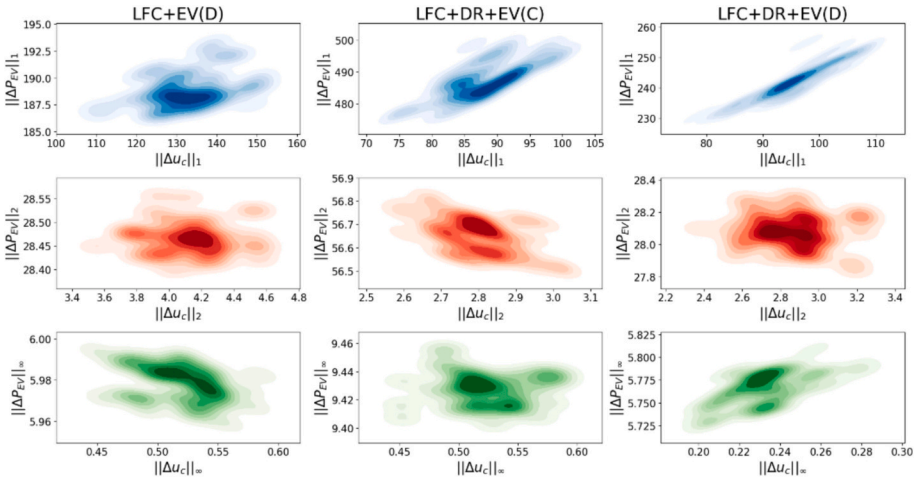

Fig. 33. Bivariate analysis of the norms of the governor control input and electric vehicle output with 500 Monte Carlo simulations.

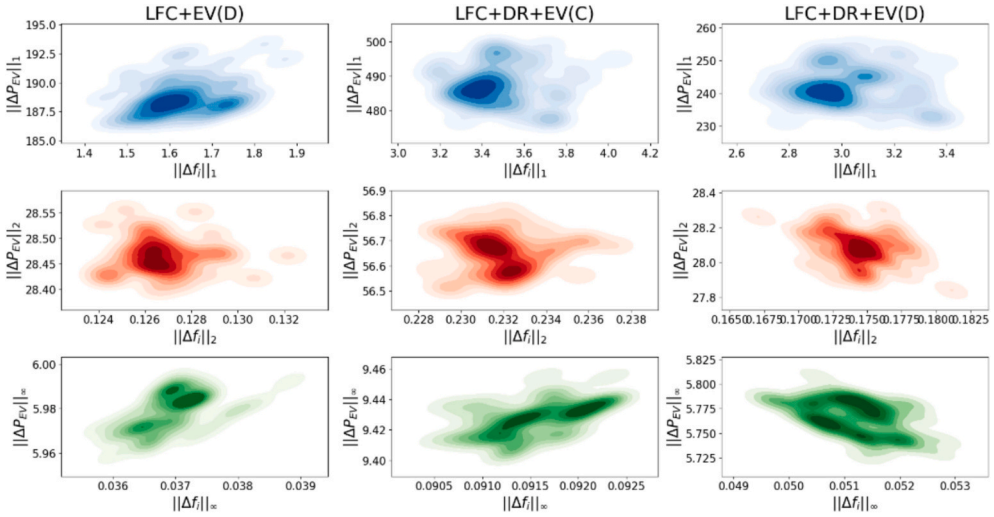

Fig. 34. Bivariate analysis of the norms of the frequency fluctuations and electric vehicle output with 500 Monte Carlo simulations.

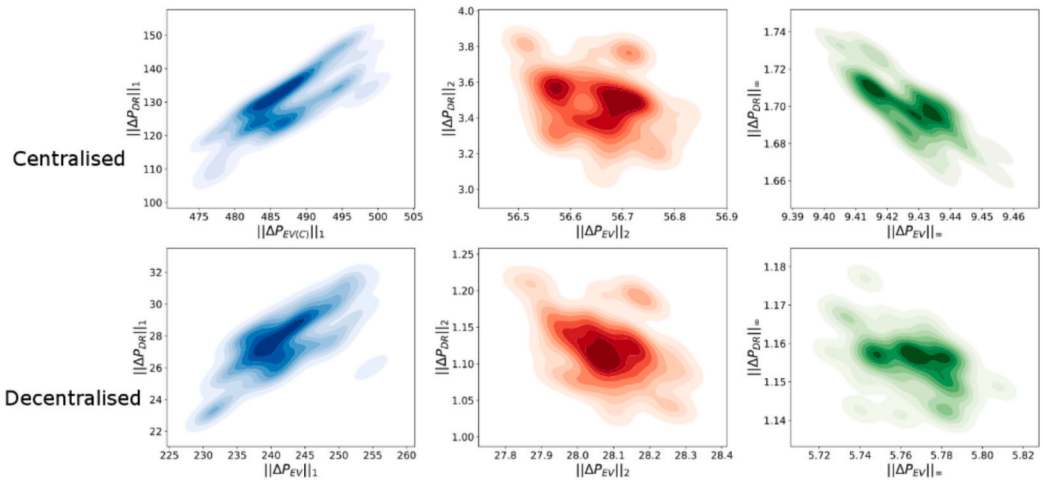

Fig. 35. Bivariate analysis of the EV power output norms and demand response power for centralized and decentralized EV configurations obtained from 500 Monte Carlo simulations.

A positive correlation is observed between the DR output and EV output L_1-norm signal, as shown in Fig. 35. However, in the L_∞ norm, the correlation is slightly more negative for centralized strategy with demand response output than decentralized output. It suggests that the maximum fluctuations of DR output will decrease with maximum fluctuations in EV output when operating as a centralized configuration. However, the pattern remains similar for both the cases suggesting that the rate of change in EV output is similar for both the configuration, with the requirement more in centralized strategy than the decentralized one.

Hence, we can summarize the outcomes from the detailed simulation results as follows:

- The state feedback controller and observer gain, derived from solving the LMIs, ensure stable operation under bounded load disturbance and FDI attack. This stability extends to higher packet drop rates of up to 90 %, as depicted in Fig. 4, and up to 85 % packet drop rate, as shown in Fig. 19. The frequency fluctuations remain within the prescribed limit of the IEEE standard for grid operations [86].
- Incorporating decentralized EVs into the LFC loop results in stable operation at higher sampling times, while utilizing lower communication bandwidth, as illustrated in Fig. 4 when compared to different LFC configurations with DR and EVs.
- Nonetheless, the system configured with decentralized EVs is vulnerable to parametric variations, such as delays in demand response or increase in packet drop rates, which can lead to increased frequency fluctuations and instability, as evidenced by the instability arising from increased packet drop rates in Fig. 19 at a 99 % packet drop rate.
- Integration of LFC with EVs and demand response strategies can yield lower spinning reserve costs, as compared to standalone LFC or LFC coupled with either EVs or DR alone, as demonstrated in Fig. 27, through comparison of the L_2-norm of the control input.

6. Conclusions

In this paper, a joint state feedback controller and an observer has been designed for the decentralized LFC system with demand response and EV. The stability conditions are derived using a switched system using an ADS model, where the controller and observer gains were obtained using a CCL algorithm solving an LMI for different LFC, DR and EV configurations. The system response is checked at different packet drop rates and time delay due to demand response. The frequency fluctuations, governor control input, EV and DR output are analysed using bivariate plots. The analysis is computed with the respective L_1, L_2 and L_∞ signal norms obtained when renewable energy is considered as disturbance vector. The analysis is also aided by the nonparametric statistical tests for frequency fluctuations and governor control input signal norms.

The main findings of the paper are summarized as follows:

- The state feedback controller and observer gain obtained after solving the LMI can ensure stable operation under bounded load disturbance and FDI attack and at a higher packet drop rate of 90 %.
- The combination of decentralized EV in the LFC loop leads to stable operation at higher sampling time, utilizing lower communication bandwidth.
- However, the system with decentralized EV configuration is susceptible to parametric variations like the demand response time delay or increase in packet drop rate as it can cause higher frequency fluctuations and instability.
- Combining LFC with EV and demand response strategies can lead to lower spinning reserve cost than standalone LFC or LFC with either EV or demand response.

Although the controller design steps may seem quite complex using the LMI framework to find the stabilizing controller for the NCS, cast as a discrete time switched system, after the control design for practical implementation, it's simply an observer-based state feedback controller. It has been shown in the past that such LMI based NCS design can handle very high percentage of packet dropout if the sampling time is sufficiently small as compared to the system time constants which is reinforced here through the study of wide variety of complex system architectures, even with 99 % packet dropout rate.

Future work will incorporate designing less restrictive LMIs so that concept can be extended to a larger number of areas by incorporating deregulation factors while also investigating scalability of the LMI based networked control algorithm on larger state space models of multi-area LFC systems. Moreover, accuracy of the whole complex power system model can also be verified using real operational data using suitable statistical inference methods in future research.

CRediT authorship contribution statement

Deepak Kumar Panda: Writing – original draft, Visualization, Software, Methodology, Investigation, Formal analysis, Data curation. **Kaushik Halder:** Writing – review & editing, Validation, Conceptualization. **Saptarshi Das:** Writing – review & editing, Supervision, Resources, Project administration, Funding acquisition, Conceptualization.

Stuart Townley: Writing – review & editing, Validation, Supervision.

Declaration of competing interest

The authors declare that they have no known competing financial interests or personal relationships that could have appeared to influence the work reported in this paper.

Data availability

Data will be made available on request.

Acknowledgement

For the purpose of open access, the author has applied a Creative Commons Attribution (CC BY) license to any author accepted manuscript version arising.

Appendix A

Typical parameters for the LFC model are given as:

$T_d = 1, H = 5, D = 1, M = 10, T_t = 0.3, T_g = 0.1, R = 0.05, T_E = 1, K_E = 1, \beta = 1 + (1/R)$,
$r = 1, \alpha_1 = 1.5, \alpha_2 = 1.25, \alpha_3 = 1.25, \alpha_4 = 1.1, T_s = 0.09$ (LFC), $T_s = 0.06$ (LFC + DR), $T_s = 0.06$ (LFC + EV_C),
$T_s = 0.14$ (LFC + EV_D), $T_s = 0.09$ (LFC + DR + EV_C), $T_s = 0.14$ (LFC + DR + EV_D).

References

[1] Doherty R, O'malley M. A new approach to quantify reserve demand in systems with significant installed wind capacity. IEEE Trans Power Syst 2005;20(2):587–95.
[2] Tabatabaee S, Mortazavi SS, Niknam T. Stochastic scheduling of local distribution systems considering high penetration of plug-in electric vehicles and renewable energy sources. Energy 2017;121:480–90.
[3] Aalami H, Moghaddam MP, Yousefi G. Demand response modeling considering interruptible/curtailable loads and capacity market programs. Appl Energy 2010;87(1):243–50.
[4] Broeer T, Tuffner FK, Franca A, Djilali N. A demand response system for wind power integration: greenhouse gas mitigation and reduction of generator cycling. CSEE Journal of Power and Energy Systems 2018;4(2):121–9.
[5] Safiullah H, Hug G, Tongia R. Design of load balancing mechanism for Indian electricity markets. Energy Systems 2017;8:309–50.
[6] "Non-BM balancing services and volumes reports." [Online]. Available: https://www.nationalgrideso.com/document/107511/download.
[7] Chan S-C, Tsui KM, Wu H, Hou Y, Wu Y-C, Wu FF. Load/price forecasting and managing demand response for smart grids: methodologies and challenges. IEEE Signal Process Mag 2012;29(5):68–85.
[8] Schäfer B, Matthiae M, Timme M, Witthaut D. Decentral smart grid control. New J Phys 2015;17(1):015002.
[9] Singh VP, Kishor N, Samuel P. Improved load frequency control of power system using LMI based PID approach. J Frankl Inst 2017;354(15):6805–30.
[10] Prakash A, Murali S, Shankar R, Bhushan R. HVDC tie-link modeling for restructured AGC using a novel fractional order cascade controller. Electr Power Syst Res 2019;170:244–58.
[11] Kumar BS, Mishra S. AGC for distributed generation. In: 2008 IEEE International Conference on Sustainable Energy Technologies; 2008. p. 89–94.
[12] Chang-Chien L-R, Lin W-T, Yin Y-C. Enhancing frequency response control by DFIGs in the high wind penetrated power systems. IEEE Trans Power Syst 2010;26(2):710–8.
[13] Gautam D, Goel L, Ayyanar R, Vittal V, Harbour T. Control strategy to mitigate the impact of reduced inertia due to doubly fed induction generators on large power systems. IEEE Trans Power Syst 2010;26(1):214–24.
[14] Zhao H, Wu Q, Hu S, Xu H, Rasmussen CN. Review of energy storage system for wind power integration support. Appl Energy 2015;137:545–53.
[15] Hossain M, Saha T, Mithulananthan N, Pota H. Robust control strategy for PV system integration in distribution systems. Appl Energy 2012;99:355–62.
[16] Panda DK, Das S, Townley S. Toward a more renewable energy-based LFC under random packet transmissions and delays with stochastic generation and demand. IEEE Trans Autom Sci Eng 2020;19(2):1217–32.
[17] Pan I, Das S. Kriging based surrogate modeling for fractional order control of microgrids. IEEE Transactions on Smart grid 2014;6(1):36–44.
[18] Molina-Garcia A, Bouffard F, Kirschen DS. Decentralized demand-side contribution to primary frequency control. IEEE Trans Power Syst 2010;26(1):411–9.
[19] Pourmousavi SA, Nehrir MH. Introducing dynamic demand response in the LFC model. IEEE Trans Power Syst 2014;29(4):1562–72.
[20] Moghadam MRV, Ma RT, Zhang R. Distributed frequency control in smart grids via randomized demand response. IEEE Transactions on Smart Grid 2014;5(6):2798–809.
[21] Babahajiani P, Shafiee Q, Bevrani H. Intelligent demand response contribution in frequency control of multi-area power systems. IEEE Transactions on Smart Grid 2016;9(2):1282–91.
[22] Benysek G, Bojarski J, Jarnut M, Smolenski R. Decentralized active demand response (DADR) system for improvement of frequency stability in distribution network. Electr Power Syst Res 2016;134:80–7.
[23] Benysek G, Bojarski J, Smolenski R, Jarnut M, Werminski S. Application of stochastic decentralized active demand response (DADR) system for load frequency control. IEEE Transactions on Smart Grid 2016;9(2):1055–62.
[24] Hosseini SA, Toulabi M, Dobakhshari AS, Ashouri-Zadeh A, Ranjbar AM. Delay compensation of demand response and adaptive disturbance rejection applied to power system frequency control. IEEE Trans Power Syst 2019;35(3):2037–46.
[25] Masuta T, Yokoyama A. Supplementary load frequency control by use of a number of both electric vehicles and heat pump water heaters. IEEE Transactions on Smart Grid 2012;3(3):1253–62.
[26] Khooban M-H. Secondary load frequency control of time-delay stand-alone microgrids with electric vehicles. IEEE Trans Ind Electron 2017;65(9):7416–22.
[27] Senjyu T, Tokudome M, Yona A, Sekine H, Funabashi T, Kim C-H. A frequency control approach by decentralized generators and loads in power systems. In: *2008 IEEE 2nd International Power and Energy Conference*; 2008. p. 79–84.
[28] Kumar LS, Kumar GN, Madichetty S. Pattern search algorithm based automatic online parameter estimation for AGC with effects of wind power. Int J Electr Power Energy Syst 2017;84:135–42.
[29] Yao E, Wong VW, Schober R. Robust frequency regulation capacity scheduling algorithm for electric vehicles. IEEE Transactions on Smart Grid 2016;8(2):984–97.
[30] Debbarma S, Dutta A. Utilizing electric vehicles for LFC in restructured power systems using fractional order controller. IEEE Transactions on Smart Grid 2016;8(6):2554–64.
[31] Bindra A. Securing the power grid: protecting smart grids and connected power systems from cyberattacks. IEEE Power Electronics Magazine 2017;4(3):20–7.
[32] Rao GS, et al. Performance comparison of various energy storage devices in combined LFC and AVR of multi area system with renewable energy integration. International Journal of Renewable Energy Research (IJRER) 2020;10(2):933–44.
[33] Revathi D, Mohan Kumar G. Analysis of LFC in PV-thermal-thermal interconnected power system using fuzzy gain scheduling. International Transactions on Electrical Energy Systems 2020;30(5):e12336.
[34] Jampeethong P, Khomfoi S. Coordinated control of electric vehicles and renewable energy sources for frequency regulation in microgrids. IEEE Access 2020;8:141967–76.
[35] Yang T, Zhang Y, Li W, Zomaya AY. Decentralized networked load frequency control in interconnected power systems based on stochastic jump system theory. IEEE Transactions on Smart Grid 2020;11(5):4427–39.
[36] Hua C, Wang Y. Delay-dependent stability for load frequency control system via linear operator inequality. IEEE Transactions on Cybernetics 2020;52(7):6984–92.
[37] Saxena S, Fridman E. Event-triggered load frequency control via switching approach. IEEE Trans Power Syst 2020;35(6):4484–94.
[38] Wen S, Yu X, Zeng Z, Wang J. Event-triggering load frequency control for multiarea power systems with communication delays. IEEE Trans Ind Electron 2015;63(2):1308–17.
[39] Yuan H, Xia Y, Yang H, Yuan Y. Resilient control for wireless networked control systems under DoS attack via a hierarchical game. International Journal of Robust and Nonlinear Control 2018;28(15):4604–23.
[40] Ameli A, Hooshyar A, El-Saadany EF, Youssef AM. Attack detection and identification for automatic generation control systems. IEEE Trans Power Syst 2018;33(5):4760–74.
[41] Sargolzaei A, Yen KK, Abdelghani MN, Sargolzaei S, Carbunar B. Resilient design of networked control systems under time delay switch attacks, application in smart grid. IEEE Access 2017;5:15901–12.

[42] Sargolzaei A, Yazdani K, Abbaspour A, Crane III CD, Dixon WE. Detection and mitigation of false data injection attacks in networked control systems. IEEE Trans Industr Inform 2019;16(6):4281–92.
[43] Abbaspour A, Sargolzaei A, Forouzannezhad P, Yen KK, Sarwat AI. Resilient control design for load frequency control system under false data injection attacks. IEEE Trans Ind Electron 2019;67(9):7951–62.
[44] Li Y, Huang R, Ma L. False data injection attack and defense method on load frequency control. IEEE Internet Things J 2020;8(4):2910–9.
[45] Guha D. Non-integer disturbance observer-aided resilient frequency controller applied to hybrid power system. Chaos, Solitons Fractals 2023;170:113421.
[46] Zhang W-A, Yu L. Output feedback stabilization of networked control systems with packet dropouts. IEEE Trans Autom Control 2007;52(9):1705–10.
[47] Wang Z, Yang F, Ho DW, Liu X. Robust H_∞ control for networked systems with random packet losses. IEEE Transactions on Systems, Man, and Cybernetics, Part B (Cybernetics) 2007;37(4):916–24.
[48] Zhang H, Shi Y, Mehr AS. Robust static output feedback control and remote PID design for networked motor systems. IEEE Trans Ind Electron 2011;58(12):5396–405.
[49] Liu C-Z, Li L, Yong J-W, Muhammad F, Cheng S, Wu Q. An innovative adaptive cruise control method with packet dropout. IEEE Trans Intell Transp Syst 2020;22(11):7102–14.
[50] Shi Y, Huang J, Yu B. Robust tracking control of networked control systems: application to a networked DC motor. IEEE Trans Ind Electron 2012;60(12):5864–74.
[51] Zhang J, Peng C, Xie X, Yue D. Output feedback stabilization of networked control systems under a stochastic scheduling protocol. IEEE Transactions on Cybernetics 2019;50(6):2851–60.
[52] Pang Z-H, Liu G-P, Zhou D, Chen M. Output tracking control for networked systems: a model-based prediction approach. IEEE Trans Ind Electron 2013;61(9):4867–77.
[53] Xiong S, Chen M, Wu Q. Predictive control for networked switch flight system with packet dropout. Appl Math Comput 2019;354:444–59.
[54] Singh AK, Singh R, Pal BC. Stability analysis of networked control in smart grids. IEEE Transactions on Smart Grid 2014;6(1):381–90.
[55] Zhang W, Branicky MS, Phillips SM. Stability of networked control systems. IEEE Control Syst Mag 2001;21(1):84–99.
[56] Halder K, Das S, Dasgupta S, Banerjee S, Gupta A. Controller design for networked control systems—an approach based on L2 induced norm. Nonlinear Analysis: Hybrid Systems 2016;19:134–45.
[57] Halder K, Panda DK, Das S, Das S, Gupta A. Specified QoS based networked observer and PI controller design with disturbance and noise rejection under random packet dropout. Physica A: Statistical Mechanics and its Applications 2022;604:127965.
[58] Shi Y, Yu B. Output feedback stabilization of networked control systems with random delays modeled by Markov chains. IEEE Trans Autom Control 2009;54(7):1668–74.
[59] Halder K, Das S, Panda DK, Das S, Gupta A. QoS aware joint observer and networked PI/PID controller design using LMIs under specified rate of packet dropouts. Appl Math Comput 2021;401:126125.
[60] IEEE. IEEE standard for phasor data concentrators for power systems. 2019.
[61] Liao K, Xu Y. A robust load frequency control scheme for power systems based on second-order sliding mode and extended disturbance observer. IEEE Trans Industr Inform 2017;14(7):3076–86.
[62] Hu Z, Liu S, Luo W, Wu L. Resilient distributed fuzzy load frequency regulation for power systems under cross-layer random denial-of-service attacks. IEEE Transactions on Cybernetics 2020;52(4):2396–406.
[63] 1815-2012 - IEEE Standard for Electric Power Systems Communications-Distributed Network Protocol (DNP3). 2012.
[64] Alhelou HH, Golshan MEH, Hatziargyriou ND. Deterministic dynamic state estimation-based optimal LFC for interconnected power systems using unknown input observer. IEEE Transactions on Smart Grid 2019;11(2):1582–92.
[65] Trefke J, Rohjans S, Uslar M, Lehnhoff S, Nordström L, Saleem A. Smart grid architecture model use case management in a large European Smart Grid project. IEEE PES ISGT Europe 2013;2013:1–5.
[66] Santodomingo R, Uslar M, Göring A, Gottschalk M, Nordström L, Saleem A, et al. SGAM-based methodology to analyse Smart Grid solutions in DISCERN European research project. In: 2014 IEEE International Energy Conference (ENERGYCON); 2014. p. 751–8.
[67] Pan I, Das S. Design of hybrid regrouping PSO-GA based sub-optimal networked control system with random packet losses. Memetic Computing 2013;5:141–53.
[68] Dasgupta S, Halder K, Banerjee S, Gupta A. Stability of Networked Control System (NCS) with discrete time-driven PID controllers. Control Eng Pract 2015;42:41–9.
[69] Shangguan X-C, He Y, Zhang C-K, Yao W, Zhao Y, Jiang L, et al. Resilient load frequency control of power systems to compensate random time delays and time-delay attacks. IEEE Trans Ind Electron 2022;70(5):5115–28.
[70] Machowski J, Lubosny Z, Bialek JW, Bumby JR. Power system dynamics: stability and control. John Wiley & Sons; 2020.
[71] Gao X-Y. Two-layer-liquid and lattice considerations through a (3+ 1)-dimensional generalized Yu-Toda-Sasa-Fukuyama system. Appl Math Lett 2024;152:109018.
[72] Gao X-Y. Considering the wave processes in oceanography, acoustics and hydrodynamics by means of an extended coupled (2+ 1)-dimensional Burgers system. Chin J Phys 2023;86:572–7.
[73] 2030.6-2016 - IEEE Guide for the Benefit Evaluation of Electric Power Grid Customer Demand Response. 2016.
[74] Van Loan CF, Golub GH. Matrix computationsvol. 3. Baltimore: Johns Hopkins University Press; 1983.
[75] Ogata K. Discrete-time control systems. Prentice-Hall, Inc.; 1995.
[76] Lin H, Antsaklis PJ. Stability and persistent disturbance attenuation properties for a class of networked control systems: switched system approach. Int J Control 2005;78(18):1447–58.
[77] Hassibi A, Boyd SP, How JP. Control of asynchronous dynamical systems with rate constraints on events. In: Proceedings of the 38th IEEE Conference on Decision and Control (Cat. No. 99CH36304). vol. 2; 1999. p. 1345–51.
[78] Liberzon D, Morse AS. Basic problems in stability and design of switched systems. IEEE Control Syst Mag 1999;19(5):59–70.
[79] DeCarlo RA, Branicky MS, Pettersson S, Lennartson B. Perspectives and results on the stability and stabilizability of hybrid systems. Proc IEEE 2000;88(7):1069–82.
[80] Yu M, Wang L, Chu T, Xie G. Stabilization of networked control systems with data packet dropout and network delays via switching system approach. In: 2004 43rd IEEE Conference on Decision and Control (CDC)(IEEE Cat. No. 04CH37601). 4; 2004. p. 3539–44.
[81] Alessandri A, Baglietto M, Battistelli G. Luenberger observers for switching discrete-time linear systems. Int J Control 2007;80(12):1931–43.
[82] Alessandri A, Coletta P. Switching observers for continuous-time and discrete-time linear systems. In: Proceedings of the 2001 American Control Conference. (Cat. No. 01CH37148). 3; 2001. p. 2516–21.
[83] Yang F, Wang Z, Hung YS, Gani M. H_∞ control for networked systems with random communication delays. IEEE Trans Autom Control 2006;51(3):511–8.
[84] Farhadi M, Mohammed OA. Performance enhancement of actively controlled hybrid DC microgrid incorporating pulsed load. IEEE Trans Ind Appl 2015;51(5):3570–8.
[85] Zhu J, Wu H, Huang J, Hua M, Li L, Xing Y. A dual-dc output three-phase three-level ac-dc converter for low-frequency pulsed power decoupling applications. IEEE Trans Ind Electron 2021;69(1):52–63.
[86] Fu M, Luo Z-Q. Computational complexity of a problem arising in fixed order output feedback design. Syst Control Lett 1997;30(5):209–15.
[87] El Ghaoui L, Oustry F, AitRami M. A cone complementarity linearization algorithm for static output-feedback and related problems. IEEE Trans Autom Control 1997;42(8):1171–6.
[88] Gao H, Chen T, Lam J. A new delay system approach to network-based control. Automatica 2008;44(1):39–52.
[89] Lofberg J. YALMIP: a toolbox for modeling and optimization in MATLAB. In: 2004 IEEE International Conference on Robotics and Automation (IEEE Cat. No. 04CH37508); 2004. p. 284–9.
[90] Sturm JF. Using SeDuMi 1.02, a MATLAB toolbox for optimization over symmetric cones. Optimization Methods and Software 1999;11(1–4):625–53.
[91] Li H, Chow M-Y, Sun Z. Optimal stabilizing gain selection for networked control systems with time delays and packet losses. IEEE Trans Control Syst Technol 2009;17(5):1154–62.
[92] IEEE standard for interconnection and interoperability of distributed energy resources with associated electric power systems interfaces. 2018.
[93] Das S, Halder K, Gupta A. Delay handling method in dominant pole placement based PID controller design. IEEE Trans Industr Inform 2019;16(2):980–91.
[94] Halder K, Das S, Gupta A. Time delay handling in dominant pole placement with PID controllers to obtain stability regions using random sampling. Int J Control 2021;94(12):3384–405.
[95] Liberzon D. Switching in systems and controlvol. 190. Springer; 2003.
[96] Lin H, Antsaklis PJ. Stability and stabilizability of switched linear systems: a survey of recent results. IEEE Trans Autom Control 2009;54(2):308–22.
[97] Hespanha JP, Morse AS. Stability of switched systems with average dwell-time. In: Proceedings of the 38th IEEE Conference on Decision and Control (Cat. No. 99CH36304). vol. 3; 1999. p. 2655–60.
[98] Hespanha JP. Uniform stability of switched linear systems: extensions of LaSalle's invariance principle. IEEE Trans Autom Control 2004;49(4):470–82.
[99] Zhai G, Hu B, Yasuda K, Michel AN. Stability analysis of switched systems with stable and unstable subsystems: an average dwell time approach. Int J Syst Sci 2001;32(8):1055–61.
[100] Panda DK, Das S. Economic operational analytics for energy storage placement at different grid locations and contingency scenarios with stochastic wind profiles. Renew Sust Energ Rev 2021;137:110474.
[101] T. D. Fletcher and M. T. D. Fletcher, "Package 'QuantPsyc,'" R Package URL: https://cran.r-project org/web/packages/QuantPsyc/QuantPsyc.pdf, 2010.
[102] Burchett WW, Ellis AR, Harrar SW, Bathke AC. Nonparametric inference for multivariate data: the R package npmv. J Stat Softw 2017;76:1–18.